

COHERENT NEAR INFRARED PHOTODETECTION WITH INDIUM GALLIUM  
ARSENIDE BASED OPTOELECTRONIC DEVICES

A DISSERTATION

SUBMITTED TO THE DEPARTMENT OF MECHANICAL ENGINEERING

AND THE COMMITTEE ON GRADUATE STUDIES

OF STANFORD UNIVERSITY

IN PARTIAL FULFILLMENT OF THE REQUIREMENTS FOR THE DEGREE OF

DOCTOR OF PHILOSOPHY

Jun-Xian Fu

September 2005

© Copyright by Jun-Xian Fu 2005  
All Rights Reserved

I certify that I have read this dissertation and that in my opinion it is fully adequate, in scope and quality, as dissertation for the degree of Doctor of Philosophy.

---

Prof. James S. Harris, Jr. Principal Advisor

I certify that I have read this dissertation and that in my opinion it is fully adequate, in scope and quality, as dissertation for the degree of Doctor of Philosophy.

---

Prof. Martin M. Fejer

I certify that I have read this dissertation and that in my opinion it is fully adequate, in scope and quality, as dissertation for the degree of Doctor of Philosophy.

---

Prof. David A. B. Miller

Approved for the University Committee on Graduate Studies

---

## ABSTRACT

Over the extremely broad electromagnetic spectrum, the near-infrared region (0.7-3 $\mu\text{m}$ ) is of great interests to physicists, chemists and biologists. Coherent photo-detection in the near-infrared as well as visible and other wavelength regions is extremely useful in identifying coherent light sources from the noisy background. It has great potential to be applied to single-molecule detection by surface-enhanced coherent anti-Stokes Raman scattering. Other applications include chemical gas detection, remote sensing and environmental monitoring, semiconductor processing control and others.

Indium gallium arsenide (InGaAs) based optoelectronic devices have been extensively investigated in the wavelength range extending from 800nm for gallium-rich material to 3 $\mu\text{m}$  for indium-rich material. A range of InGaAs alloys with bandgap energies in the near infrared wavelength range are investigated by solid-source molecular beam epitaxy (SSMBE). They include strain-free standard  $\text{In}_{0.532}\text{Ga}_{0.468}\text{As}$  and  $\text{In}_{0.532}\text{Ga}_{0.468}\text{AsN}_x\text{Sb}_y$  lattice-matched to InP substrates, highly strained pseudomorphic  $\text{In}_x\text{Ga}_{1-x}\text{As}/\text{In}_y\text{Ga}_{1-y}\text{As}$  quantum structures on InP substrates and relaxed metamorphic thick  $\text{In}_{x>0.8}\text{Ga}_{1-x}\text{As}$  device layers with cyclic arsenic-assisted in-situ annealed step-graded InAlAs buffer layers on GaAs and InP substrates. An InP/InAlAs/InGaAs heterojunction bipolar phototransistor (HPT) is designed, simulated and fabricated. The electrical and optical properties, such as responsivity and spectral response, of the HPT are characterized.

A compact standing-wave Fourier-transform interferometer system capable of coherent detection in the near-infrared region is demonstrated. A new technique of identifying coherent light sources using harmonic Fourier spectra analysis is developed. The system only includes a PZT-controlled gold-coated scan mirror and a partial-transparent (3.8% single-path loss) InP/InAlAs/InGaAs HPT. The close-loop scan range of PZT-controlled mirror is 32 $\mu\text{m}$ . With such mirror scan length, at the harmonic 5<sup>th</sup> order spectrum components, the resolution of the demonstrated interferometer is 37.5 $\text{cm}^{-1}$  with the free spectral range  $\sim 340\text{nm}$  and central spectral position at 1500nm. The system resolution could reach 1 $\text{cm}^{-1}$  with improved system design and elements selection.

## ACKNOWLEDGMENTS

I would like to thank Prof. James Harris, “coach”, for his continuing supports on both the academic research and the personal life in the five years of graduate student life in the farm. I feel so fortunate to have a very free research environment he provided. Even during the frustrated days of painful system maintenance, endless fabrication processes in the clean-room, and unsuccessful optical measurements, I know he is always there for help. His broad knowledge and optimistic attitudes inspired me to find the beauty in the art of MBE and the fun in the fields of optoelectronics.

I would like to thank Prof. Martin Fejer and Prof. David A. B. Miller for serving on my PhD dissertation oral defense and reading committees. I am grateful to their insightful feedbacks and advices on the final form of my dissertation. I would like to thank Prof. Mark Brongersma and Prof. Mark Schnitzer for serving on my PhD dissertation oral defense committee. I would like to thank Dr. Glen Solomon for helpful discussions on all subjects. I feel so fortunate to have opportunities taking classes instructed by great professors from several departments in Stanford University, Applied Physics, Electrical Engineering, Material Science and Engineering.

Part of my dissertation and research work was under the PWASSP project, which was funded by DARPA starting from 2001 till 2004, on developing Si-MEMS based standing-wave Fourier-transform interferometer, collaborating with Dr. Helen Kung, Dr. Sameer Bhalotra and Dr. Ofer Levi. I enjoyed the team-working experience with them.

Many students in Harris’ group contributed to this dissertation. Dr. Chien-chung Lin acted as a mentor training me on MBE and showed me what way to take in order to enjoy the fun and pain. Dr. Vijit Sabnis, Dr. Wonill Ha, Dr. Vince Lordi, Dr. Lynford Goddard and Kai Ma provided many helps from the very beginning on various parts of my research work in the MBE lab, clean-room and optics lab.

Xiaojun Yu, my “Jun-brother” and working partner on the MBE system-I, is one of the best friends I found in Stanford. We worked closely on the MBE materials growth and machine maintenance. He helped me on the TEM characterization of material

structural property. I believe the five-year working relationship will lead to a life-long friendship.

Many students either helped me on my dissertation or worked me on various projects in Stanford. My thanks go to Luigi Scaccabarozzi, Alireza Khalili, Yu-Hsuan Kuo, Zhilong Rao, Yangsi Ge, and all the other students in Harris' group; Ray Chen, Shen Ren from Miller's group and Carsten Langrock, Xiuping Xie from Fejer's group.

My parents and sister are always the strongest support all through my life. Without their unselfish supports in the past twenty-nine years, I would not be able to be finishing this dissertation. Qi, my wife, has been accompanying me through all my happiness and sadness for more than five years. Without her understanding and agitation, I will not achieve so much so far. My heartfelt appreciations and thanks are given to my whole family.

## TABLE OF CONTENTS

List of tables.....	ix
List of figures.....	x
Chapter 1 Background .....	1
1.1 Infrared and IR system.....	1
1.1.1 IR detectors .....	2
1.1.2 Coherence and coherent detection .....	4
1.1.3 Spectrometer .....	5
1.2 Semiconductor and molecular beam epitaxy .....	8
1.2.1 Instruments, general principles, and techniques .....	10
1.2.2 Heteroepitaxy and lattice engineering .....	13
1.3 Indium gallium arsenide .....	15
1.4 Summary .....	18
References:.....	18
Chapter 2 InGaAs-based material systems: growth and characterization .....	22
2.1 Lattice-matched material systems on InP substrates .....	22
2.1.1 InGaAs and InAlAs.....	22
2.1.2 InGaAs(NSb) .....	29
2.2 Pseudomorphic growth of highly-strained ingaas.....	39
2.2.1 Strain-balanced $\text{In}_x\text{Ga}_{1-x}\text{As}/\text{In}_y\text{Ga}_{1-y}\text{As}$ superlattice .....	40
2.2.2 Fractional monolayer superlattice $\text{In}_{0.53}\text{Ga}_{0.47}\text{As}/\text{InAs}$ .....	44
2.2.3 Conclusion .....	47
2.3 Metamorphic growth of relaxed InGaAs .....	47
2.3.1 TD reduction and defect control .....	48
2.3.2 Sample growth and in-situ monitoring .....	49
2.3.3 Surface morphology and evolution.....	52
2.3.4 Strain relaxation and characterization.....	54
2.3.5 Optical characterization .....	61
2.3.6 Conclusion .....	62
2.4 Summary .....	63

References:.....	63
Chapter 3 Device design, fabrication and characterization .....	68
3.1 Detector and linearity.....	68
3.1.1 PIN photodiode.....	69
3.1.2 Phototransistor .....	70
3.2 Device design and fabrication.....	75
3.2.1 AlGaAs/GaAs PIN photodiode.....	76
3.2.2 InP/InGaAs/InAlAs DHPT .....	78
3.3 Device characterization.....	82
3.4 Summary .....	87
References:.....	87
Chapter 4 Standing-wave fourier-transform interferometer .....	89
4.1 Fourier transform and harmonic spectra components.....	89
4.2 Standing wave ftir design.....	95
4.2.1 Optical model.....	95
4.2.2 Detector absorption region thickness.....	97
4.2.3 Tolerance analysis.....	98
4.2.4 Fabry-Perot effect .....	99
4.3 SWFTIR setup .....	101
4.4 Optical measurements.....	103
4.4.1 Single frequency light source.....	103
4.4.2 Multiple wavelength light sources.....	105
4.5 Summary .....	108
References:.....	109
Chapter 5 Summary .....	110
Appendix A.....	112
Appendix B .....	113

## LIST OF TABLES

<i>Number</i>	<i>Page</i>
Table 1-1: IR detector type and material systems.....	3
Table 2-1: Growth conditions for three test samples with same N cell condition.....	30
Table 4-1: Comparision between traditional FTIR and H-SWFTIR .....	107

## LIST OF FIGURES

<i>Number</i>	<i>Page</i>
Figure 1-1: Coherence and monochromatic.....	5
Figure 1-2: Michelson spectrometer.....	6
Figure 1-3: Standing-wave transform interferometer.....	7
Figure 1-4: Spectrometer arrays with standing-wave transform interferometer structure for hyper-spectral sensing and imaging applications.....	8
Figure 1-5: Three-chamber MBE system.....	10
Figure 1-6: Growth chamber of the MBE system.....	11
Figure 1-7: Homoepitaxy and heteroepitaxy.....	14
Figure 1-8: Defects in heteroepitaxy.....	15
Figure 1-9: Diagram of bandgap energy versus lattice constant.....	16
Figure 1-10: Congruent sublimation temperatures for ternary III-V materials.....	17
Figure 2-1: RHEED patterns during the InP deoxidization process and InGaAs epi- layer growth.....	24
Figure 2-2: XRD rocking curve of InGaAs layers grown on InP substrates ((100), $\omega/2\theta$ (004) scan) with different compositions from highly mismatch to lattice-match conditions.....	26
Figure 2-3 DGS structure as a transition layer between InGaAs and InAlAs layers.....	27
Figure 2-4: XRD rocking curve of DGS sample (top curve) and simulation (bottom)....	27
Figure 2-5: Room-temperature photoluminescence of DGS sample.....	28
Figure 2-6: Room-temperature optical absorption (transmission) measurement of the DGS sample.....	28
Figure 2-7: SQW samples grown by MBE.....	31
Figure 2-8: High-resolution XRD rocking curve of sample 1 with the thickness of SQW 50nm, measurement and simulation curves matched well.....	32
Figure 2-9: SIMS depth profiling analysis of sample 1, inset figure showing the nitrogen and antimony content in the QW region.....	33

Figure 2-10: XRD rocking curve of samples 2 & 3 for three different QW compositions, InGaAsSb (a), InGaAsN (b) and InGaAsNSb (c), simulation of (c) gave two different material compositions. ....	34
Figure 2-11: SIMS analysis showed N% increased in the case of antimony atoms present during the QW growth.....	35
Figure 2-12: RTPL of sample 2 (SQW with GaInNAs of N%=1.6%) and sample 3 (SQW with GaInNAsSb of N%=2.1% and Sb%=3.0%). ....	38
Figure 2-13: LTPL measurements for SQW structures of samples 2 and 3 and both of the samples were annealed at 720°C for one minute, where the features around 1.9μm come from the water absorption in the air.....	39
Figure 2-14: InGaAs film critical thickness on InP substrate.....	40
Figure 2-15: Strain-balanced growth. ....	41
Figure 2-16: Cross-section TEM (XTEM) picture of strain-balanced superlattice $\text{In}_x\text{Ga}_{1-x}\text{As}/\text{In}_y\text{Ga}_{1-y}\text{As}$ ( $x=0.41$ and $y=0.67$ ) grown on lattice-matched InGaAs/InP. ....	42
Figure 2-17: XRD rocking curve of $\text{In}_x\text{Ga}_{1-x}\text{As}/\text{In}_y\text{Ga}_{1-y}\text{As}$ superlattices: measurement curve with narrow satellite peak features (top) and simulation curve (bottom).....	42
Figure 2-18: RTPL of $\text{In}_x\text{Ga}_{1-x}\text{As}/\text{In}_y\text{Ga}_{1-y}\text{As}$ ( $x=0.41$ and $y=0.67$ ) superlattice. ....	43
Figure 2-19: Room-temperature optical absorption of the superlattice with absorption edge at around 1.95μm ( $\text{In}_{0.67}\text{Ga}_{0.33}\text{As}$ ), 1.7μm ( $\text{In}_{0.53}\text{Ga}_{0.47}\text{As}$ ), and features between 1.8-1.9μm due to the minibands absorption of the superlattice.....	43
Figure 2-20: XTEM of FMS SQW with LM-InGaAs cladding layers.....	44
Figure 2-21: XRD rocking curve of FMS-SQW with effective indium content 88%. ....	45
Figure 2-22: XRD rocking curve of 3 FMS-MQWs, measurement curve (blue) and effective 3-MQWs simulation curve (red) match well. ....	45
Figure 2-23: RTPL of FMS-SQW $\text{In}_{0.53}\text{Ga}_{0.47}\text{As}/\text{InAs}$ 1:3 with QW layer 6.8nm.....	46
Figure 2-24: TD motion corresponding to the thickness of strained layers.....	49

Figure 2-25: Substrate temperature change over the time evolution during the growth of LM-InAlAs buffer, metamorphic InAlAs graded-buffers and thick InGaAs device layers. ....	50
Figure 2-26: Sample structure with InGaAs device layer and the metamorphic linearly step-graded buffer layers.....	51
Figure 2-27: AFM for InGaAs grown on InP substrates with metamorphic InAlAs buffer at different substrate temperature: $T_{(a)} > T_{(b)} > T_{(c), (d)}$ . ....	53
Figure 2-28: AFM for InGaAs samples grown on GaAs substrates, left miscut (001) substrate with 4° toward [110]A, right (001) substrate. ....	53
Figure 2-29: XRD rocking curve ( $\omega$ - $2\theta$ ) of sample grown on GaAs substrate. ....	55
Figure 2-30: SIMS depth profiling of the same sample as above grown on GaAs substrate. ....	55
Figure 2-31: RSM diagram for (004) symmetric and (224) asymmetric scans. ....	57
Figure 2-32: RSM of InGaAs(device layer)/InAlAs metamorphic buffers grown on InP substrates for both (004) and (224) scans.....	58
Figure 2-33: RSM of InGaAs (device layer)/InAlAs metamorphic buffers grown on GaAs substrates for both (004) and (224) scans. ....	59
Figure 2-34: XTEM of InGaAs device layer grown on InP substrate with five-step graded InAlAs buffer layers (the first step was missing during the mechanical sample preparing process.....	61
Figure 2-35: RTPL of samples grown on InP and GaAs substrates. ....	62
Figure 2-36: Optical absorption of InGaAs device layers grown on GaAs substrates with step-graded metamorphic buffer layers. ....	62
Figure 3-1: Current components in Npn heterojunction bipolar (photo)transistor. ....	71
Figure 3-2: Scaling law of Npn HPT on the optical gain and small signal current gain, as well as the photocurrent density in the device.....	74
Figure 3-3: Absorption coefficient ( $\alpha$ ) and refractive index ( $n$ ) of intrinsic GaAs. ....	76
Figure 3-4: AlGaAs/GaAs p-i-n photodiode layer structure, mesa definition, substrate removal and flip-chip bonding for the integration purpose. ....	77
Figure 3-5: Absorption coefficient and refractive index of intrinsic LM-InGaAs. ....	78

Figure 3-6: DHPT with (a) abrupt B-C junction, and (b) graded B-C junction, with energy barrier at B-C junction removed by DSL.....	79
Figure 3-7: Epi-layers of collector-up Npn InP/InGaAs/InAlAs DHPT, mesa structure and Ohmic contact. ....	80
Figure 3-8: I-V characteristics of SHPT and DHPT.....	83
Figure 3-9: I-V characteristics of DHPT with large C-E voltage bias.....	84
Figure 3-10: I-V characteristics of a defective DHPT.....	85
Figure 3-11: Spectral responsivity characterization of a DHPT with emitter-up structure.....	86
Figure 3-12: Collector current characteristics with different incident laser powers.....	86
Figure 4-1: Fourier transform of periodical signals (top), sampling sinusoidal and distorted signals with a square window (bottom). ....	91
Figure 4-2: Distinguish two waves with different frequencies by sampling with fixed window width: (from top to bottom) single sinusoidal wave with normalized frequency 1, two sinusoidal waves with frequencies 1 and 1.02, two sinusoidal waves with frequencies 1 and 1.025, two sinusoidal waves with frequencies 1 and 1.1. Sampling window has a fixed width of $\Delta L = 25$ , $0.6/\Delta L = 0.024$ .....	92
Figure 4-3: Harmonic components in Fourier spectrum up to 5 <sup>th</sup> order. ....	93
Figure 4-4: Waveform and Fourier spectra of two ideal sinusoidal waves with different frequencies normalized 1 and 1.005 with sampling window width of $\Delta L = 25$ , (from top to bottom) the phase difference $\varphi = 0, 3\pi/4, 13\pi/16$ , and $7\pi/8$ . Frequency difference $0.005 \ll 0.6/\Delta L = 0.024$ . The improvement of the resolution of the system is at the cost of signal magnitude, and the peak difference in the bottom spectrum equals to $1/\Delta L + \Delta k$ with all the peak FWHM width of $1/\Delta L$ . ....	94
Figure 4-5: Scheme of a standing-wave transform spectrometer, the intensity of the standing-wave light field being sampled by a thin partially transparent detector.....	95
Figure 4-6: The dependence of sensitivity and contrast on the absorption layer thickness for a linear photodetector, shown in the left diagram is the	

precise model and rough model without considering the power loss in the absorption region. ....	97
Figure 4-7: Influence of detector tilting on the signal contrast.....	98
Figure 4-8: Dependence of the interference pattern contrast on the detector tilt angle....	99
Figure 4-9: Fabry-Perot cavity formation, dash line corresponds to the detector absorption region, $\rho$ , $\sigma$ the amplitude reflection and transmission of each mirror, $\rho^2=R$ and $\sigma^2=T$ .....	99
Figure 4-10: Light intensity at the detector absorption region versus the mirror position.....	100
Figure 4-11: The scheme of standing-wave Fourier-transform spectrometer, shown light field intensity does not consider the refractive difference of InP, InGaAs and InAlAs, and the DHPT circuit shows the floating base and sampling of $R_E$ . ....	102
Figure 4-12: Interference pattern from the DHPT with the scan mirror displacement, the coherent light source is a tunable laser with wavelength of 1500nm and output power of 1mW. ....	103
Figure 4-13: Waveform and Fourier spectrum of a single wavelength laser source, shown in the bottom figure four harmonic components $6667\text{cm}^{-1}$ (1 <sup>st</sup> order), $13334\text{cm}^{-1}$ (2 <sup>nd</sup> order), $20000\text{cm}^{-1}$ (3 <sup>rd</sup> order), and $26668\text{cm}^{-1}$ (4 <sup>th</sup> order).....	104
Figure 4-14: Waveform and Fourier spectrum of the interference pattern for light sources with two frequencies ( $6670\text{cm}^{-1}$ taken as reference, $7600\text{cm}^{-1}$ calculated from the calibration data).....	106
Figure 4-15: Fourier spectra for multiple wavelength coherent light sources, as the frequency difference reduced from 50nm to 30nm and 15nm, the harmonic order which can distinguish the two frequencies change from the 2 <sup>nd</sup> order to 3 <sup>rd</sup> and 4 <sup>th</sup> order.....	107

# CHAPTER 1 BACKGROUND

## 1.1 Infrared and IR systems

Over the extremely broad electromagnetic spectrum, the infrared (IR) region lies between visible light and microwave. The IR region is of great interest for applications in optical communication, remote sensing, chemical gas detection, solar cell technology, environmental monitoring and biological areas such as medicine and clinical analysis [1]. Infrared means “below red”, where *infra* comes from Latin meaning “below” and red being the visible light with the longest wavelength. IR covers a wide wavelength range from 700nm to 1mm and is divided into sub-regions: near infrared (NIR, IR-A) 0.7-1.4 $\mu$ m, short wavelength infrared (IR-B) 1.4-3 $\mu$ m, mid-wavelength infrared (IR-C) 3-8 $\mu$ m, long-wavelength infrared (8-15 $\mu$ m) and far infrared 15-1000 $\mu$ m. Different terms are used to refer to each of the IR regions based on various applications. For example, in the telecommunication field the interesting IR region is further divided into individual bands, which correspond to specific combinations of different light sources, detectors and fiber optical materials:

- O - band            1260–1360 nm
- E - band            1360–1460 nm
- S - band            1460–1530 nm
- C - band            1530–1565 nm
- L - band            1565–1625 nm
- U - band            1625–1675 nm

The NIR region from 700nm to 2.5 $\mu$ m covers most of the NIR IR-A and SWIR IR-B regions and is very important for optical non-destructive evaluation and inspection [2]. Compared to visible light and X-ray analysis, IR techniques have advantages because of the relative transparency of tissues and cells under IR illumination. Optical techniques, such as coherent anti-Stokes Raman spectroscopy (CARS) have demonstrated sensitivity at the single-molecule level with surface-enhanced techniques and non-invasive characterization capability [3, 4].

### 1.1.1 IR Detectors

A general IR system includes IR light sources (S), detectors (D), and often a component for transforming the light from multiple light sources or dispensing the light to multiple detectors (T). The light sources and detectors are essential for extending the wavelength of interesting applications in specific IR regions. Of all the possible materials with IR region emission and absorption, semiconductor materials have been widely investigated due to the fact that semiconductors are both very efficient sources and detectors and able to cover a wide range of wavelengths from the ultra-violet to the infrared. There are two groups of IR detectors, energy detectors and photon detectors (as shown in Table 1-1) [5]. Energy detectors respond to the temperature change under IR illumination due to a change in the property of the materials. They are normally low-cost and useful for single detector applications, such as fire detection and automatic light switch systems. Photon detectors link the signal to the free electric carrier generation through the interaction of incident photons and bound electrons. In the detector's history, PbS was the first to be successfully demonstrated with IR sensitivity out to  $3\mu\text{m}$  in 1940's. Later, silicon became the dominant material in the semiconductor industry mostly because its stable natural oxide is a nearly perfect insulator and enables complex processing. Silicon detectors have also been widely used in the visible and NIR region below  $1.1\mu\text{m}$ . It was well known that detectors with very high performance can be fabricated from Si, Ge, GaAs, InSb, InGaAs and HgCdTe (also known as MCT for mercury cadmium telluride) [6].

Inherent bandgap engineering techniques in compound semiconductor device technology make semiconductor IR detectors superior for many applications. For example,  $\text{In}_x\text{Ga}_{1-x}\text{As}$  detectors can cover a wide range from 700nm to  $3\mu\text{m}$  by changing the composition from gallium-rich ( $x < 0.5$ ) to indium-rich ( $x > 0.5$ ). In addition to the composition control of semiconductor materials, quantum structures, like quantum well (QWIP) [7] and quantum dot (QDIP) [8] systems enable changes in the effective bandgap of the active materials and have been utilized in modern IR sources and detector systems.

The detector performance is often the most critical factor of any IR SDT system. The interesting parameters of an IR detector include [9]: spectral response to define the

wavelength range of interest, detectivity to define the detector signal-to-noise ratio, responsivity to define the detector electrical signal output, response speed and frequency response to determine the system frequency, dark resistance to determine the dark current without any illumination, linearity to determine the range of irradiation over which the signal is linear to irradiance, effective optical area, field of view, package and so on. It is clear that sophisticated device structure design is as important as, if not more than, improving the material quality of active absorption regions.

**Table 1-1: IR detector type and material systems [5].**

Photon Detectors		Energy Detectors	
Intrinsic, PV	- MCT - Si, Ge - InGaAs - InSb, InAsSb	Bolometers	- Vanadium Oxide ( $V_2O_5$ ) - Poly-SiGe - Poly-Si - Amorph Si
Intrinsic, PC	- MCT - PbS, PbSe	Thermopiles	- Bi/Sb
Extrinsic	- SiX	Pyroelectric	- Lithium Tantalite (LiTa) - Lead Zirconium Titanite (PbZT)
Photo-emissive	- PtSi	Ferro-electric	- Barium Strontium Titanite (BST)
QWIP	- GaAs/AlGaAs	Micro cantilever	- Bimetals

P-I-N (three regions corresponding to p-type doped, intrinsic and n-type doped) photodiodes, MSM (metal-semiconductor-metal) detectors and bipolar phototransistors are three examples of the wide-range of detector families featuring easy fabrication processes and high performance for particular applications. Different from the linear responsivity of PIN and MSM detectors, phototransistors are known to be nonlinear devices with their electrical output signal not linearly proportional to the incident irradiance except over a limited “small signal” operating range. Recent developments in

micromachining technology make it possible to integrate IR light sources and detectors into a miniaturized sensing system-on-chip. InGaAs, compared to other semiconductors, is the most promising candidate for such purposes because of the mature InP technology developed for optical communications [10].

### 1.1.2 Coherence and coherent detection

NIR coherent photon detection is the main application of this dissertation. In chemistry and biology sensing and analysis, it is essential to distinguish coherent light waves with multiple wavelengths from a very noisy background [1]. For example, CARS is a very special coherent detection technique which has drawn a lot of attention recently, especially for the analysis of non-treated (non-tagged or non-stained) specimens [3]. “Coherence is the property wherein corresponding points on the wave-front are in phase” (D. J. Horowitz, Electronics Engineers handbook). The coherent feature of waves corresponds to the capability of forming immovable interference patterns. There are two kinds of coherence in nature, temporal coherence and spatial coherence. Spatial coherence is the coherent nature of light as a function of different positions at the same wave-front of point light sources (for example, stars) and has been developed into coherent imaging techniques in astronomy [11]. Temporal coherence is related to frequency and phase of the wave-front. The coherence of a light source is directly related to the linewidth of the emission and the coherence length,  $l$ , can be estimated from Eq. (1-1) [1],

$$l = \frac{\lambda^2}{\Delta\lambda} \quad (1-1)$$

For example, light emitted from a laser diode (highly-monochromatic with fixed phase difference among all the waves) is highly coherent and the coherent length can be larger than 1cm, while light emitted from a LED (light-emitting diode, not-highly monochromatic and random phase difference) has low-coherence and the coherent length on the order of a few  $\mu\text{m}$  (as shown in Fig. 1-1). Also shown in Fig. 1-1 is non-coherent white light from a lamp with multiple frequencies and random phase changes. For a

normal laser light source used in CARS microscopy, at a wavelength of 830nm and linewidth around 2GHz, the coherence length will be,

$$l = \frac{\lambda^2}{\Delta\lambda} = c / \Delta\nu = 0.15m$$

Coherent light sources are also very useful in the holography, which was first demonstrated with a coherent spectral line from a mercury-vapor lamp before the laser was even invented. Another example of coherent light sources is the Raman lines in CARS microscopy.

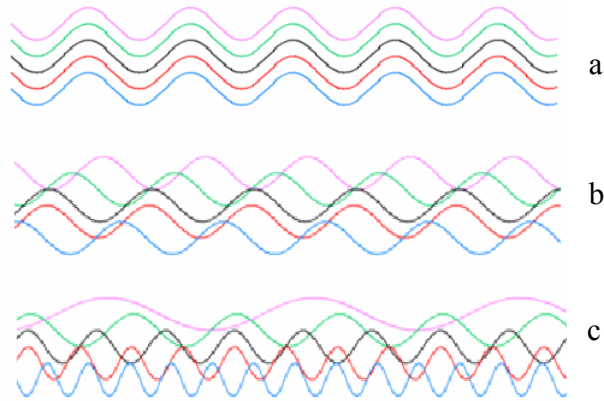


**Figure 1-1: Light waves from different light sources: (a) a laser (coherent light source); (b) a LED; (c) a white light lamp [1].**

### 1.1.3 Spectrometer

A general spectrometer in a SDT system is capable of identifying different spectrum components of the incident light with a specific combination of D (detectors) and T (transform components) [1]. A spectrum typically corresponds to the intensity pattern for specific individual frequency components. Important characteristics of the spectrometer include resolution, throughput and multiplexing [12].

The resolution of the spectrometer is the capability of the SDT system for identifying the frequency difference of two light waves:  $\Delta\lambda$ , the wavelength difference,  $\Delta k = \frac{2\pi}{\lambda^2} \Delta\lambda$ , the wave-number difference ( $k = \frac{2\pi}{\lambda}$ ), or  $\mathfrak{R} = \frac{\lambda}{\Delta\lambda}$  (all of these

definitions will be used on particular conditions). The system's power of collecting photons is defined as "throughput". It is highly dependent on the design of the system structure, and is related to the area and solid angle of the entrance aperture. The multiplexing factor of the spectrometer describes the capability of detecting multiple wavelength components simultaneously. Multiplexing spectrometers are also called "transform" spectrometers, employing transform mechanisms to identify simultaneously detected multiple wavelength components. Non-multiplex spectrometers incorporate a monochromator (a grating or a prism) which only sends a single position-dependent frequency light beam to the detector and the spectrum is generated by scanning the monochromator at a given rate. A Michelson spectrometer (shown in Fig. 1-2) is the most popular type of multiplex spectrometer. It is capable of high resolution spectral analysis with very broad frequency coverage. Light beams pass through the 50/50 beam splitter and are reflected by the fixed mirror and the movable mirror, respectively. An interference pattern forms at the detector where the two beams interfere with varying phase versus the position of the scanning movable mirror. This pattern is called an "interferogram" and normally has a burst feature (a very large magnitude) at the position where the beams reflected by the two mirrors experience equal distances from the incident surface of the beam-splitter to the detector plane. Fourier transforms can be used to analyze such interferograms.

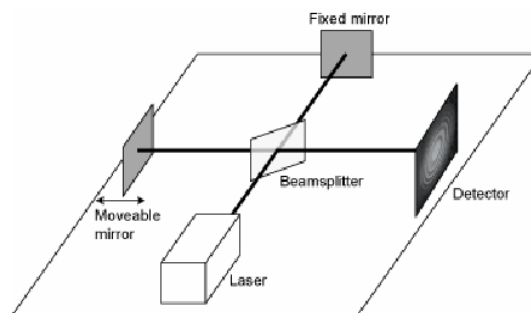


**Figure 1-2: Michelson spectrometer [1].**

Obviously a Michelson spectrometer is capable of spectrum analysis for both coherent and non-coherent light sources (white light interferometry is one example). The advantages of Michelson interferometry are as follows [12]. The multiplex ( Fellgett)

advantage comes from the fact that the incident light with all frequencies reaches the detector simultaneously, increasing the measurement speed  $M$  times, and the signal-to-noise ratio is  $\sqrt{M}$  times better than a monochromator, where  $M$  is the total number of resolution elements in the spectrum. The optical throughput (Jacquinot) advantage is related to the solid angle and the effective area of the light beams, which are greater for a Michelson spectrometer than those of a monochromator. Fourier transform infrared (FTIR) spectrometers can cover a wide range of infrared wavelength and have been commercially available since 1960's.

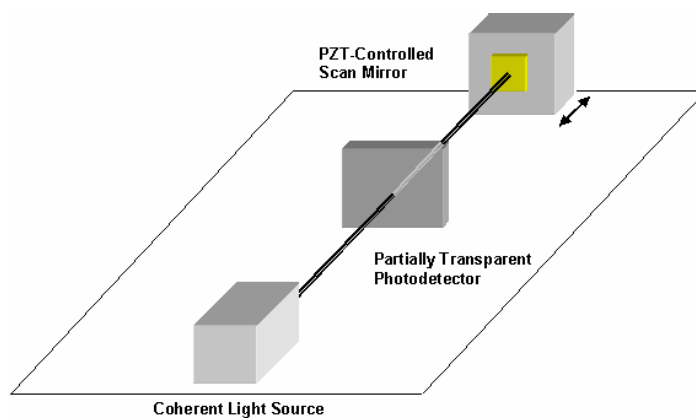


**Figure 1-3: Standing-wave Fourier-transform interferometer (folded Michelson spectrometer)**

As mentioned previously, low-resolution coherent detection is of great interest for most field applications. The folded Michelson spectrometer (shown in Fig. 1-3) eliminates the 50/50 beam splitter and combines the two mirrors (fixed and movable) into one scanning mirror [13]. The number of functional optical components is reduced from four to two, the scanning mirror and a partially transparent detector. The incident light beams pass through the detector with negligible absorption and are reflected by the highly reflective and conductive mirror. For coherent light sources, a standing wave light field can be formed by the forward and backward light beams. By scanning the mirror (effectively moving the detector in the immovable standing-wave light field), the interference pattern of the coherent light beam and a delayed version of itself is sampled by the detector using a square window in the spatial domain. Generally the resolution of the spectrometer only depends on the free travel length of the reflective mirror (the width

of the sampling window). In chapter 4, a new spectrum analysis technique will be investigated and higher resolution can be achieved for a fixed mirror travel length.

Compared to a normal FTIR spectrometer, the key point of the standing-wave FTIR (SWFTIR) interferometer is the partially transparent photo-detector, which should introduce negligible absorption loss of the incident light beams, but at the same time, provide a large enough electrical output signal for Fourier transform and spectrum analysis. There have been a lot of efforts making miniaturized spectrometer systems using surface and bulk micro-machining techniques [14-16]. Miniaturized SWFTIRs have been demonstrated with silicon-based micro-electric-mechanical system (MEMS) electrostatic mirrors and thin film photodiode detectors [17-19]. On the other hand, the system structure of SWFTIRs make them suitable for array applications in the field of hyperspectral sensing and imaging (shown in Fig. 1-4).

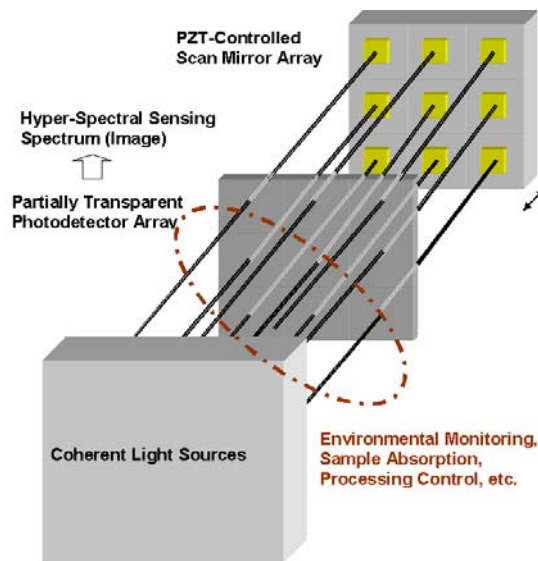


**Figure 1-4: Spectrometer arrays with standing-wave transform interferometer structure for hyper-spectral sensing and imaging applications.**

## 1.2 Semiconductor and Molecular Beam Epitaxy

Since high performance light sources and detectors are essential for a reliable IR SDT system, semiconductor materials with good qualities are highly desirable for device

fabrication. Molecular Beam Epitaxy (MBE) has been extensively investigated in the past three decades since A. Y. Cho at Bell labs in 1968 first demonstrated the capability of using molecular beams (modern solid-source MBE mostly uses atomic beams instead) to grow semiconductor materials with high crystal quality. The term of MBE was named two years later by Cho [20]. Although at that time the material quality grown by MBE was inferior to that grown by liquid phase epitaxy, MBE was believed to be one of the most promising methods to realize atomic layer control of single crystal semiconductor material growth. Another growth technology developed almost in the same era was Metal Organic Chemical Vapor Deposition (MOCVD) and later generally named as Metal-Organic Vapor Phase epitaxy (MOVPE). MOVPE has been widely utilized in the semiconductor industry mostly due to its better capability for multi-wafer growth and batch production. Recently, commercial MBE systems have demonstrated similar capabilities for multi-wafer growth in a production line [21]. Compared with MOVPE, MBE is more appropriate for research and development purposes because the growth parameters (chamber pressure, beam fluxes, temperature) are relatively independent instead of highly correlated with each other in MOVPE, so the optimization of growth can be more easily done. Readers interested in more details about the history and development of MBE technology should refer to the review articles in references [22-24].

Benefiting from four important technology improvements in a relatively short period, MBE became an effective high-quality material growth technique and resulted in tremendous successful developments of various electrical and optical devices. First, high-vacuum technology developed very rapidly and the background base pressure can reach the level of  $10^{-10}$ Torr ( $\sim 10^{-8}$ Pa) after several stage pumping and baking. Also key to achieving high-vacuum was the system design to provide an isolated growth chamber which is isolated from the sample loading chamber and transfer-tube to minimize the impurity levels carried with the substrates, holders, etc., during introduction into the MBE growth chamber. The second milestone was the development of high-temperature MBE system components. The next important improvement was low-defect epi-ready substrates, sample preparation methods and optimization of growth conditions. The last improvement was the development of high-purity source materials, substrates and Pyrolytic Boron Nitride (PBN) crucibles that eliminated the introduction of undesired

impurities and contamination during the growth period. The technology progress involved combining significant improvements over a broad range of different interdisciplinary fields. The developments in in-situ monitoring and controlling of the growth process, and in-situ and ex-situ characterization enabled researchers to continuously improve their understanding of the physics and real processes of epitaxial material growth [25].

### 1.2.1 Instruments, general principles, and techniques

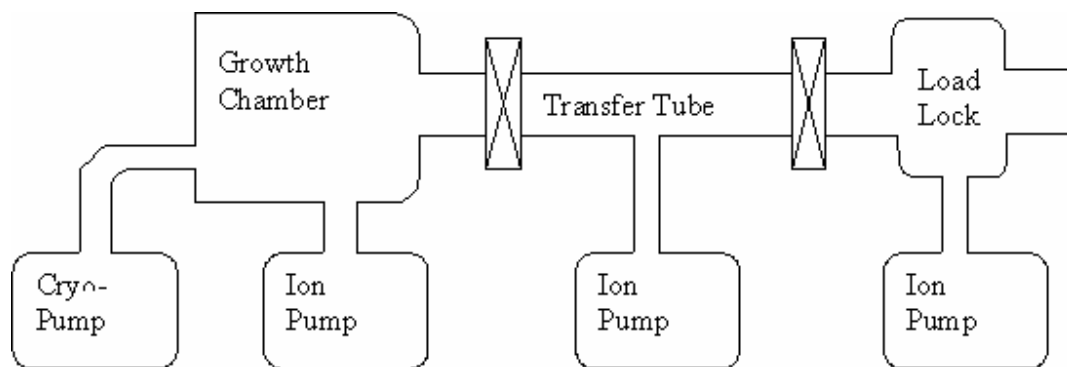


**Figure 1-5: Three-chamber MBE system: growth chamber, transfer tube and load lock.**

Fig. 1-5 shows a schematic diagram of the MBE system used in this dissertation. General MBE systems have most of these common features. Growth chamber, transfer tube and load lock are isolated by gate-valves and the ultra-high vacuum is maintained by a combination of ion-pumps and liquid-helium cryo-pumps. Liquid nitrogen flows in a large shroud inside the growth chamber to keep the base pressure in the  $10^{-11}$ Torr range. An alcohol and water mixed coolant at  $-10^{\circ}\text{C}$  flows in the source flange in order to minimize cross-interference or contamination of neighboring source cells. There are four basic types of source cells, small trumpet effusion cells for indium, SUMO effusion cells for gallium and aluminum, a needle-valved arsenic cracker cell, and dopant effusion cells for beryllium and silicon. As shown in Fig. 1-6, a substrate car rotation control system rotates the substrate around 10 revolutions per minute (rpm) to improve the epi-layer growth uniformity across the substrate surface. In-situ control systems include a residual gas analyzer (RGA) and reflective high-energy electron diffraction (RHEED). An ex-situ

optional optical reflectivity setup in the transfer tube is used to measure the thickness of epi-layers without taking partially grown samples out of the high-vacuum environment. It could also be used to monitor the grown film layer thickness for precise structure growth, for example, distributed Bragg reflector (DBR) mirrors in vertical cavity surface emitting lasers (VCSEL).

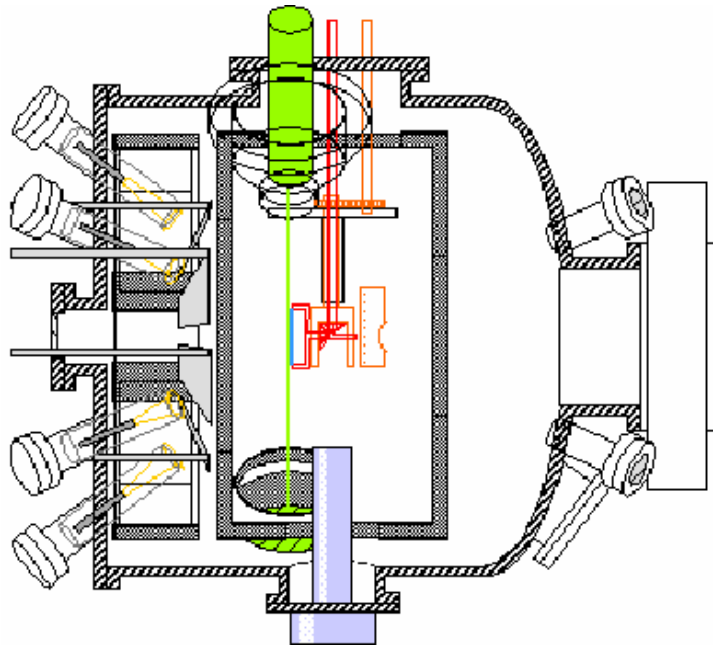


**Figure 1-6: Growth chamber of the MBE system: (from left to right) source flange with cells, RHEED gun and fluorescence screen, view port and gate valve to transfer tube. (From [www.snow.stanford.edu](http://www.snow.stanford.edu))**

The substrate preparation process is essential for high-quality material growth. A two-step thermal cleaning method has become the widely used procedure after commercial epi-ready substrates were available. The substrates normally come inside a nitrogen sealed package and have epi-ready surfaces which have mono-layer oxide top layers in order to protect the surfaces from contamination. The first step of baking (GaAs substrates at 350°C and InP substrates at 250°C) eliminates most of the water vapor incorporated during the loading process. The second step of thermal cleaning and deoxidization in the growth chamber further cleans the residual organic contamination and thin oxide protection layer on the surface of the substrate. The congruent temperature (alloy elements evaporate in equal proportions) of GaAs and InP are 580°C and 510°C,

respectively. Since it is not very easy to directly measure the surface temperature of the substrates, the deoxidization process has to be monitored by indirect methods. Reading through the thermal couple (TC) at the backside of the substrates is dependent on the substrate type (doping, polish, vendor and manufacture date) and mounting method. So other temperature measure methods are necessary at least for calibration procedures. An IR pyrometer is normally very useful for high-temperature measurement. Newer models of IR pyrometer could measure temperature as low as 300°C. Metal-semiconductor eutectic points are another reference useful for the whole calibration curve of TC and real temperature. For example, the eutectic point of silicon and aluminum is 570°C.

During the heating process of cleaning and deoxidization of the substrates, arsenic or phosphorous (for GaAs or InP substrates) will evaporate, so it is very important to have background arsenic or phosphorous overpressure (normally at the level of  $10^{-6}$ Torr) to inhibit the decomposition of substrates and so minimize the thermal damage to the substrate surface. For the thermal cleaning and deoxidization of InP substrates, arsenic overpressure can be used to stabilize the surface although it has more effect than inhibiting the decomposition process. Arsenic is more actively oxidized than phosphorous does. The thin oxide layer on the surface of InP ( $\text{InO}_x$  and  $\text{PO}_x$ ) will change to  $\text{AsO}_x$ , and then deoxidize even more easily [27, 28]. On the other hand, the exchange of arsenic and phosphorous will leave a very thin layer of InAsP on the surface after long-time thermal treatments. An appropriate buffer layer of InP (or InGaAs) will reduce the effects of such a thin layer [29].

Since MBE is basically a stoichiometric process of the reaction of molecular (atomic) beams of the constituent elements with a crystalline substrate surface, the precise control of the substrate temperature and source fluxes are very important for high-quality material growth by MBE [24]. Research on the kinetic processes in MBE has shown that for most compound semiconductors, the sticking coefficient of the group-III atoms is close to unity under normal growth conditions, while the sticking coefficient of group-V atoms is negligible unless group-III atoms are present and increases with the atom coverage [25]. Based on this fact, the composition control of ternary and quaternary materials with a single group-V element is only dependent on the ratios of group-III beam

fluxes. However, the growth control for materials with more than one group-V element is more difficult due to the non-unity sticking coefficient of group-V elements. In order to realize monolayer control of the epi-layer growth, the fluxes of all the source cells have to be controlled with precision better than one percent. The precise control of source fluxes is realized by feed-back loop control of the source temperatures within  $\pm 0.1^\circ\text{C}$  (Eurotherm power and controller modules). Despite the precise flux control before the epi-layer growth, in-situ closed-loop control is necessary for particularly complex structure growth (for example, quantum-cascade lasers) because of the flux drift due to source material loss during growth [30]. Different ex-situ methods described below were used to characterize the material quality and pre-calibrate the relationship between the source fluxes and growth rates.

High resolution X-ray diffraction (HRXRD), atomic force microscope (AFM), scanning electron microscope (SEM), tunneling electron microscope (TEM), secondary ion mass spectrometry (SIMS) and Rutherford back scattering (RBS) are several of the characterization techniques for assessment of structural qualities and composition analysis of epi-grown films. Photoluminescence (PL), deep-level transient spectroscopy (DLTS) and optical absorption are commonly used as characterization techniques for assessment of optical qualities and defect estimation.

### **1.2.2 Heteroepitaxy and lattice engineering**

MBE is a powerful materials growth technique to epitaxially grow ultra-thin layers with the same (homoepitaxy) or different (heteroepitaxy) materials from the substrates (shown in Fig. 1-7). High quality homojunction devices can be fabricated by doping the homoepitaxy layers. On the other hand, heterojunction devices with heterostructures, especially double heterostructures, can be fabricated using heteroepitaxially grown materials and are the research subject of more than two thirds of the semiconductor physics community (Z. I. Alferov, Nobel Lecture, 2001 [31]). Heteroepitaxy generally involves the issues of both lattice constant and energy band engineering. For the growth of different materials on substrates with the same or close lattice constants (for example,  $\text{In}_{0.532}\text{Ga}_{0.468}\text{As}$  on InP, AlAs on GaAs), the growth front will be smooth and defect-free.

Generally speaking, heteroepitaxy includes at least two lattice constants and the lattice mismatch (which may be as high as 16%, growth of GaN on sapphire  $\text{Al}_2\text{O}_3$ ) between the two materials is the origin of misfit strain and later defects during the epitaxial growth.

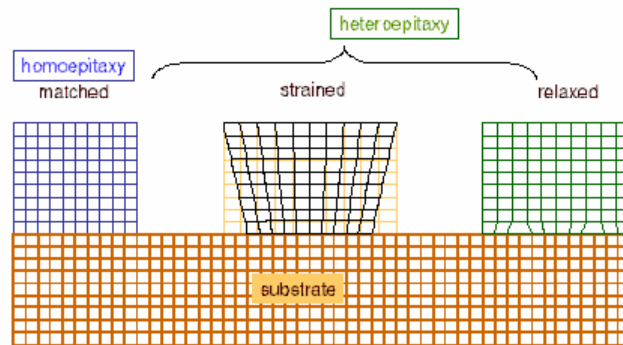


**Figure 1-7: Homoepitaxy and heteroepitaxy (including lattice matched, strained and relaxed systems) [32].**

As-grown layers with significant lattice-mismatch usually have rough surfaces and a high defect density. The defects incorporated into the layers include misfit dislocations at the layer-substrate interface, threading edge dislocations propagating to the outer surface of the layers, and other defects resulting from the strain and growth-condition dependent mechanisms (shown in Fig. 1-8). Among all the defects, misfit dislocations (MD) and threading dislocations (TD) are of great interest to both theoretical and experimental research because they are detrimental to device performance and may be controlled by optimizing the growth parameters. It is always beneficial to have a buffer layer with the same or close lattice constant to that of the device layers. Buffer layers function as a lattice transition from the substrate to the top device layers, providing a smooth and significantly lower defect density growth front, leaving strain-related defects behind.

In the history of MBE heteroepitaxial materials growth, single step buffers, multiple-step buffers, superlattices, and compositionally graded buffers have been utilized for different particular applications [33, 34]. Metamorphic growth with a step-graded buffer layer was later identified as one of the most successful techniques in many applications. This has been especially true in silicon technology (III-V on silicon, SiGe,

and silicon-on-insulator) and the “virtual substrate” technique has been extensively investigated [35].

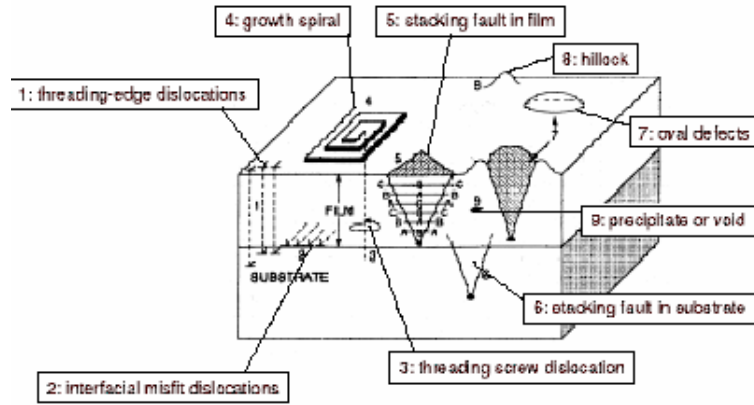


Figure 1-8: Defects in heteroepitaxy [32].

### 1.3 Indium Gallium Arsenide

On the diagram of bandgap energy versus lattice constant (shown in Fig. 1-9), InGaAs is a very important semiconductor material with a lattice constant 5.6533-6.0583Å and bandgap energy of 0.3-1.4eV [36, 37]. The lattice constant of InGaAs with 53.2% indium has the same lattice constant as InP, so it can be coherently grown on InP substrates defect-free without introducing misfit dislocations.  $\text{In}_{0.532}\text{Ga}_{0.468}\text{As}$  is also called “standard” InGaAs, compared to the wavelength-extended  $\text{In}_x\text{Ga}_{1-x}\text{As}$  on InP substrates ( $x > 0.532$ ) and on GaAs substrates (normally  $x < 0.3$ ). Strained and non-strained InGaAs of the same composition have different bandgap energies due to the effect of lattice strain on the band structure.

The lattice constant of  $\text{In}_x\text{Ga}_{1-x}\text{As}$  is,

$$a = 6.0583 - 0.405(1 - x) \quad (1-2)$$

and the bandgap energy of  $\text{In}_x\text{Ga}_{1-x}\text{As}$  for unstrained  $\text{In}_x\text{Ga}_{1-x}\text{As}$  on (001) GaAs with HH-LH (heavy hole - light hole) splitting = 0 is,

$$E_g(x) = 0.324 + 0.7(1-x) + 0.4(1-x)^2 \text{ eV} \quad (1-3)$$

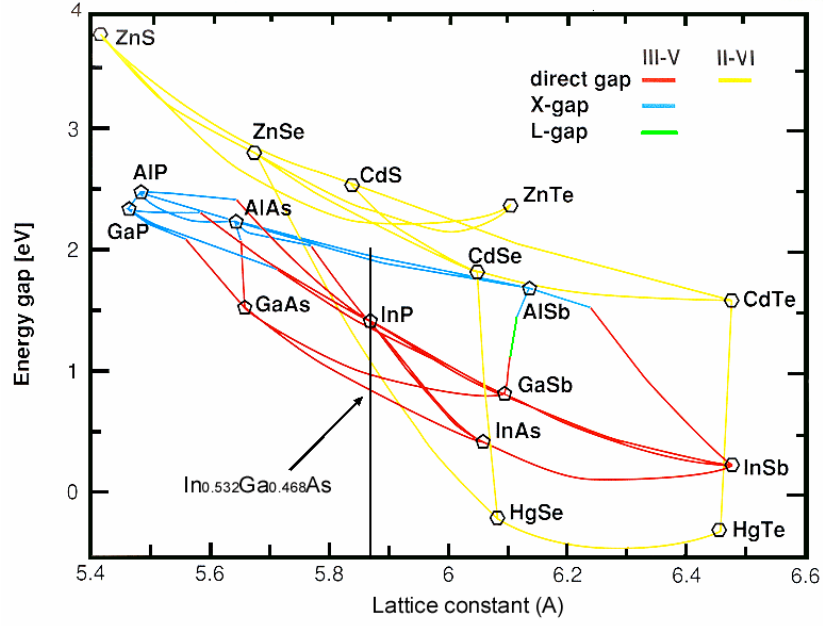


Figure 1-9: Diagram of bandgap energy versus lattice constant [37].

For strained  $\text{In}_x\text{Ga}_{1-x}\text{As}$  on (001) GaAs with small  $x$  ( $<0.2$ ) with HH-LH =  $0.42x\text{eV}$ , the bandgap energy is,

$$E_g(x) = 1.43 - 1.11x + 0.45x^2 \text{ (eV)} \quad (1-4)$$

For  $\text{In}_{x+0.532}\text{Ga}_{0.468-x}\text{As}$  grown on (001) InP substrates, the bandgap energy of unstrained material with HH-LH splitting = 0 is,

$$E_g(x) = 0.75 - 1.05x + 0.45x^2 \text{ (eV)} \quad (1-5)$$

and that of the strained material with HH-LH =  $0.42x\text{eV}$  is,

$$E_g(x) = 0.75 - 0.63x + 0.45x^2 \text{ (eV)} \quad (1-6)$$

For applications in the NIR region out to 2.5 $\mu\text{m}$  (bandgap energy of 0.5eV), relaxed (no residual strain) InGaAs needs to have an indium content more than 80%. On the other hand, strained InGaAs (coherent thin layer and defect free) has very good electrical and optical qualities for high-speed transistors (high electron mobility transistor, HEMT) and lasers [38]. The electron mobility of InGaAs (53.2% In, 13800  $\text{cm}^2/\text{Vs}$  at 300K and 70000  $\text{cm}^2/\text{Vs}$  at 77K) makes it among the best materials available for high-speed electrical devices [39].

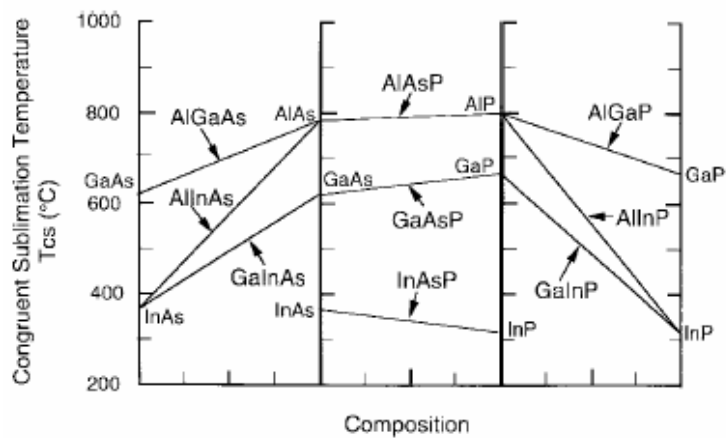


**Figure 1-10: Congruent sublimation temperatures for ternary III-V materials [25].**

The growth of high quality InGaAs lattice matched to InP substrates involves sophisticated calibration of the growth rates of indium and gallium (refer to section 1-2). Fortunately the growth rates are dependent only on group-III fluxes for materials with a single group-V element. For example, there will be 0.14% lattice mismatch for indium content change of only 2% in InGaAs. For ternary materials growth, several factors have to be monitored. Phase separation and lateral composition modulation have been identified long ago for alloy semiconductor materials growth [36, 40]. The MBE growth window (mainly substrate temperature, growth rate and group-V to group-III flux ratio) for high-quality material of ternary alloys is generally smaller than that of binary compounds. For example, the MBE growth of lattice matched InGaAs prefers a lower growth temperature and larger V/III flux ratios compared to GaAs growth, while the MBE growth of lattice matched InAlAs prefers a higher growth temperature and

relatively smaller V/III flux ratios. The substrate temperature for growing high quality materials is generally related to the congruent sublimation temperatures (as shown in Fig. 1-10). It is noticed that the congruent sublimation temperature of InGaAs decreases as the indium content increases.

#### 1.4 Summary

This dissertation is organized as follows: Chapter 2 describes the MBE growth of InGaAs-based, lattice matched material systems on InP substrates and mismatched material systems on InP and GaAs substrates, characterization of material properties and analysis of defect control; Chapter 3 focuses on photodetection device design, fabrication and characterization, including p-i-n photodiodes and n-p-n heterojunction bipolar phototransistors; Chapter 4 demonstrates a new technique of Fourier spectrum harmonic components analysis and the realization of a compact standing-wave Fourier-transform interferometer using a PZT-controlled scan mirror and a partially transparent photodetector; Chapter 5 summarizes the contribution of this dissertation.

#### References:

1. For general information about IR and IR systems, the online cyclopedia [www.wikipedia.org](http://www.wikipedia.org) and [www.answers.com](http://www.answers.com) will help on most technical terms and descriptions, other online magazines [www.spectroscopymag.com/spectroscopy/](http://www.spectroscopymag.com/spectroscopy/) and [www.spectrum.ieee.org](http://www.spectrum.ieee.org) include recent progresses on IR systems and spectroscopy, as well as sensing and detection.
2. O. S. Khalil, "Spectroscopic and clinical aspects of noninvasive glucose measurements", *Clinical Chemistry*, 45 (2) 165-177, 1999
3. J. X. Cheng, A. Volkmer, X. S. Xie, "Theoretical and experimental characterization of coherent anti-Stokes Raman scattering microscopy", *J. Opt. Soc. Am. B* 19 (6) 1363-1375, 2002
4. T. W. Koo, S. Chan, A. A. Berlin, "Single-molecule detection of biomolecules by surface-enhanced coherent anti-Stokes Raman scattering", *Opt. Lett.*, 30 (9) 1024-1026, 2005
5. General online resource [www.xenics.com/DOC/InfraredTechnology.doc](http://www.xenics.com/DOC/InfraredTechnology.doc)
6. P. R. Norton, "Infrared image sensors", *Opt. Engineering*, 30 (11) 1649-1663, 1991

7. B. F. Levine, "Quantum-well infrared photodetectors", *J. Appl. Phys.*, 74 (8) R1-81, 1993
8. J. Philips, P. Bhattacharya, S. W. Kennerly, D. W. Beekman, M. Dutta, "Self-assembled InAs-GaAs quantum-dot intersubband detectors", *IEEE J. Quantum Electron.*, 35 (6) 936-943, 1999
9. General online resource [www.calsensors.com/detectortech.html](http://www.calsensors.com/detectortech.html)
10. There are a number of good review papers on integrated optics, among them an excellent one is "Semiconductor photonic integrated circuits" by T. L. Koch and U. Koren, *IEEE J. Quantum Electron.*, 27 (3) 641-653 1991
11. P. G. Mezger, "Radio astronomy in the eighties", 13<sup>th</sup> European microwave conferences, 3-12, Sept. 5-8<sup>th</sup>, 1983
12. P. R. Griffiths, "Fourier transform infrared spectrometry", *Science, New Series*, 222 (4621) 297-302, 1983
13. D. A. B. Miller, "Laser tuners and wavelength-sensitive detectors based on absorbers in standing waves", *IEEE J. Quantum Electron.*, 30 (3) 732-749, 1994
14. R. D. Suenram, J. U. Grabow, A. Zuban, I. Leonov, "A portable, pulsed-molecular beam, Fourier-transform microwave spectrometer designed for chemical analysis", *Rev. Sci. Instruments*, 70 (4) 2127-2135, 1999
15. E. N. Lewis, P. J. Treado, I. W. Levin, "A miniaturized, no-moving-parts Raman spectrometer", *Appl. Spectroscopy*, 47 (5) 539-543, 1993
16. O. Manzardo, H. P. herzig, C. R. Marxer, N. F. Rooij, "Miniaturized time-scanning Fourier transform spectrometer based on silicon technology", *Opt. Lett.*, 24 (23) 1705-1707, 1999
17. H. L. Kung, S. R. Bhalotra, J. D. Mansell, D. A. B. Miller, J. S. Harris, "Standing-wave transform spectrometer based on integrated MEMS mirror and thin-film photodetector", *IEEE J. Sel. Top. Quantum. Electron.*, 8 (1) 98-105, 2002
18. S. R. Bhalotra, H. L. Kung, J. Fu, N. C. Helman, O. Levi, D. A. B. Miller, J. S. Harris, "Integrated standing-wave transform spectrometer for near infrared optical analysis", *Proceedings LEOS 105-106*, Glasgow, United Kingdom, 2002
19. D. Knipp, H. Stiebig, S. R. Bhalotra, E. Bunte, H. L. Kung, D. A. B. Miller, *IEEE Trans. Electron. Devices*, 52 (3) 419-426, 2005
20. T. E. Bell, "Alfred Yi Cho", *IEEE Spectrum*, 31, 70-73, 1994
21. Information from the most important MBE system and components vendor, [www.veeco.com](http://www.veeco.com), as well online magazine III-V reviews.
22. "An introduction to MBE growth", <http://www.ece.utexas.edu/projects>
23. A. Y. Cho, J. R. Arthur, "Molecular beam epitaxy", *Progress in Solid State Chemistry*, 10 (3) 157-191, 1975
24. "Molecular beam epitaxy: fundamentals and current status", by M. A. Herman, 2<sup>nd</sup> ed., Berlin, New York, Springer, 1996; "Molecular beam epitaxy – applications to

- key materials”, by R. F. C. Farrow, William Andrew Publishing, “molecular beam epitaxy of high-quality GaAs and AlGaAs” by E. C. Larkins and J. S. Harris, Jr., pp. 114-274 (online version: <http://www.knovel.com/knovel2/Toc.jsp?SpaceID=10059&BookID=140>)
25. K. Y. Cheng, “Molecular beam epitaxy technology of III-V compound semiconductors for optoelectronic applications”, *Proceedings of IEEE*, 85 (11) 1694-1714, 1997
  26. V. Tank, H. Dietl, “Multispectral pyrometer for temperature measurement with automatic correction of the influence of emissivity”, *Infrared Physics*, 30 (4) 331-342, 1990
  27. J. F. Wager, D. L. Ellsworth, S. M. Goodnick, C. W. Wilmsen, “Composition and thermal stability of thin native oxides on InP”, *J. Vac. Sci. Technol.*, 19 (3) 513-518, 1981
  28. G. Hollinger, E. Bergignat, J. Joseph, Y. Robach, “On the nature of oxides on InP surfaces”, *J. Vac. Sci. Technol. A*, 3 (6) 2082-2088, 1985
  29. E. Tournie, Y. H. Zhang, N. J. Pulsford, K. Ploog, “Structural and optical properties of Al<sub>0.48</sub>In<sub>0.52</sub>As layers grown on InP by MBE: influence of the substrate temperature and of a buffer layer”, *J. Appl. Phys.*, 70 (12) 7362-7369, 1991
  30. S. R. Johnson, E. Grassi, M. Beaudoin, M. D. Boonzaayer, K. S. Tsakalis, Y. H. Zhang, “Closed-loop control of composition and temperature during the growth of InGaAs lattice matched to InP”, *J. Vac. Sci. Technol. B*, 17 (3) 1237-1240, 1999
  31. Z. I. Alferov, “Nobel lecture: the double heterostructure concept and its applications in physics, electronics and technology”, *Rev. Mod. Phys.*, 73 (3) 767-782, 2001
  32. Diagrams taken from the personal research project regarding to the epitaxial growth of film on substrates, defect generation and categorization, <http://fy.chalmers.se/~yurgens/epitaxy.pdf>
  33. F. W. Smith, A. R. Calawa, C. L. Chen, M. J. Manfra, L. J. Mahoney, “New MBE buffer used to eliminate backgating in GaAs MESFETs”, *IEEE Electron Device Letters*, 9 (2) 77-80, 1988
  34. P. Sheldon, B. G. Yacobi, K. M. Jones, D. J. Dunlavy, “Growth and characterization of GaAs/Ge epilayers grown on Si substrates by MBE”, *J. Appl. Phys.*, 58 (11) 4186-4693, 1985
  35. E. Kasper, K. Lyutovicj, M. Bauer, M. Oehme, “New virtual substrate concept for vertical MOS transistors”, *Thin Solid Films*, 336 (1-2) 319-322, 1998
  36. “Properties of lattice matched and strained Indium Gallium Arsenide”, by P. Bhattacharya, INSPEC, 1993
  37. [http://www.tf.uni-kiel.de/matwis/amat/semi\\_en/kap\\_5/backbone/r5\\_1\\_4.html](http://www.tf.uni-kiel.de/matwis/amat/semi_en/kap_5/backbone/r5_1_4.html)
  38. J. J. Rosenberg, M. Benlamri, P. D. Kirchner, J. M. Woodall, G. D. Pettit, “An In<sub>0.15</sub>Ga<sub>0.85</sub>As/GaAs pseudomorphic single quantum well HEMT”, *IEEE Electron Device Letters*, 6 (10) 491-493, 1985

39. I. Suemune, L. A. Coldren, M. Yamanishi, Y. Kan, "Extremely wide modulation bandwidth in a low threshold current strained quantum well lasers", *Appl. Phys. Lett.*, 53 (15) 1378-1380, 1988
40. M. A. Marciniak, R. L. Hengehold, Y. K. Yeo, G. W. Turner, "Optical characterization of MBE grown InAsSb nearly lattice matched to GaAs", *J. Appl. Phys.*, 84 (1) 480-488, 1998

## CHAPTER 2 INGAAS-BASED MATERIAL SYSTEMS: GROWTH AND CHARACTERIZATION

High quality semiconductor materials are essential to the fabrication of IR sources and detectors for a high performance SDT IR system. InGaAs based material systems grown by solid-source MBE are investigated for NIR detection. The general principles, instruments and operation procedures of MBE have been described in chapter 1 and this chapter will focus on the materials growth and characterization of the structural and optical properties. The ultimate goal is to grow high quality materials for light sources and detectors in the NIR region out to 2.5 $\mu$ m. Three different material systems are studied, including lattice-matched InGaAs and InGaAs(NSb) material systems grown on InP substrates, highly strained pseudomorphic In<sub>x</sub>Ga<sub>1-x</sub>As/In<sub>y</sub>Ga<sub>1-y</sub>As materials system with quantum structures grown on InP substrates, and relaxed metamorphic thick In<sub>(x>0.7)</sub>GaAs device layers grown on InP and GaAs substrates.

### 2.1 Lattice-matched material systems on InP substrates

InP and GaAs substrates are extensively used for the growth of III-V semiconductors by MBE or MOVPE. Four-inch InP substrates and six-inch GaAs substrates have been commercially available with epi-ready quality surfaces [1]. The lattice constant of GaAs is 5.6533 $\text{\AA}$  and that of InP 5.8688  $\text{\AA}$ . On the diagram of bandgap energy vs. lattice constant (Fig. 1-9), InP substrates are shown to be more flexible for the growth of materials sensitive in the near IR region out to 2.5 $\mu$ m. The fast development of InP technology in the fields of optical and wireless communications have enabled extensive investigation of lattice-matched (LM) material systems epitaxially grown on InP substrates, including In<sub>0.532</sub>Ga<sub>0.468</sub>As, In<sub>0.523</sub>Al<sub>0.477</sub>As, (In<sub>0.532</sub>Ga<sub>0.468</sub>)<sub>x</sub>(In<sub>0.523</sub>Al<sub>0.477</sub>)<sub>1-x</sub>As, In<sub>1-x</sub>Ga<sub>x</sub>As<sub>y</sub>P<sub>1-y</sub> ( $x = 0.468y$ ), GaAs<sub>0.5</sub>Sb<sub>0.5</sub>, and others [2-7].

#### 2.1.1 InGaAs and InAlAs

In<sub>0.532</sub>Ga<sub>0.468</sub>As and In<sub>0.523</sub>Al<sub>0.477</sub>As are among the most important materials which lattice-match to InP substrates. With precise composition control, the layer thickness of

both materials is not limited. In addition, InP,  $\text{In}_{0.532}\text{Ga}_{0.468}\text{As}$  and  $\text{In}_{0.523}\text{Al}_{0.477}\text{As}$  produce high-quality buffers for further epitaxial material growth by burying residual contamination and defects which are on the surface and in the substrates.

Our GEN-II MBE system is equipped with a GaP sublimation source, providing a phosphorous overpressure environment and growth of thin InP buffer layers. The volume of the GaP cell is very limited and the sublimation efficiency is not high enough for thick phosphide layer growth [8]. Although it would be ideal to deoxidize the substrate in a phosphorous overpressure atmosphere, an optimized deoxidization process can also be relatively successful in arsenic overpressure atmosphere [9-11]. There are several temperature points that are important to keep in mind for high-quality material growth:  $\text{P}_2$  desorbs from InP substrates at  $\sim 300^\circ\text{C}$ ,  $\text{P}_4$  desorbs at higher than  $650^\circ\text{C}$ , In desorbs at  $\sim 500^\circ\text{C}$ , the InP sublimation temperature is  $\sim 360^\circ\text{C}$ , and the surface oxide decomposes at  $\sim 500^\circ\text{C}$ . At a substrate temperature of  $300^\circ\text{C}$ , the InP substrate will desorb  $\text{P}_2$  and thermal damage (for example, a rough surface) occurs if there is no group-V element overpressure to prevent it from happening. Generally an arsenic overpressure environment on the order of  $10^{-6}\text{Torr}$  is used to protect the surface from thermal damage, and then the substrate temperature was ramped at a rate of  $15^\circ\text{C}/\text{min}$  to  $\sim 600^\circ\text{C}$  with the RHEED monitoring the deoxidization process. Since arsenic atoms are more active than phosphorous atoms, the exchange of atomic sites in InP substrates with arsenic atoms helps the deoxidization process. The main oxide materials found on InP substrate surfaces include:  $\text{InO}_x$ ,  $\text{PO}_x$ ,  $\text{In}(\text{OH})_3$ ,  $\text{InPO}_4$  and  $\text{In}(\text{PO}_3)_3$ , which will change to  $\text{AsO}_x$  and decompose during the deoxidization process [10, 11]. Although it is generally accepted that the deoxidization and surface reconstruction temperature is  $510^\circ\text{C}$ , the thermal couple (TC) temperature used to monitor the growth is dependent on various factors including: substrate doping type, mounting method, vendor and freshness of the substrates, loading environment and others.

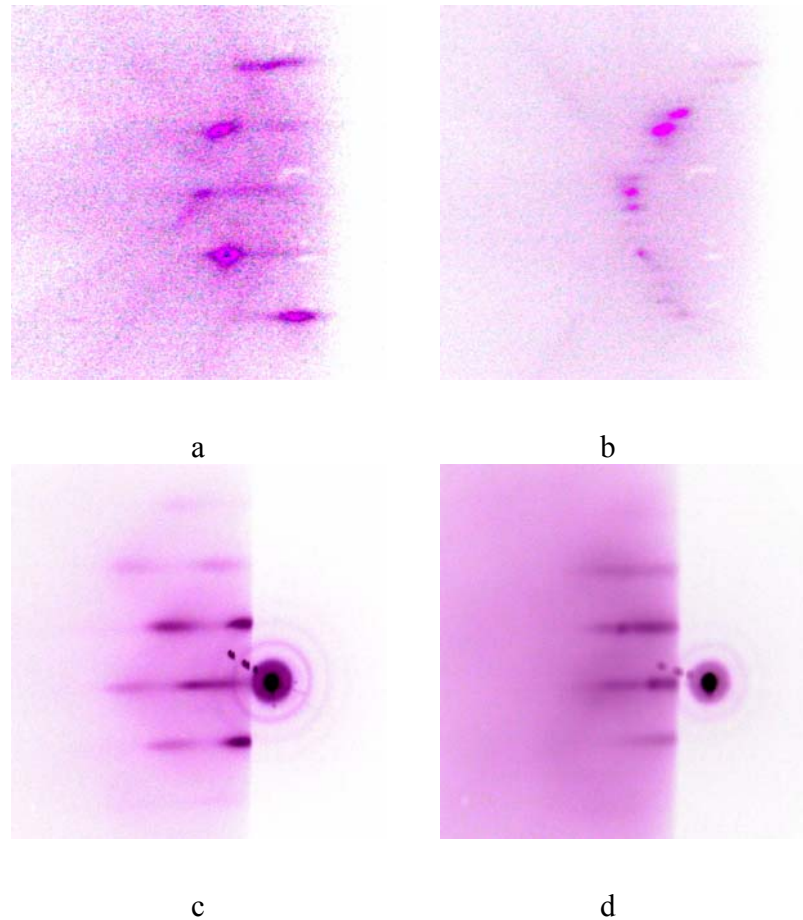


**Figure 2-1: RHEED patterns during the InP deoxidization process and InGaAs epi-layer growth: surface reconstruction (2×4) with two-fold (a) and four-fold (b), starting of epi-layer growth (c) and after several monolayer of InGaAs growth (d).**

During the deoxidization process monitored by RHEED, Kikuchi lines, bright spots, bright streaks, and bright (2×4) surface reconstruction patterns (As-rich two manifold and group-III-rich four manifold, shown in Fig. 2-1 (a) and (b)) appear sequentially at different stages with increasing substrate temperatures. After clear (2×4) surface reconstruction patterns were identified, the InP substrate was cooled quickly to the growth point (TC 500°C for InGaAs and TC 525°C for InAlAs on n-type Sn-doped InP substrates, TC 520°C for InGaAs and TC 545°C for InAlAs on semi-insulating Fe-doped InP substrates). If the source fluxes were carefully calibrated and the lattice constant of the grown materials is exactly matched to the InP substrates, two-dimensional growth will be the starting mode and the RHEED patterns maintain their streaky features from the beginning of the growth. Actually the lattice mismatch of the grown materials to

InP substrates can only be controlled to no better than  $3.4 \times 10^{-4}$  on condition that the source flux be controlled with 1% precision. So normally at the very beginning of the growth, spotty RHEED patterns will be first observed partly because of the thermal damage during the deoxidization process and partly due to the lattice mismatch between the epi-layers and the substrates. The thermal damage at the surface of the substrates can be healed by atomic diffusion [12], so if the lattice mismatch is below a threshold value (an empirical estimation from the material investigation in this dissertation is around 0.15%, corresponding to indium content deviation about 2%) the RHEED patterns will return to their initial streaky appearance after several monolayers of growth of either InGaAs or InAlAs and keep this streaky feature thereafter (as shown in Fig. 2-1 (c) and (d)). Generally speaking, the RHEED pattern is surface-roughness dependent and streaky patterns normally represent an atomically smooth surface.

Fig. 2-2 shows the X-ray diffraction (XRD, Philips X'Pert) rocking curve of three InGaAs layers grown on InP substrates with the same layer thickness of 500nm and same arsenic-overpressure environment during the deoxidization process. The compositions of the three epi-layers were calculated from the XRD simulation (X'pert epitaxy) as  $\text{In}_{0.470}\text{Ga}_{0.530}\text{As}$ ,  $\text{In}_{0.513}\text{Ga}_{0.487}\text{As}$  and  $\text{In}_{0.533}\text{Ga}_{0.467}\text{As}$ . Correspondingly, the mismatch strain between the layers and the substrates are -0.43%, -0.13% and 0.01%, respectively. The lattice match condition of epi-grown InGaAs and InAlAs layers can be controlled at the level of  $5.0 \times 10^{-4}$  with good reproducibility.

Digital grading superlattices (DGS) of  $\text{In}_{0.532}\text{Ga}_{0.468}\text{As}/\text{In}_{0.523}\text{Al}_{0.477}\text{As}$  can be grown on InP substrates and pseudo-substrate buffer epi-layers because of the lattice-match features of both materials. The digital growth technique is realized by computer-automated motion control of all the related source shutters. DGS structures of InGaAs/InAlAs can be used to build graded heterojunctions and act as transition layers to enhance the Schottky barrier of MSM detectors to reduce the dark current without degrading the carrier collection efficiency. The growth scheme of a typical DGS structure is shown in Fig. 2-3. This DGS has 19 periods of InGaAs/InAlAs (ratio of thickness change from 19:1 close to the InGaAs side to 1:19 close to the InAlAs side). The thickness of each period is 10nm and that of the total DGS layers is 190nm. Also shown

in the figure is the effective conduction and valence band structures based on mini-band theory.

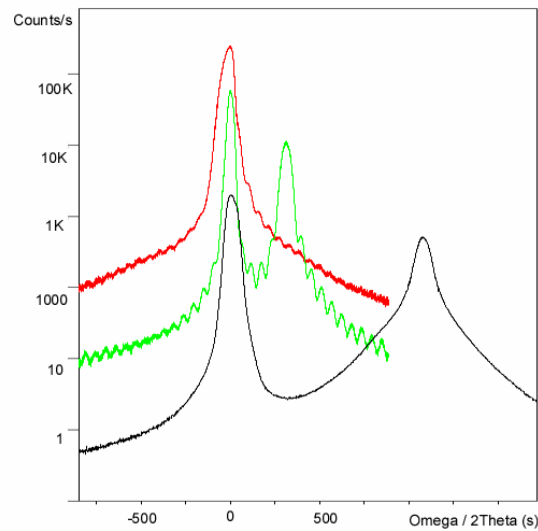


**Figure 2-2: XRD rocking curve of InGaAs layers grown on InP substrates ((100),  $\omega/2\theta$  (004) scan) with different compositions from highly mismatch to lattice-match conditions.**

The structural quality of the DGS sample can be characterized by XRD rocking curve (shown in Fig. 2-4). The composition of the InAlAs layers is intentionally adjusted off lattice-match condition with 0.17% misfit strain, and the composition of InGaAs layers fulfills the lattice-match condition on InP substrates (mismatch less than  $5 \times 10^{-4}$ ). Optical characterization methods, such as room-temperature photoluminescence and optical absorption (transmission) are used to characterize the optical quality of the material qualities of DGS samples (shown in Fig. 2-5 and 2-6). Application of DGS in the device design will be described in the next chapter.

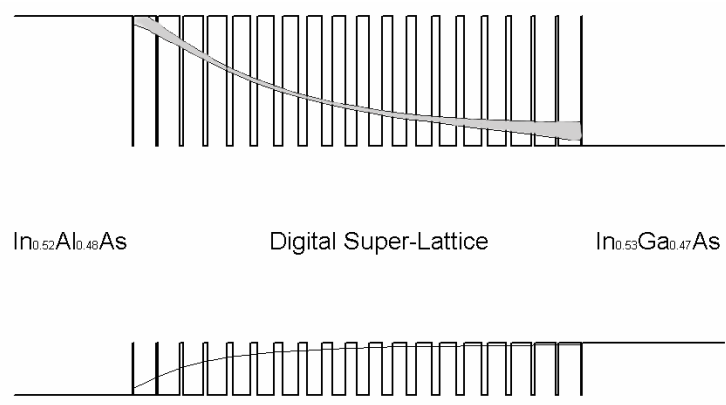


**Figure 2-3: DGS structure as a transition layer between InGaAs and InAlAs layers.**

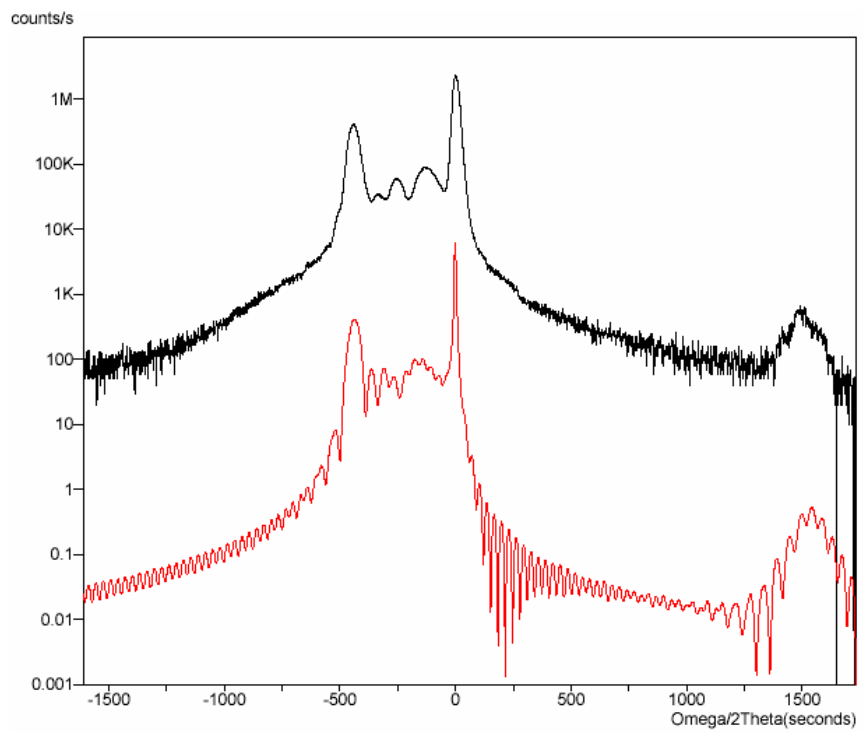


**Figure 2-4: XRD rocking curve of DGS sample (top curve) and simulation (bottom).**

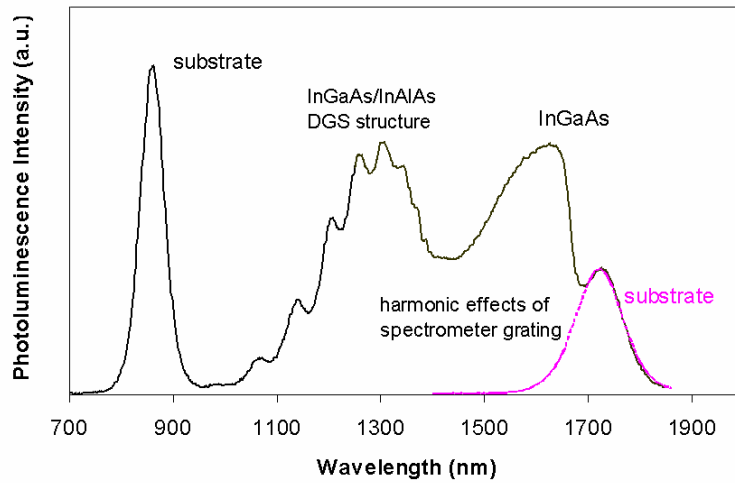


Figure 2-5: Room-temperature photoluminescence of DGS sample, the emission of substrate peak deviate from InP substrate (1.34eV, 925nm) due to off-calibration of the PL system at that wavelength. Second harmonic response of grating in the spectrometer is shown and InGaAs emission peak asymmetry comes from the responsivity drop of the detector beyond 1.6 $\mu$ m.

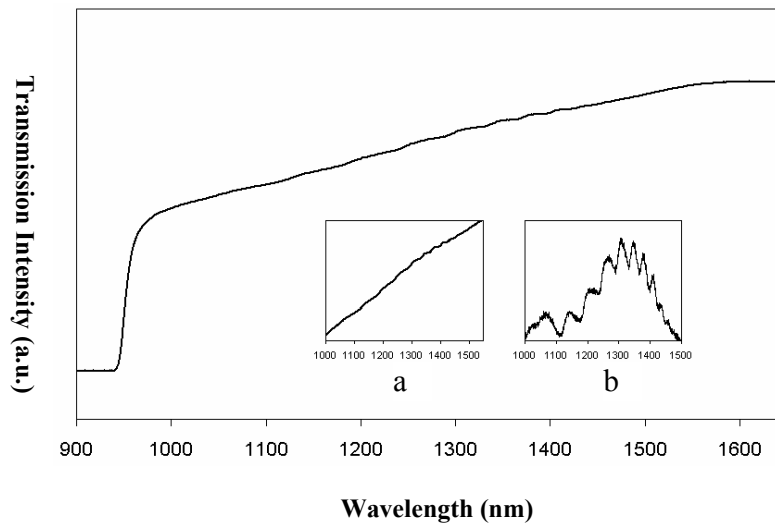


Figure 2-6: Room-temperature optical absorption (transmission) measurement of the DGS sample with absorption edge at 1.6 $\mu$ m, minibands absorption effects shown in the inset diagrams and InP substrate absorption at 925nm: (inset diagrams) (a) details at 1000-1500nm; (b) curve features with the removal of linear background.

### 2.1.2 InGaAs(NSb)

GaInNAs/GaAs has been extensively studied as a substitute material system for InGaAsP/InP in the pursuit of lower cost and more efficient lasers in optical communications [13, 14-16]. There were several theories explaining the mechanisms of bandgap narrowing for nitrogen incorporation in GaAsN or GaInNAs [17-19]. One of the generally accepted explanations is that the incorporated nitrogen atoms distorted the local crystal structures because of the very small atomic size and overlapping wavefunctions correspond to a localized level in the conduction band and anti-crossing of the conduction band, and localized level produce bonding and anti-bonding bands, which effectively reduce the bandgap energy of the alloy [18]. With additional antimony atoms incorporated in the active region, the crystal and optical quality of dilute nitride layer can be significantly improved and the operating wavelength can be extended further from 1.3 $\mu\text{m}$  to 1.55 $\mu\text{m}$  which covers the entire S-C-L bands of long-haul optical communications [20, 21]. Since the incorporation of nitrogen atoms and antimony atoms corresponds to different strain conditions, more lattice-matched materials can be grown on the InP substrates. According to Vegard's law, the lattice-match condition for  $\text{Ga}_{0.47}\text{In}_{0.53}\text{N}_x\text{As}_{1-x-y}\text{Sb}_y/\text{In}_{0.53}\text{Ga}_{0.47}\text{As}/\text{InP}$  is that  $x:y$  equals to 1:2.56. Dilute nitride and antimonide grown on InP substrates can be sensitively emitting or absorbing photons in the wavelength range of NIR out to 2.5 $\mu\text{m}$ .

The relevant samples were grown in a Varian Gen-II MBE system-V, which is different from the system-I described before in this dissertation. System-V is equipped with indium and gallium SUMO-cells (Applied Epi, Veeco). By controlling the temperatures of both the tip and base zones of the cells, stable source fluxes can be maintained during the MBE growth to keep the composition of lattice-match condition on InP substrates. The arsenic source is a precisely controlled needle-valve cracker with the sublimation region set to 390°C and the cracking zone set to 800°C. The antimony source is a non-valved cracker cell with two heating zones which are maintained at idle temperatures when not used. During epitaxial layer growth, the flux of arsenic is monitored by the needle-valve position, and the flux of antimony is controlled by the sublimation zone temperature (450-490°C) while the cracking zone temperature was kept

at 850°C. The nitrogen source is a modified SVT plasma source with the highest rf-power of 300W and ultra-clean nitrogen gas flow up to 20sccm (standard cubic centimeter per minute).

The surface cleaning process was the same as described earlier: the substrate was first heated to 300°C quickly and then ramped to 600°C (TC, corresponding to the real substrate temperature around 510°C) with a ramping rate of 20°C/min in an arsenic-overpressure environment with arsenic beam equivalent pressure (BEP) flux of  $10^{-6}$ Torr. After a  $2\times 4$  surface reconstruction pattern was clearly recognized by RHEED, the substrate was cooled quickly to TC500°C and an  $\text{In}_{0.53}\text{Ga}_{0.47}\text{As}$  buffer layer was grown, followed by the test structures. The structure of the samples is shown in Fig. 2-7, including the capping layer, the cladding layer and the buffer layer LM-InGaAs. The thickness of the thin layer of  $\text{Ga}_{0.47}\text{In}_{0.53}\text{N}_x\text{As}_{1-x-y}\text{Sb}_y$  was between 20nm and 50nm. There was a transition layer of LM-InGaAs after the buffer layer growth with the substrate temperature gradually cooled down to 370-390°C. The nitrogen plasma was ignited 10-15 minutes before the single quantum well (SQW) layer growth. The use of a transition layer reduces non-radiative defects in the SQW layer because of the operation instability of plasma cells when first ignited. The background N level at a growth rate of 0.5 $\mu\text{m/hr}$  was around 0.15% when the plasma was ignited and shutter was closed.

**Table 2-1: Growth conditions for three test samples with same N cell condition.**

sample	Indium	Gallium	Arsenic	Antimony
1	$1.42\times 10^{-7}$ Torr 0.167 $\mu\text{m/hr}$	$8.80\times 10^{-8}$ torr 0.148 $\mu\text{m/hr}$	$3.5\times 10^{-6}$ torr	$5.88\times 10^{-8}$ torr
2	$2.20\times 10^{-7}$ torr 0.257 $\mu\text{m/hr}$	$1.36\times 10^{-7}$ torr 0.228 $\mu\text{m/hr}$	$5.4\times 10^{-6}$ torr	0
3	$2.20\times 10^{-7}$ torr 0.257 $\mu\text{m/hr}$	$1.36\times 10^{-7}$ torr 0.228 $\mu\text{m/hr}$	$5.4\times 10^{-6}$ torr	$7.68\times 10^{-8}$ torr

Three different samples were grown (as shown in Table 2-1 and Fig. 2-7): sample 1 has a GaInNAsSb SQW layer thickness of 50nm and both of the cladding and capping layers 150nm, samples 2 and 3 have the same SQW thickness of 20nm for GaInNAs

(sample 2) and GaInNAsSb (sample 3) with cladding and capping layer thicknesses of 80nm. The gas flow (10% of 20sccm) and rf-power (300W) of the nitrogen plasma cell were kept the same for the growth of all three samples and the flux ratio of group-V/group-III was between 15~20.

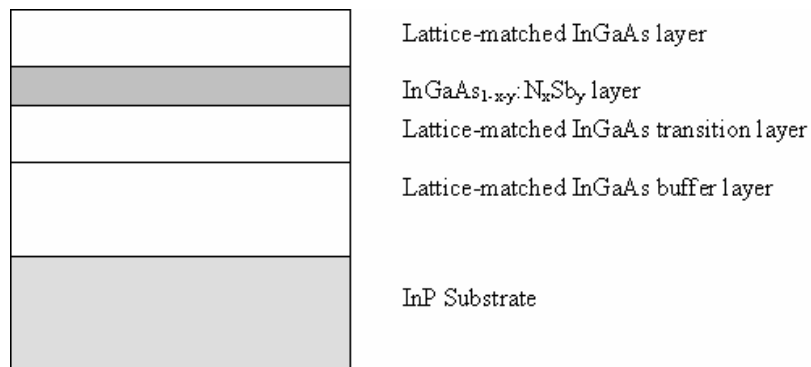


**Figure 2-7: SQW samples grown by MBE.**

The solubility of nitrogen atoms in bulk semiconductor materials is theoretically expected to be very low [22, 23]. However, it was found that up to 14.8% N could be incorporated in GaAsN layers without phase segregation for particular growth conditions [24]. Due to the different bond strength of InNAs and GaNAs, phase segregation was expected to happen for either high nitrogen concentration or non-optimized growth conditions [25]. Since phase segregation would severely degrade the material quality, it was essential to optimize the growth conditions for dilute nitride growth. As mentioned previously, the operating condition of the nitrogen plasma cell was kept the same for the growth of all the samples so that the optimization of stability, plasma beam intensity and purity (free of ions) of the plasma cell would be independent of the growth conditions. The N content in the QW region was controlled by changing the growth rate (determined by group-III elements, as described in Chapter 1) and was dependent on the substrate temperature during growth. The incorporation of nitrogen atoms in the QW was basically a meta-stable process, so low growth temperature (more than 100°C below the normal LM-InGaAs growth) was preferred to achieve relatively smooth growth surfaces.

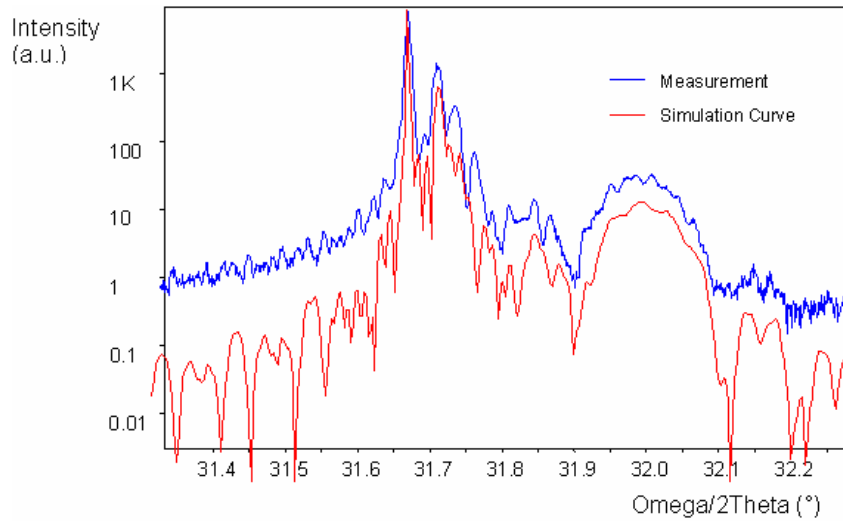


**Figure 2-8: High-resolution XRD rocking curve of sample 1 with the thickness of SQW 50nm, measurement and simulation curves matched well.**

XRD rocking curves and SIMS depth profiling analysis were used to characterize the composition and structural quality of sample 1 (shown in Fig. 2-8 and 2-9). The nitrogen and antimony content were identified to be 3.5% and 3%, respectively. The composition of the SQW in sample 1 was characterized to be  $\text{Ga}_{0.47}\text{In}_{0.53}\text{N}_{0.035}\text{As}_{0.935}\text{Sb}_{0.03}$  and there was a tensile strain of 0.9% to the cladding layers and the InP substrate. No evidence of phase separation (XRD peaks of GaN, InN, GaAs, InAs, GaSb, or InSb) can be found in the wider Omega scan (not shown) in the XRD measurement. The positions of peaks in the XRD rocking curve measurements were dependent on both of the material composition and strain. For materials with multiple group-III and group-V ingredients, it would be possible to get the same XRD simulation with different compositions. So XRD can only be regarded as a reliable material characterization method when combined with other characterization methods, for example, SIMS or RBS. Fig. 2-9 shows that it was not a trivial effect that indium atoms segregate with a higher ratio in the QW at the top surface of growth front.

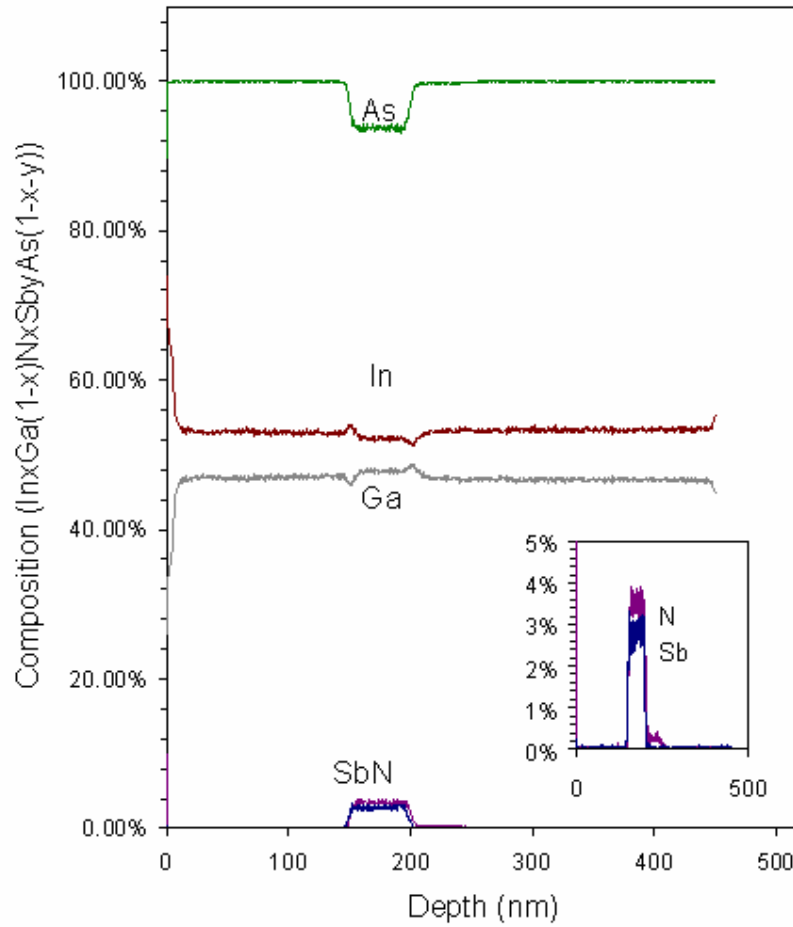


**Figure 2-9: SIMS depth profiling analysis of sample 1, inset figure showing the nitrogen and antimony content in the QW region.**

The N composition (N%) was inversely proportional to the growth rate ( $gr$ , in  $\mu\text{m/hr}$ ) of group III (In+Ga) for the growth of GaInNAs on GaAs in Eq. (2-1),

$$N\% = \frac{A_{GaAs}}{gr_{Ga} + gr_{In}} \quad (2-1)$$

where  $A_{GaAs}$  is a growth and system dependent constant and one best fit of different samples with various growth conditions leads to a nitrogen incorporation factor  $A \sim 1.0$  [25,26]. However, it would be a different story for growing samples 2 and 3 with both nitrogen and antimony in the QW region. During the growth of SQW samples, the RHEED patterns showed that nitrogen atoms roughen the surface (streaky for InGaAs



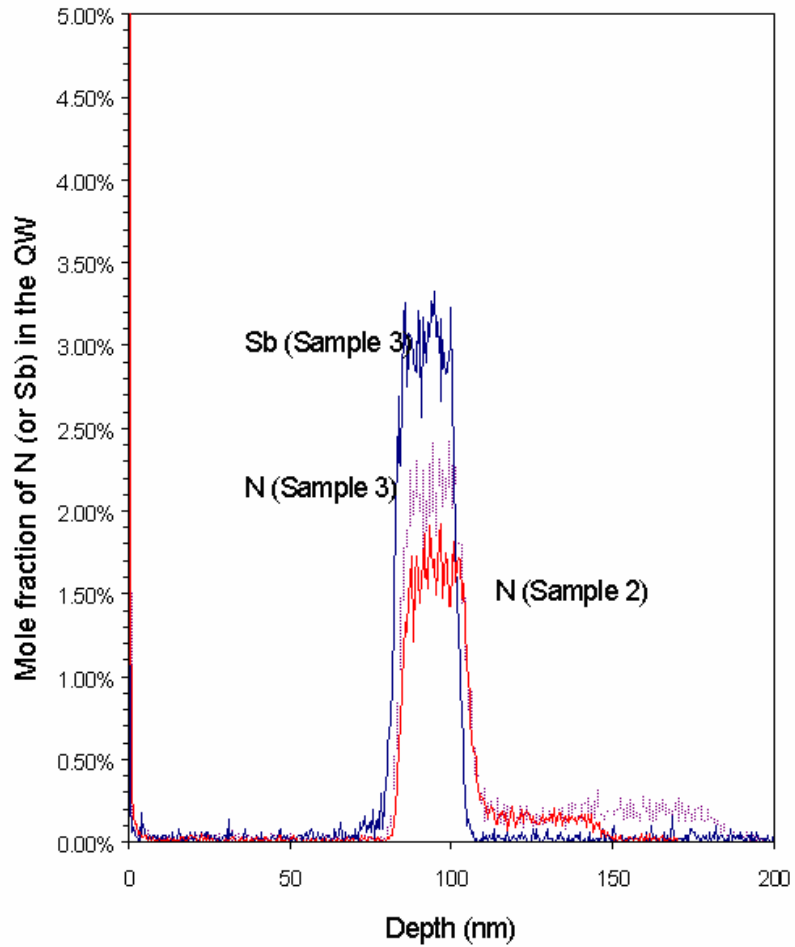


**Figure 2-11: SIMS analysis showed N% increased in the case of antimony atoms present during the QW growth.**

As shown in Fig. 2-11, with about 3% (mole fraction) Sb in the GaInNAsSb layer, N content increased from 1.6% (sample 2) to 2.1% (sample 3). Comparing the results of sample 1 and samples 2&3, the relationship between the N content and group III growth rate in Eq. (2-1) would still hold for the growth of GaInNAsSb on InP with one additional factor,  $C_{Sb}$ , in Eq. (2-2),

$$N\% = \frac{A_{InP} \cdot C_{Sb}}{gr_{Ga} + gr_{In}} \quad (2-2)$$

where the constant factor  $A_{InP}=0.8$  and the nitrogen incorporation enhancement factor with 3.0% Sb was  $C_{Sb}\sim 1.3$ .

It was known that the nitrogen incorporation was independent of indium composition during the MBE growth of GaInNAs layers on GaAs substrates with indium less than 30% [21]. However, in the MOVPE growth of GaInNAs on GaAs, it was found that the segregation of indium atoms on the surface changed the surface reconstruction and affected the nitrogen incorporation during the growth [27]. SIMS analysis of sample 1 in Fig. 2-9 showed that the indium composition was different in the QW layers of GaInNAs and GaInNAsSb from that in the lattice matched buffer and cladding layers. From the raw SIMS data of, the indium ion count decreased by a certain amount (3.5% in sample 1, 1.5% in sample 2 and 2.1% in sample 3) while no corresponding increase was observed for gallium atoms. Since the source temperatures of indium and gallium were precisely controlled during all the layer growths, there must be some inter-correlation effects of N and In atoms, either during the layer growth of QW layers or in the SIMS analysis. Such an effect should also be expected in the growth of GaInNAs(Sb) on GaAs substrate. But since the cladding layers are either GaAs or GaAsN without continuous indium references, the change of indium content was small and might have been just overlooked in the past. Moreover, it is unlikely that the ion counting of nitrogen atoms and indium atoms in SIMS are correlated. Therefore, one of the explanations would be that randomly incorporated nitrogen atoms in the unit cell of InGaAs statistically change the cell infrastructure (a mixed state of Zinc-Blende and Wurt-zite cell) and the effective composition of the unit cells.

Photoluminescence (PL) measurements are a sensitive method for the characterization of the optical quality of MBE grown materials. From the wavelength and full-width-half-maximum (FWHM) linewidth of the PL emission peaks, the types and density of defects incorporated in the active region could be estimated. The pumping light source of the PL setup was an Argon-ion green laser with operation output power of 100mW at the sample surface. A group of different detectors (Si, Ge, standard InGaAs and wavelength-extended InGaAs) covered a wide range of wavelength from 600nm to 2.6 $\mu$ m. The 0.5m (optical path) spectrometer in the setup had three exchangeable gratings

with central sensitive wavelengths at 600nm, 1 $\mu$ m and 1.6 $\mu$ m, respectively. There was also a liquid-helium cooled cryostat sample stage for low-temperature PL as low as 25K except for the room-temperature PL measurement capability.

From chapter 1, we know that defects are normally generated from the heteroepitaxial growth of lattice-mismatched strained layers. On the other hand, the low growth temperature of GaInNAsSb SQW layers and high flux ratio of group-V/III introduced a large amount of point defects. Different from most of the defects related to misfit dislocations and threading edge dislocations, point defects can be healed by post-growth rapid thermal annealing (RTA) [28]. Fig. 2-12 shows that the intensity of PL emission peaks of cladding layers (LM-InGaAs at  $\sim$ 1.7 $\mu$ m) and SQW layers (GaInNAs at  $\sim$ 1.95 $\mu$ m or GaInNAsSb at  $\sim$ 2.05 $\mu$ m) all increased with increasing annealing temperatures from 600 $^{\circ}$ C to 720 $^{\circ}$ C. The decrease of intensity for annealing at the temperatures higher than 720 $^{\circ}$ C was due to the inefficient cover protection against arsenic desorption from the samples. The partially relaxed GaInNAsSb layer of sample 1 (with nitrogen content of 3.5% and tensile strain of 0.9%, thickness of SQW 50nm) had a high concentration of non-radiative defects that quenched the photoluminescence. The low temperature used in the growth of GaInNAs(Sb) introduced extra defects in the layer even with the help of surfactant antimony atoms. Post-growth annealing reduced the non-radiative defects formed during the nitride layer growth and the optimized annealing conditions would be between 680 $^{\circ}$ C and 720 $^{\circ}$ C for 1 to 10mins with a maximum ramping rate of 200 $^{\circ}$ C/sec.

The blue shift of the PL emission peaks of annealed GaInNAs(Sb) samples grown at low temperature and annealed at high temperature, which have been both experimentally and theoretically explained by the nearest nitrogen neighbors changes in GaInNAs/GaAs pseudo-cell structures [29], were not clearly observed for the SQW structures grown on InP substrates. One of the possible reasons is that the additional antimony atoms in the QW layer grown on InP substrates reduces the strain instead of increasing the already highly compressive strain of GaInNAsSb QW layers grown on GaAs substrates, which reduces the driving force for changes in the nearest nitrogen neighbors during annealing. The influence of non-radiative defects on the intensities of

PL emission peaks were expected to be reduced for low temperature measurements (as shown in Fig. 2-13).

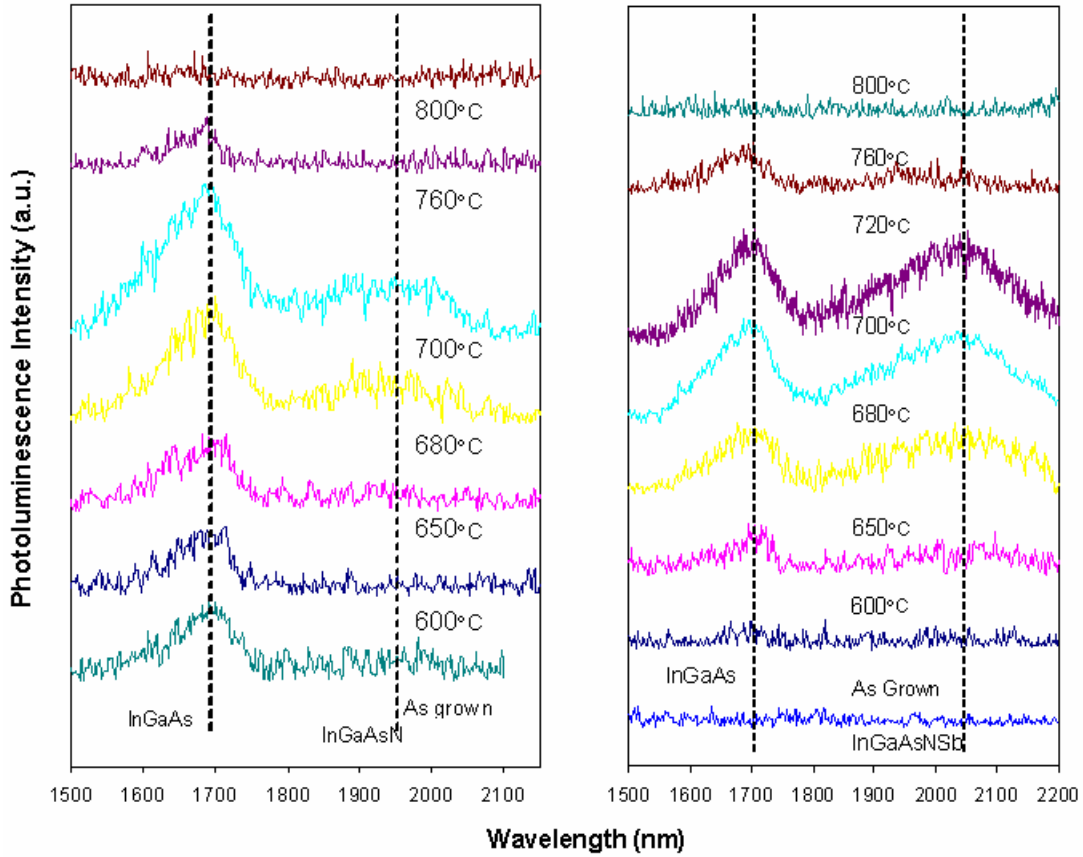


**Figure 2-12: RTPL of sample 2 (SQW with GaInNAs of N%=1.6%) and sample 3 (SQW with GaInNAsSb of N%=2.1% and Sb%=3.0%).**

In summary, InGaAs/GaInNAsSb/InGaAs SQW structures with good crystalline and optical qualities were successfully grown on InP substrates with RTPL emission beyond 2 $\mu$ m. Nitrogen content was inversely proportional to the growth rate of group III ingredients. Antimony atoms enhanced the nitrogen incorporation and acted as surfactant to improve the material qualities.

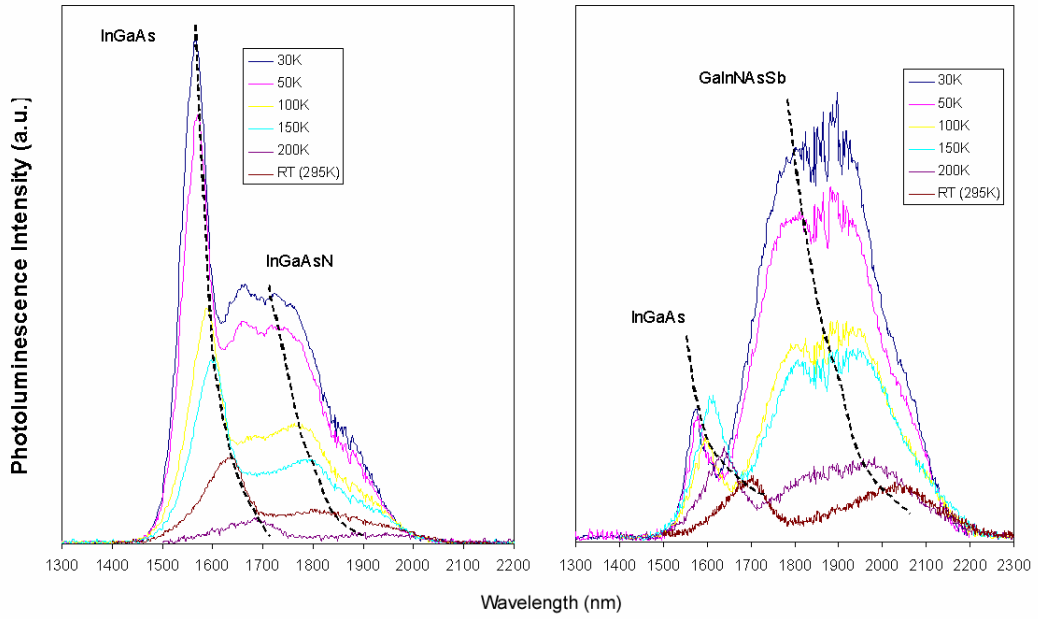


**Figure 2-13: LTPL measurements for SQW structures of samples 2 and 3 and both of the samples were annealed at 720°C for one minute, where the features around 1.9 $\mu$ m come from the water absorption in the air.**

## 2.2 Pseudomorphic growth of highly-strained InGaAs

In addition to the lattice-matched materials systems, highly strained materials systems can also be grown on InP substrates with high quality. As mentioned before, defects would be generated if the thickness of the lattice mismatched layers exceeded the critical thickness,  $h_c$ , (in Eq. (2-3)), called the Matthews' critical thickness, over which the strain would be compensated by misfit dislocations (MD) [30].

$$h_c \sim \frac{b(1-\nu \cos^2 \theta)}{4\pi(1+\nu)\epsilon \cos \lambda} \ln\left(\frac{ah_c}{b}\right) \quad (2-3)$$

where  $b = a/\sqrt{2}$  is the magnitude of the Burgers vector ( $a$  is the lattice constant of the film),  $\nu$  is the Poisson's ratio and for most of the semiconductors  $\nu=0.2(0.3)$ ,  $\theta$  is the angle between the MD line and Burgers vector,  $\epsilon = \frac{a_f - a_s}{a_s}$  is the misfit strain,  $\lambda$  is the

angle between the Burgers vector and a line that lies in the interface of film and substrate normal to the MD line and is related to the defect type,  $\alpha$  is the core cutoff parameter. For example, the growth of InGaAs layers on InP substrates has relevant parameters:  $\alpha \sim 4$ ,  $\cos \lambda = 0.5$ ,  $\nu = 0.2$ ,  $\theta = 60^\circ$ ,  $a_s = 5.8688 \text{ \AA}$ . The calculated theoretical critical thickness of InGaAs film on InP substrates is shown in Fig. 2-14.

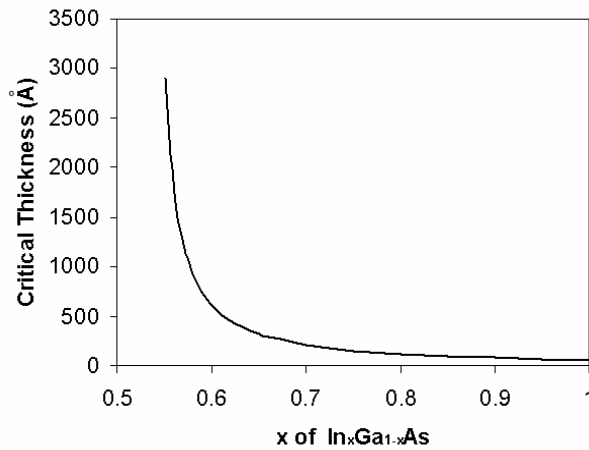


**Figure 2-14: InGaAs film critical thickness on InP substrate.**

The dependence of critical thickness on the film strain varied for different growth conditions [31]. It is possible to grow thin layers with effective thicknesses greater than the critical thickness limit (metastable, supercritical) by applying specific growth techniques. Compared to metamorphic growth of lattice relaxed material, pseudomorphic growth of highly strained layers had better misfit dislocation control and has proven to be more appropriate for specific device applications, like HEMT, for high speed electronic components [32].

### **2.2.1 Strain-balanced In<sub>x</sub>Ga<sub>1-x</sub>As/In<sub>y</sub>Ga<sub>1-y</sub>As superlattice**

Stain-balanced growth techniques have been extensively applied in the MBE growth of lattice-mismatched material systems [30, 33]. It can be applied to the growth of wavelength-extended InGaAs quantum structures on InP substrates (shown in Fig. 2-15). Material 1 and 2 have two different indium content, one larger than 53.2% and the other smaller than 53.2%, with compressive and tensile strain, respectively. When Eq. (2-4) is

satisfied, thick layers of material 1 and 2 can be coherently grown (no relaxation happens).

$$t_1 \cdot \frac{a_1 - a_s}{a_s} = t_2 \cdot \frac{a_2 - a_s}{a_s} \text{ and } t_1, t_2 < h_c \quad (2-4)$$

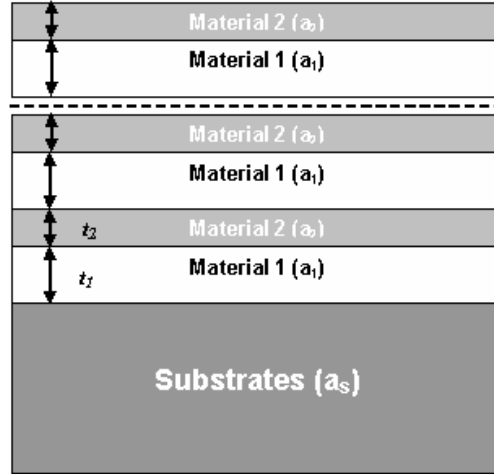


**Figure 2-15: Strain-balanced growth.**

Two gallium cells in the SSMBE system (I) gave an extra freedom for the growth of InGaAs layers with different composition. Ten periods of tensile-strained (In%=0.41) and compressive-strained (In%=0.67) InGaAs were successfully grown as superlattices on (100) InP substrates. Both layers had strain with a magnitude of  $|\varepsilon| = 0.8\%$  to the InP substrates, and the layer thicknesses was 20nm each in one period, smaller than the critical thickness calculated from the theoretical models above.

TEM pictures (shown in Fig. 2-16) showed smooth interfaces between the two material layers in the superlattice. The contrast comes from the composition of different indium content, layers with higher indium content being darker. The total thickness of  $\text{In}_{0.67}\text{Ga}_{0.33}\text{As}$  (or  $\text{In}_{0.41}\text{Ga}_{0.59}\text{As}$ ) was 200nm, much thicker than the calculated critical thickness. XRD rocking curve measurements ( $\omega/2\theta$  (004) scan) showed good structural quality (shown in Fig. 2-17 with very narrow width of satellite peaks compared to the simulation results).

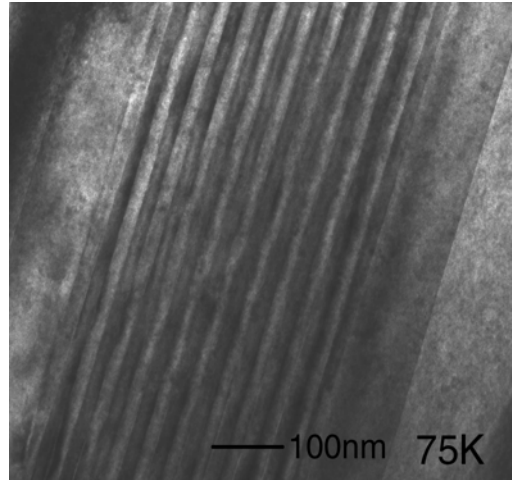


**Figure 2-16: Cross-section TEM (XTEM) picture of strain-balanced superlattice  $\text{In}_x\text{Ga}_{1-x}\text{As}/\text{In}_y\text{Ga}_{1-y}\text{As}$  ( $x=0.41$  and  $y=0.67$ ) grown on lattice-matched  $\text{InGaAs}/\text{InP}$ .**

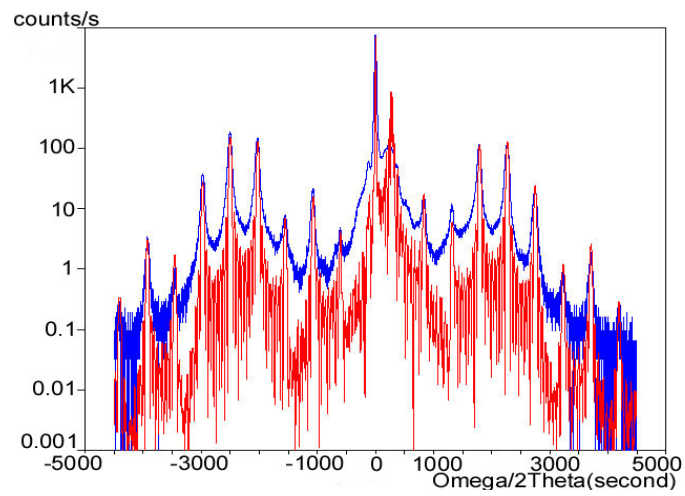


**Figure 2-17: XRD rocking curve of  $\text{In}_x\text{Ga}_{1-x}\text{As}/\text{In}_y\text{Ga}_{1-y}\text{As}$  superlattices: measurement curve with narrow satellite peak features (top) and simulation curve (bottom).**

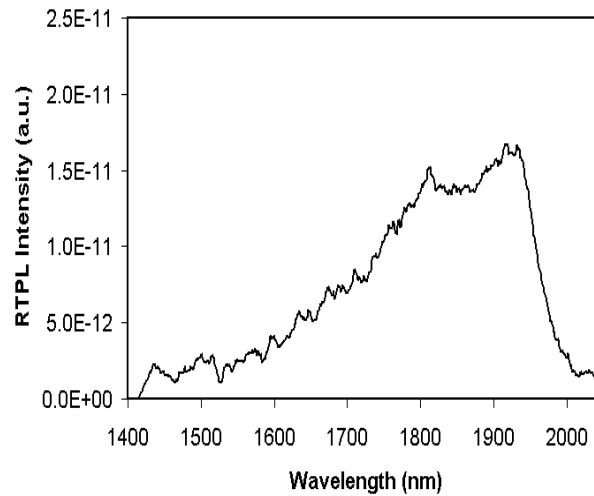


**Figure 2-18: RTPL of  $\text{In}_x\text{Ga}_{1-x}\text{As}/\text{In}_y\text{Ga}_{1-y}\text{As}$  ( $x=0.41$  and  $y=0.67$ ) superlattice.**

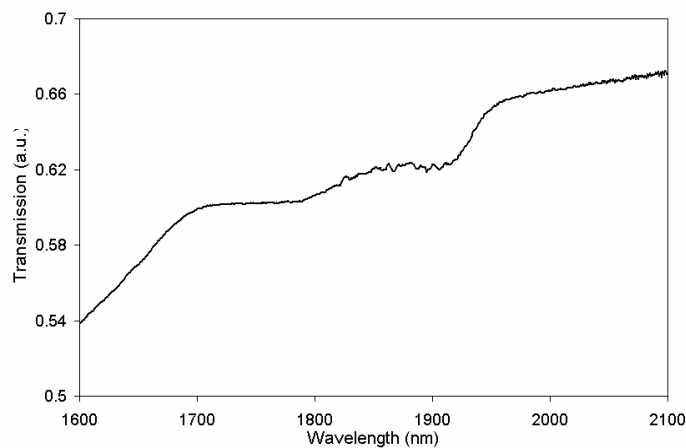


**Figure 2-19: Room-temperature optical absorption of the superlattice with absorption edge at around  $1.95\mu\text{m}$  ( $\text{In}_{0.67}\text{Ga}_{0.33}\text{As}$ ),  $1.7\mu\text{m}$  ( $\text{In}_{0.53}\text{Ga}_{0.47}\text{As}$ ), and features between  $1.8$ - $1.9\mu\text{m}$  due to the minibands absorption of the superlattice.**

Room-temperature photoluminescence (Fig. 2-18) and optical absorption (Fig. 2-19) were used to characterize the optical qualities of the strain-balanced superlattice. One of the RTPL emission peaks of strain-balanced  $\text{In}_{0.41}\text{Ga}_{0.59}\text{As}/\text{In}_{0.67}\text{Ga}_{0.33}\text{As}$  superlattices was at  $1.94\mu\text{m}$  with an effective FWHM width of  $120\text{nm}$  ( $40\text{meV}$ ). There was another peak around  $1810\text{nm}$  which can be explained by the mini-band theory for superlattices. The relatively strong PL intensity and narrow width of the peaks revealed the good

optical quality of the superlattice. The absorption coefficient of the superlattice structure was estimated to be  $2.4 \times 10^3 \text{ cm}^{-1}$  at  $1.9 \mu\text{m}$ .

### 2.2.2 Fractional monolayer superlattice $\text{In}_{0.53}\text{Ga}_{0.47}\text{As}/\text{InAs}$

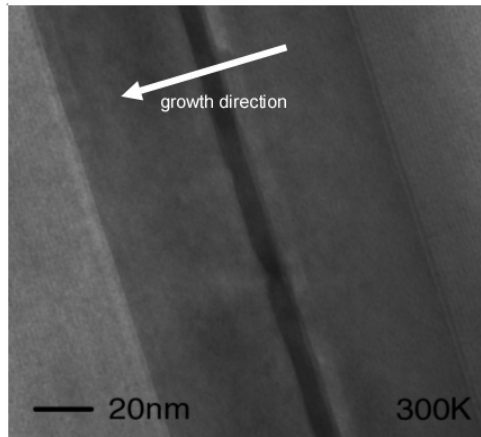


**Figure 2-20: XTEM of FMS SQW with LM-InGaAs cladding layers.**

Different from the strain-balanced superlattice growth, a fractional monolayer super-lattice (FMS) of  $\text{In}_{0.53}\text{Ga}_{0.47}\text{As}/\text{InAs}$  (1:3 in layer thickness ratio) can be grown as a quantum well layer with standard InGaAs cladding layers. The total QW region is thicker than the critical thickness (supercritical), but remains strained. Compared to GaAs/InAs superlattices [34], the strain between adjacent layers in LM-InGaAs/InAs superlattices is smaller and thus the growth can be controlled more precisely. Single quantum well and multiple quantum well structures were grown and characterized. RHEED patterns were used to monitor the coherent growth of the superlattices. Before the growth of the quantum well, streaky RHEED pattern features were recognized. When the FMS growth started from the InAs layer, the streaky RHEED pattern became weak and blurry, but still kept the streaky features. During the growth of the following LM-InGaAs layers, the RHEED pattern became bright and sharply streaky again similar to the RHEED pattern before the FMS growth. The quantum well thickness was controlled to assure coherent growth of all layers. It was known that low growth temperature was preferred for highly strained metastable film layers, so the substrate temperature was cooled  $20^\circ\text{C}$  lower for the growth of the FMS quantum well compared to that of the LM-InGaAs cladding layers. Ten periods of superlattice were grown with a thickness of each period  $0.68\text{nm}$ , of

which the LM-InGaAs layer is 0.17nm (half monolayer) and the InAs layer is 0.51nm (shown in Fig. 2-20).

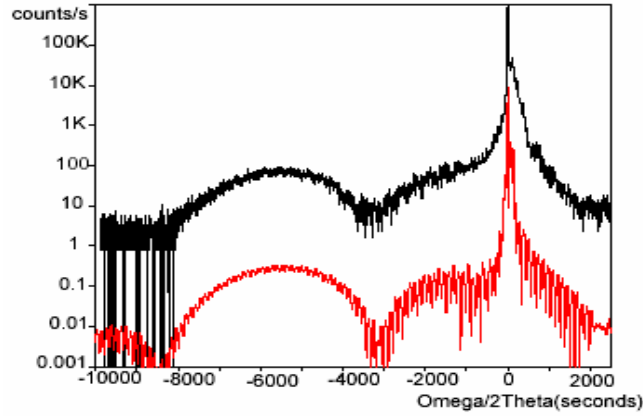


Figure 2-21: XRD rocking curve of FMS-SQW with effective indium content 88%.

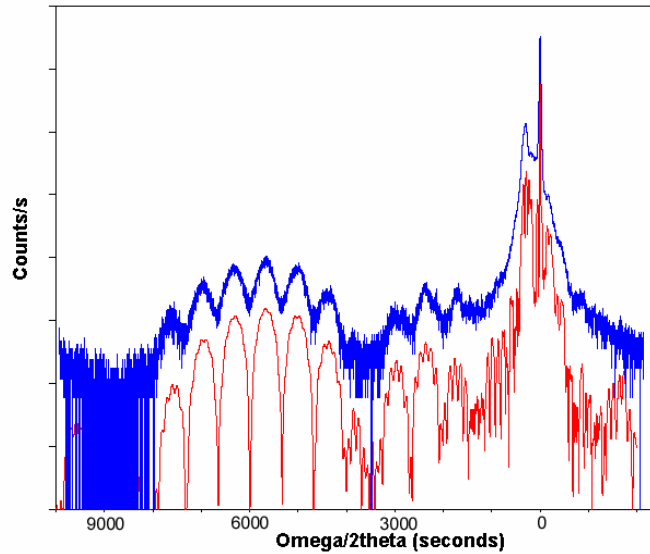
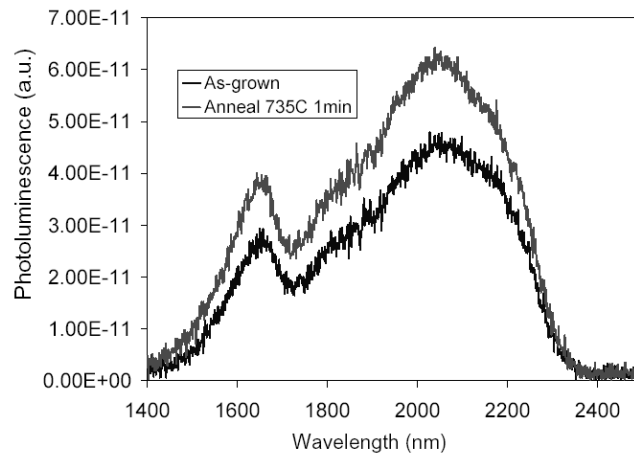


Figure 2-22: XRD rocking curve of 3 FMS-MQWs, measurement curve (blue) and effective 3-MQWs simulation curve (red) match well.

XRD rocking curve measurements (Fig. 2-21 and 2-22) verified that the effective indium content in the FMS-QW layer was 88% ( $\text{In}_{0.532}\text{Ga}_{0.468}\text{As} : \text{InAs} = 1:3$ ). The effective bandgap energy can be calculated using Eq. (1-7) for strained  $\text{In}_{0.532+x}\text{Ga}_{0.468-x}\text{As}$  grown on (001) InP substrates,  $E_g(x) = 0.75 - 0.63x + 0.45x^2 = 0.585\text{eV}$  (correspond to

the wavelength of 2.12 $\mu$ m). Single and multiple quantum wells were grown using the FMS growth technique with good structural qualities. Theoretically atomic level ordering in III-V alloys could reduce the effective bandgap energy [35]. Different from the spontaneous atomic ordering in ternary material alloys (for example, (InAs)<sub>x</sub>(GaAs)<sub>1-x</sub>), FMS introduced intentional atomic ordering in the SQW layer. However, the bandgap energy narrowing effect is always very small and hardly observed by normal characterization methods. RTPL measurements provide an estimation of the optical qualities of the grown quantum well structures and the emission peaks in the PL spectrum can be used to determine the bound energy states of electrons in the quantum well. The TEM picture of the FMS-SQW in Fig. 2-20 shows clear waviness and non-uniform thickness of the QW layer. The roughness at the top interface between the QW and cladding layer reflects the effects of indium atom segregation. The thickness fluctuation was on the order of 1nm (3-4 monolayers), small for bulk growth or thick layer growth but showing clearly observable effects in photoluminescence.



**Figure 2-23: RTPL of FMS-SQW In<sub>0.53</sub>Ga<sub>0.47</sub>As/InAs 1:3 with QW layer 6.8nm.**

Compared to the RTPL of the strain-balanced superlattice (Fig. 2-18), the FMS-SQW sample showed higher carrier confinement and greater peak broadening (FWHM) from the PL measurements. RTPL had an emission peak at 2.05 $\mu$ m and spread from 1750nm to 2400nm (shown in Fig. 2-22). The thickness fluctuation of the quantum well partly contributed significantly to the peak broadening. On the other hand, low-temperature grown FMS-QW contained a significant amount of defects that could only be

partly healed by post-growth annealing at 735°C for only one minute. Based on the observation of RTPL, we assumed that at least some of the defects introduced by low-temperature grown, highly strained FMS-QW were point defects and optimized growth conditions could lead to better material quality.

### 2.2.3 Conclusion

In summary, wavelength-extended InGaAs with high (or effectively high) indium content were pseudomorphically grown on LM-InGaAs/InP substrates using strain-balanced superlattices and fractional monolayer superlattices. Photoluminescence and optical absorption measurements demonstrated the possibility of using such material systems to fabricate optoelectronic devices active at a wavelength region beyond 1.7 $\mu\text{m}$  [36, 37].

## 2.3 Metamorphic growth of relaxed InGaAs

In the previous two sections, lattice matched and strained InGaAs based materials and quantum structures demonstrated NIR emission and absorption in the wavelength range beyond that of the standard InGaAs at 1.7 $\mu\text{m}$ . Because of the strain influence on the splitting of heavy-hole and light-hole bands in the valence band (Eq. 1-7 of Chapter 1), the bandgap energy of pseudomorphic strained InGaAs would not be smaller than 0.554eV (corresponding wavelength of 2.24 $\mu\text{m}$ ). For the growth of GaInNAsSb on InP (or LM-InGaAs), a mole fraction of nitrogen atoms as high as 3.5% would be required to reach a bandgap energy of 0.5eV (wavelength of 2.5 $\mu\text{m}$ ). Even with the surfactant effect of antimony atoms present, compensating the strain and smoothing the growth front surface, such high nitrogen content would increase the degree of difficulty in MBE growth due to the problem of phase segregation. In order to reach NIR region as far as 2.5 $\mu\text{m}$ , relaxed InGaAs with indium content  $\leq 80\%$  must be considered for the active regions. The lattice mismatch between the device active regions of  $\text{In}_{x>0.8}\text{GaAs}$  and substrates is more than 1.84% and 5.73% for the layers grown on InP and GaAs substrates, respectively. During the epi-layer growth, when the thickness of mismatched layers is thicker than the critical thickness defined by Eq. (2-3), dislocations will typically

form to accommodate the relaxation of strain between the substrate and the grown film layers. A high density of various defects (as shown in Fig. 1-8) would generate, accumulate and propagate into the active regions if no special material growth techniques were accomplished for the metamorphic growth of relaxed InGaAs [38, 39]. Theoretical models based on energy equilibrium provide guidance on various mechanisms for reducing the misfit and threading dislocations and monitoring defect propagation into the highly mismatched layers [40-42].

### **2.3.1 Threading Dislocation reduction and defect control**

Generally the density of TD is inversely proportional to the thickness of buffer layers, which means very thick buffer layers have to be grown in order to achieve high quality device layers with TD densities at the level of  $10^6\text{cm}^{-2}$ . On the other hand, thermal design criteria for high-power devices and integration of optical systems on chip make a relatively thin buffer layer highly desirable to isolate the active device layers from incorporating misfit dislocations and other defects [43]. In addition to low densities of TD in the layers, smooth surface morphology of the growth front is also very important in reducing interface scattering effects for high speed and efficient devices, such as HEMT [44]. Several theoretical models have been proposed to reduce the TD densities in mismatched layers grown on TD-free substrates. TD reduction mechanisms include: the annihilation or fusion of TDs and arrest of TD by other dislocations, the blocking of TD by MD, and the annihilation of TD by interacting with another TD [40-42]. As shown in Fig. 2-24, the gliding motion of threading dislocations is influenced by the thickness of mismatched layers and the interaction of TDs, which is represented by the annihilation radius  $r_A$ .

Different schemes of buffer layers have been investigated for the growth of highly mismatched films on various substrates, including single-composition buffer layers, linear graded buffer layers, superlattice layers and step-graded buffer layers [45-47]. Step-graded buffers have been theoretically and experimentally identified as the best scheme. As for the growth of wavelength-extended InGaAs on InP substrates, various buffer materials including InAsP, InGaAs, InAlAs, and InGaAlAs, which have shown

different level of performance as metamorphic growth buffers [45-48]. It was noticed that under certain growth conditions, anion-based buffer layers (for example,  $\text{InAs}_x\text{P}_{1-x}$ ) demonstrated better quality than cation-based buffer layers (for example,  $\text{In}_x\text{Al}_{1-x}\text{As}$ ) partly because of the difference in the bond strengths between In-As (1.41eV) and Al-As (1.98eV) [48]. However, the growth of InAsP by MBE involves the use of phosphorous and introduces extra difficulty in composition control (non-unity sticking coefficient for As and P). On the other hand, InAlAs buffer layers have higher bandgap energy than InAsP buffer layers and so play an important role in reducing leakage current and enhancing the device performance [43]. It would thus be useful to find the optimized growth conditions for the growth of highly mismatched InGaAs device layers on InP or GaAs substrates with a metamorphic InAlAs buffer.

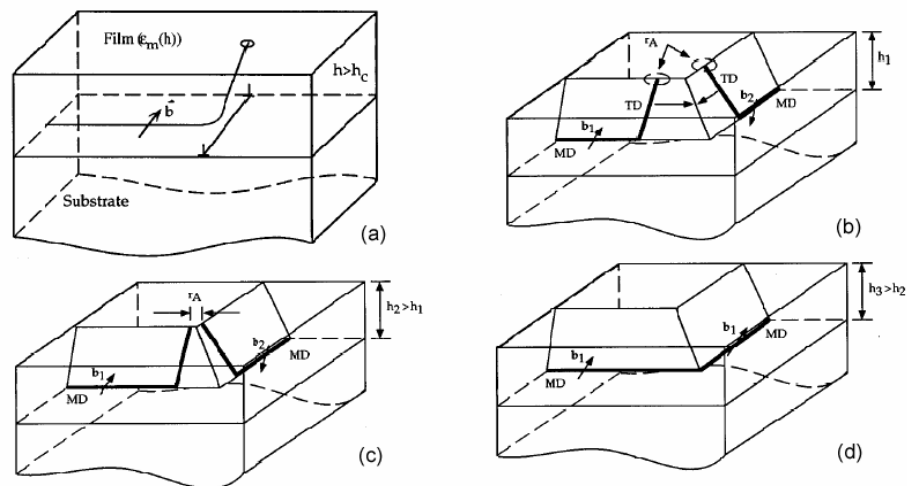


**Figure 2-24: TD motion corresponding to the thickness of strained layers: (a) blocking by a MD, (b) TDs out of the interaction range  $r_A$  (annihilation radius approximately 50-100nm for most III-V semiconductors), (c) TDs within the annihilation radius, (d) annihilation of two TDs [41].**

### 2.3.2 Sample growth and in-situ monitoring

All the samples were grown in the same GEN-II SSMBE system-I equipped with effusion cells for indium, gallium and aluminum, and an arsenic needle-valve cracker cell. In-situ reflective high-energy electron diffraction (RHEED) was used to monitor the substrate oxide blowoff and the growth process [49]. Two of the most important growth parameters, substrate temperature and growth rate, were pre-calibrated by at least two

different but consistent methods. Similar to the processes mentioned previously, the substrate temperature was calibrated to the thermal couple (TC) temperature using a combination of silicon-aluminum eutectic point, pyrometer, and the sublimation temperatures of GaAs (580°C) and InP (510°C). The growth rates were calibrated by ion-gauge measured beam-equivalent pressure, optical reflectivity spectroscopy and ex-situ step-profiling after selective wet-etching mesa-definition. The thick  $\text{In}_x\text{Ga}_{1-x}\text{As}$  ( $x > 0.8$ ) device layers grown on the  $\text{In}_y\text{Al}_{1-y}\text{As}$  metamorphic step-graded buffers have a lattice constant close to that of the buffer layers. For the growth of InGaAs on InP substrates,  $y$  changed from 0.52 to 0.82, while for the growth on GaAs,  $y$  changed from 0 to 0.8. The grading step scheme was chosen to insure 2-D growth mode all through the growth.

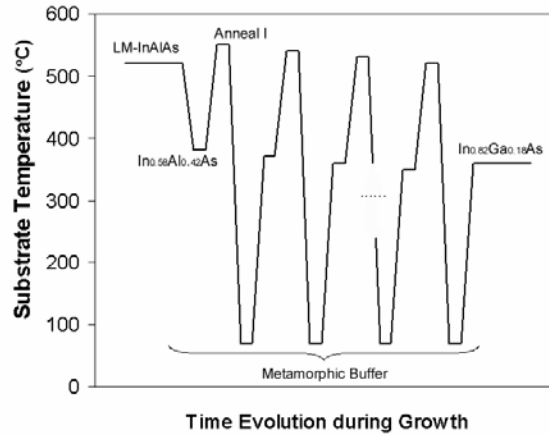


**Figure 2-25: Substrate temperature change over the time evolution during the growth of LM-InAlAs buffer, metamorphic InAlAs graded-buffers and thick InGaAs device layers.**

The surface of epi-ready Sn-doped n-type (or Fe-doped semi-insulating) InP substrates were prepared by a two-step thermal cleaning (refer to chapter 1 and section 2.1 in this chapter) and the substrate ramping rate was 20°C/min with an arsenic over-pressure of  $2.0 \times 10^{-6}$  Torr during the entire growth. After clear (2×4) surface reconstruction RHEED patterns were observed, the substrate was ramped down to TC520°C for lattice-matched  $\text{In}_{0.523}\text{Al}_{0.477}\text{As}$  layer growth. The first InAlAs layer was 200nm thick and acted as a growth buffer. The composition control for lattice-match condition was critical to achieve a smooth growth front surface. The surface cleaning of

GaAs substrates was very similar with the growth of GaAs and AlAs layers as growth buffers to eliminate the influence of defects and residual contamination of the substrates.

After the growth of a lattice-matched layer (LM-InAlAs on InP, or AlAs/GaAs on GaAs), the substrate was cooled down to 380°C to start the growth of the metamorphic buffer layers (shown in Fig. 2-25 with the temperature evolution only for the growth on InP substrates, while it was very similar for the growth on GaAs substrates). For growth on InP substrates, the buffer layer consisted of five steps with each step 250nm thick and a 6% indium content increase from bottom to top (shown in Fig. 2-26). For growth on GaAs substrates, the buffer layer consisted of eight steps with each step 250nm thick and 10% indium content increase. The composition change of the neighboring InAlAs layers was realized by changing the temperature of the aluminum cell during the cyclic annealing of the graded layers.

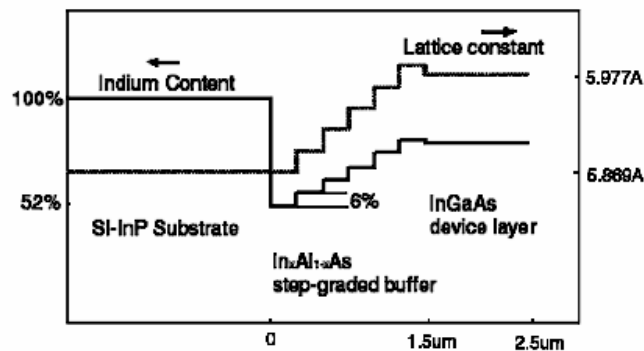


**Figure 2-26: Sample structure with InGaAs device layer and the metamorphic linearly step-graded buffer layers.**

The in-situ thermal annealing and the following cool-down process of each step in the graded layer were essential to achieve high-quality smooth interfaces. Growth temperature and annealing processes were critical for the metamorphic growth of the step-graded buffer layers. The substrate temperature for the growth of each step layer decreased from TC380°C to TC340°C, and the in-situ annealing temperature decreased from TC540°C to TC500°C with an annealing time of 20 minutes for each step. The thick (1µm) InGaAs device layers had a slightly smaller lattice constant compared to the very

top step layer of the buffer in order to compensate for the residual strain in the buffer layers. Another capping layer of InAlAs was grown on top of the InGaAs device layer.

RHEED was used during the growth of the step-graded layers to monitor the annealing process and the growth of the thick InGaAs layer. The RHEED pattern became blurry, although still identifiable as streaky, during the low-temperature growth of each step layer. During the in-situ annealing process, the pattern became brighter and clearer with (2×4) surface reconstruction patterns and restoring the streaky features. Since the substrate was rotating during the growth, streaky patterns were clearer on the two perpendicular positions which were identified as <110> directions. All samples grown with metamorphic buffer layers using the cyclic in-situ annealing method showed mirror-like surfaces. Under illumination of grazing incident intense light, line structure features could be easily recognized along the  $[0\bar{1}1]$  direction.

### 2.3.3 Surface morphology and evolution

The surface morphology of samples with metamorphic step-graded buffer layers was characterized by AFM with both 0° scans (along  $[011]$  direction), 90° scans (along  $[0\bar{1}1]$  direction) and 45° scans. By combining all three scans, we could identify the line features along both  $[011]$  and  $[0\bar{1}1]$  directions, which are the so-called “cross-hatch” lines typical of lattice mismatch heteroepitaxy.

As shown in Figure 2-27 (d), in a relatively large range of scan across the surface area of 50×50μm, the effective RMS roughness was 2.968nm, which is a factor of two to three times better than previously reported results [45-48, 50]. If we consider a local area as small as 5×5μm (the typical area a transistor might occupy), the best RMS roughness was as low as 1.521nm, compared with that reported by Hudait for the growth of an 800nm-InGaAs device layer with continuous four-step graded buffer layers for a total thickness of 2.7μm, the RMS surface roughness was 7.3nm for InAlAs buffer layers and 2.2nm for InAsP buffer layers [48].

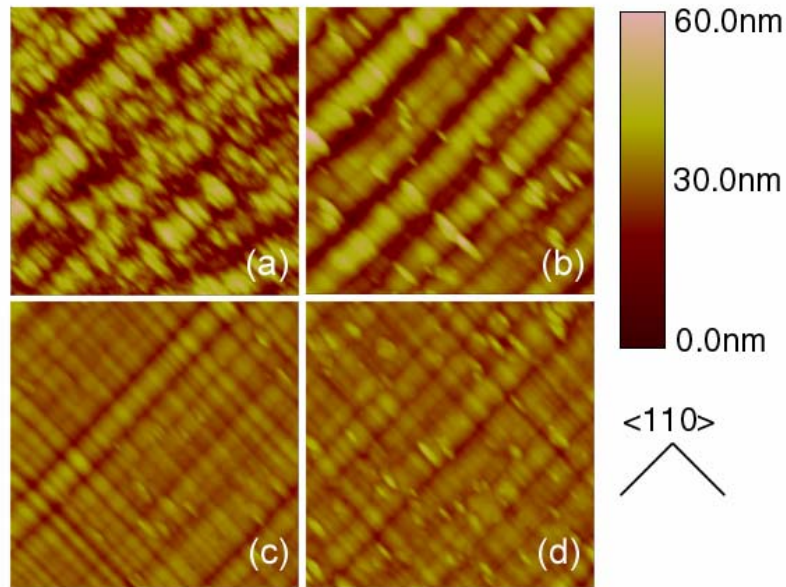


**Figure 2-27: AFM for InGaAs grown on InP substrates with metamorphic InAlAs buffer at different substrate temperature:  $T_{(a)} > T_{(b)} > T_{(c), (d)}$ .**

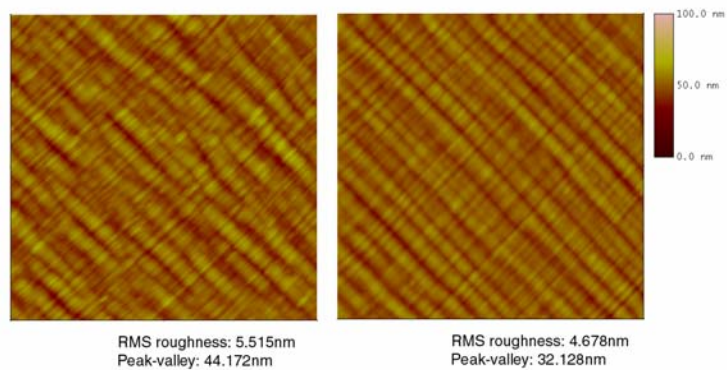


**Figure 2-28: AFM for InGaAs samples grown on GaAs substrates, left miscut (001) substrate with 4° toward [110]A, right (001) substrate.**

The RMS surface roughnesses of samples here with InAlAs buffer layers using the cyclic in-situ annealing method were comparable to those in [48] with InAsP buffers. However, the surface morphology was very dependent on substrate temperature, growth rate, annealing temperature and substrate type for the growth of step-graded buffers (as shown in Fig. 2-27 and 2-28). Low substrate temperature and high growth rate were essential to achieve smooth surfaces by reducing indium droplet formation and inhibiting

the diffusion of surface atoms. On the other hand, the surface morphology and relaxation were affected by substrate orientation and the growth of buffer and device layers.

#### 2.3.4 Strain relaxation and characterization

High-resolution X-ray diffraction (HRXRD) is a sensitive measurement for characterizing the structural qualities of epitaxial films grown on substrates. HRXRD rocking curve (RC) measurements have been used in the previous investigations of lattice-matched and pseudomorphic structures on InP substrates, characterizing the material composition and structural qualities [51, 52]. For films with unknown composition, the use of XRD is limited in estimating the relaxation of films since XRD is dependent on both. Other characterization methods, like SIMS, combined with the rocking curve or the RSM measurements of HRXRD, can accurately estimate the composition and relaxation of device layers, as well as each step of the metamorphic buffer layers. As shown in Fig. 2-29, the XRD rocking curve of  $\text{In}_{0.835}\text{Ga}_{0.165}\text{As}$  ( $0.94\mu\text{m}$ ) grown on  $\text{In}_x\text{Al}_{1-x}\text{As}$  metamorphic step-graded buffer layers (8-steps with a total thickness of around  $2\mu\text{m}$ ) on GaAs substrates shows clear grading steps and good structural qualities of both device layer and buffer layers. Using the composition analysis results from SIMS (Fig. 2-30), the relaxation of each step layer and the device layer can be estimated. However, due to the interference effects and calibration difficulty in SIMS, the absolute calibration on composition analysis can only be within a range of 5%. Based on the results of HRXRD and SIMS, the metamorphic buffer layers were fully relaxed (100% relaxation) and the device layer was closely lattice matched to the top buffer layer.

The FWHM width of the peak of a thick  $\text{In}_{0.835}\text{Ga}_{0.165}\text{As}$  device layer grown on a GaAs substrate (overlapping with the top step-graded buffer layer) in the  $\omega$ - $2\theta$  scan was 123arcsec and that in the  $\omega$  scan was 1230arcsec. For the growth of  $\text{In}_{x>0.8}\text{GaAs}$  on InP substrates with metamorphic InAlAs buffer layers, the FWHM width of device layer in the  $\omega$ - $2\theta$  scan was only 63arcsec and that in the  $\omega$  scan was only 540arcsec (not shown here). Generally speaking, the peak width broadening of the XRD rocking curves comes from scattering by defects, local disorder structure or phase separation of grown films [53]. As mentioned before, the indium content changes in the samples grown on GaAs

and InP substrates were 40%/μm and 24%/μm, respectively. It was not surprising that highly mismatched InGaAs device layers grown on InP substrates had better material qualities than those grown on GaAs substrates.

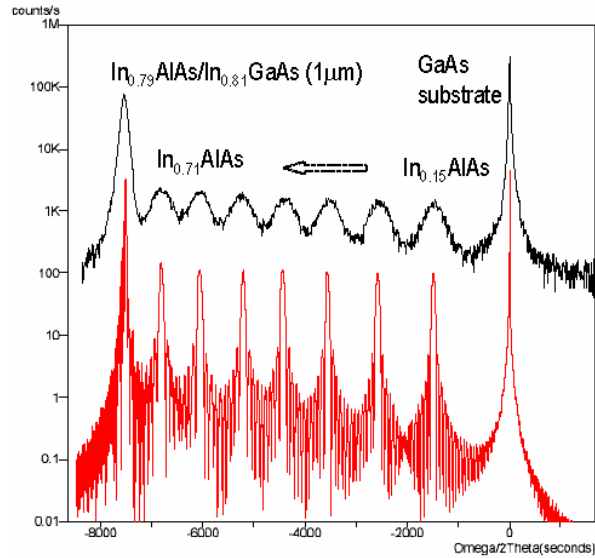


Figure 2-29: XRD rocking curve ( $\omega-2\theta$ ) of sample grown on GaAs substrate.

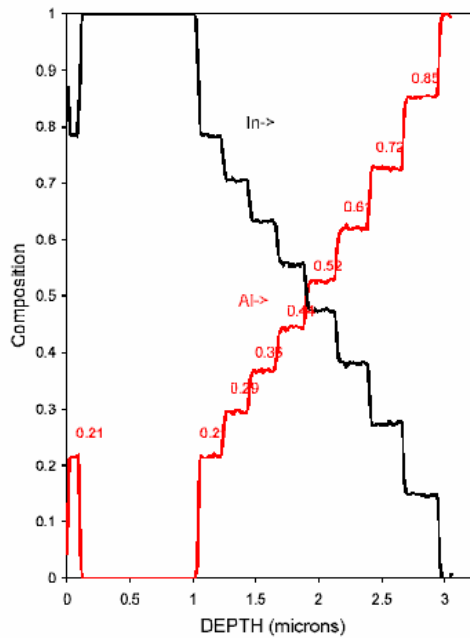


Figure 2-30: SIMS depth profiling of the same sample as above grown on GaAs substrate.

In addition to the HRXRD rocking curves, reciprocal space map (RSM) is capable of unveiling the relative lattice tilt and estimating the residual strain in the layers versus the substrate [54, 55]. Two types of RSM scan, symmetric (004) scans and asymmetric (224) scans, are generally used in III-V material characterization. The (004) scans are sensitive for estimating the lattice tilt of layers to the substrate, and (224) scans are sensitive for characterizing the relaxation and residual strain of the layers themselves relative to the substrate. Fig. 2-31 shows the RSM scheme of substrates ( $a_{sub}$ ) and film layers grown strained, partly relaxed and fully relaxed with and without a lattice tilt of  $\alpha$ , which can be calculated by Eq. (2-5) using the peak position displacement ( $\Delta q_y$  and  $\Delta q_z$ ).

$$\tan \alpha = \frac{\Delta q_y^{004}}{\frac{4}{a_{sub}} - |\Delta q_z^{004}|} \quad (2-5)$$

Lattice mismatch between the film and the substrate can be estimated for perpendicular misfit to (001) substrate ( $\perp$ ) and in-plane misfit ( $\langle 110 \rangle$ ) in Eq. (2-6),

$$\left( \frac{\Delta a}{a} \right)_{\perp} = - \frac{\Delta q_z^{004}}{\frac{4}{a_{sub}} + \Delta q_z^{004}}$$

$$\left( \frac{\Delta a}{a} \right)_{\langle 110 \rangle} = - \frac{\Delta q_y^{224}}{\frac{2\sqrt{2}}{a_{sub}} + \Delta q_y^{224}} \quad (2-6)$$

and the lattice mismatch misfit can be calculated by Eq. (2-7),

$$\frac{a_f - a_s}{a_s} = \left( \frac{\Delta a}{a} \right) = \frac{1-\nu}{1+\nu} \left( \frac{\Delta a}{a} \right)_{\perp} + \frac{\nu}{1+\nu} \left[ \left( \frac{\Delta a}{a} \right)_{\langle 110 \rangle} + \left( \frac{\Delta a}{a} \right)_{\langle \bar{1}\bar{1}0 \rangle} \right] \quad (2-7)$$

where  $\nu$  is the Poisson coefficient.

The relaxation rate of the layers grown on the substrate can be estimated by Eq. (2-8), taking into account the residual strain,  $\varepsilon_r$ , of the grown-film with an expected strain,  $\varepsilon$ .

$$R = \frac{\varepsilon - \varepsilon_r}{\varepsilon} = \frac{\frac{a_f - a_s}{a_s} - \frac{a_f - a_{XRD}}{a_{XRD}}}{\frac{a_f - a_s}{a_s}} \quad (2-8)$$

where  $a_f$  and  $a_s$  are the lattice constants of the unstrained film and substrate, respectively,  $a_{XRD}$  is the lattice constant of film measured from the rocking curve.

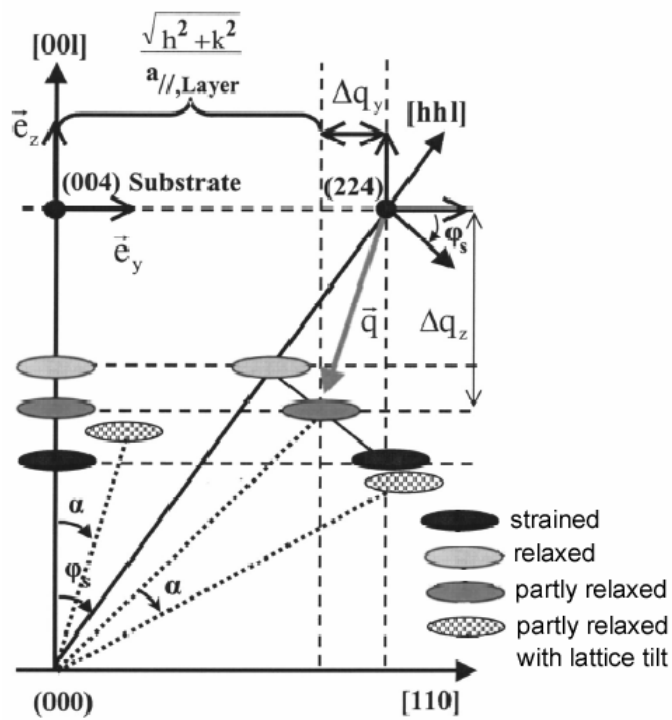
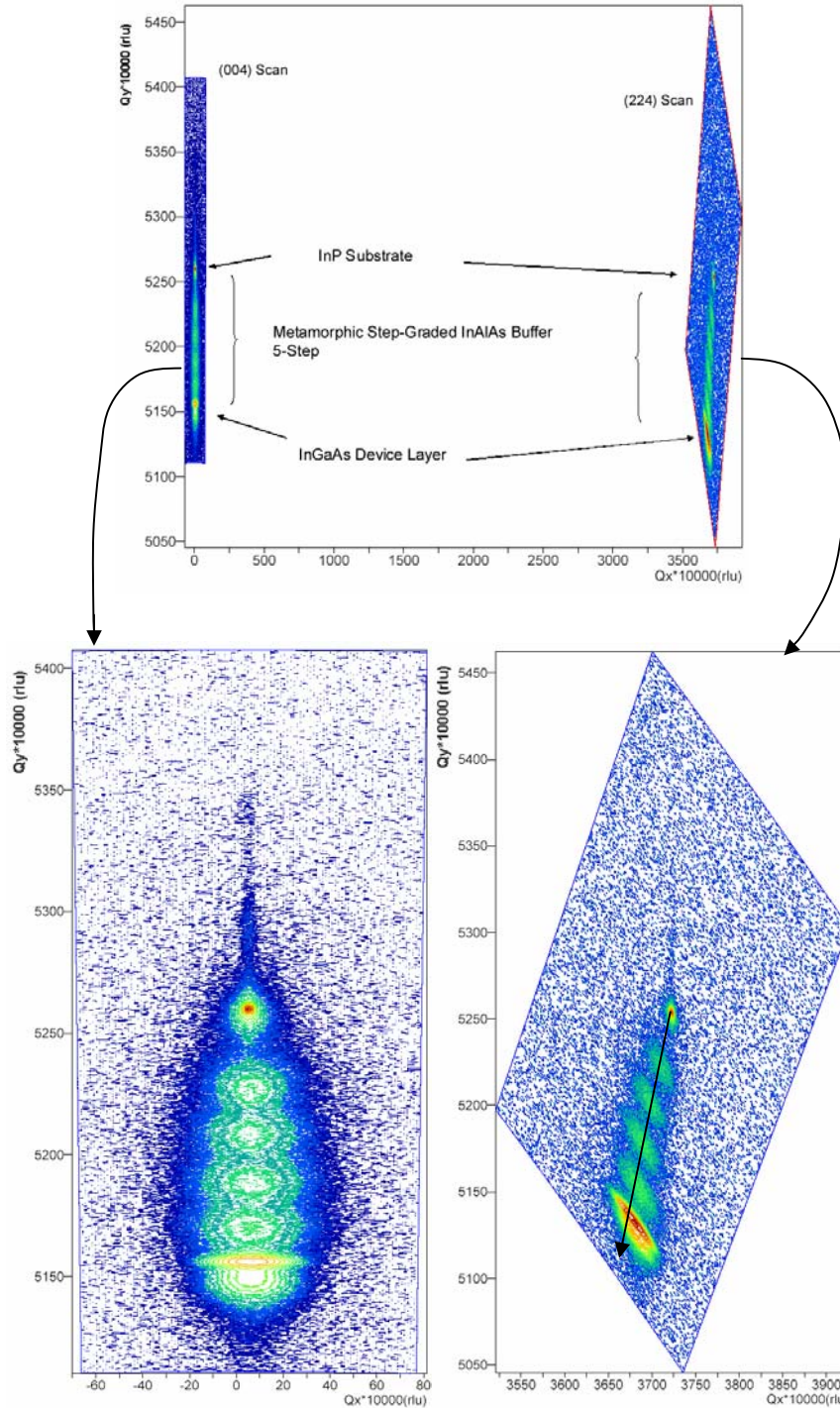


Figure 2-31: RSM diagram for (004) symmetric and (224) asymmetric scans, shown are substrate and films peaks under different scenario, strained, partly relaxed, fully relaxed and partly relaxed with lattice tilt [55].



**Figure 2-32: RSM of InGaAs(device layer)/InAlAs metamorphic buffers grown on InP substrates for both (004) and (224) scans.**

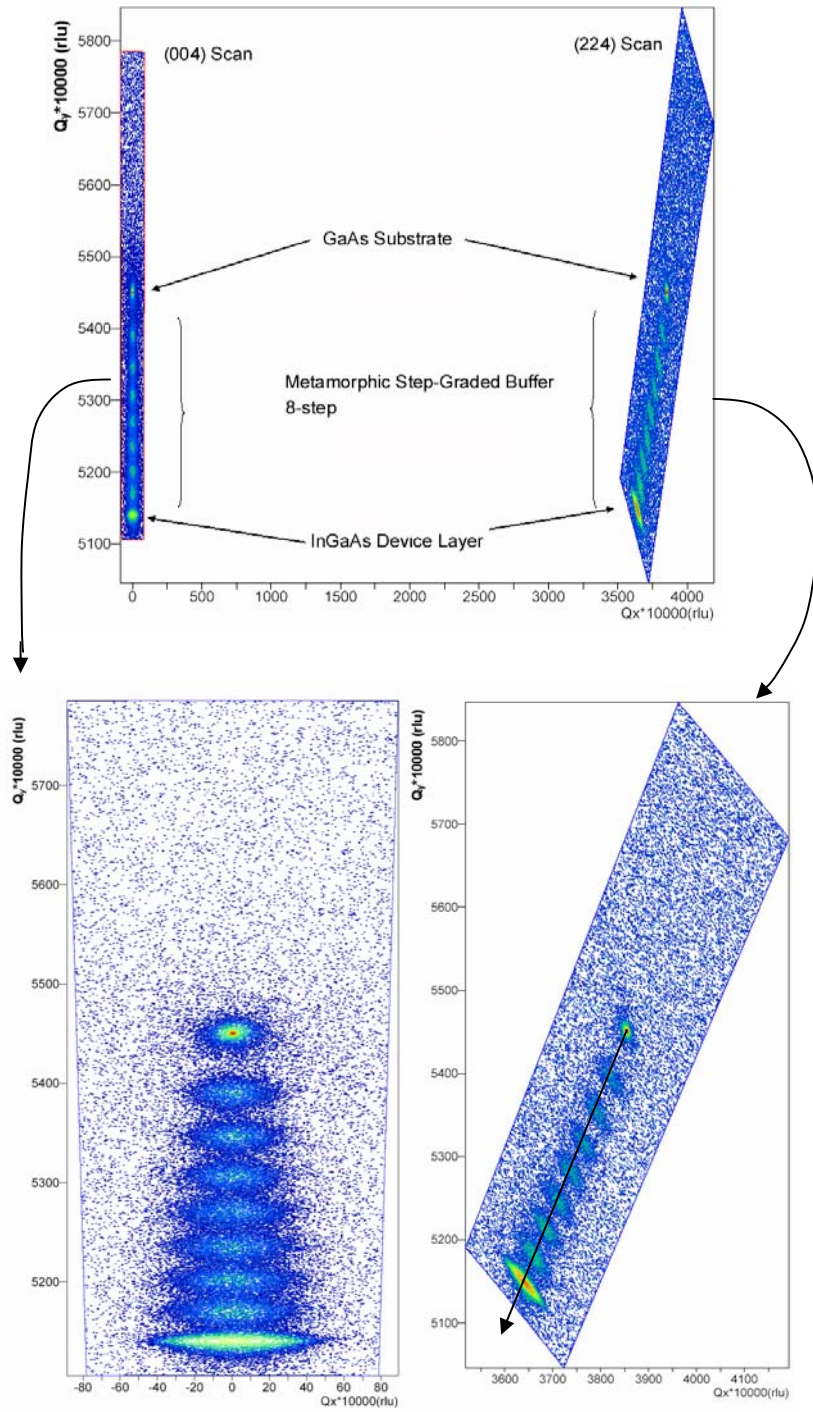
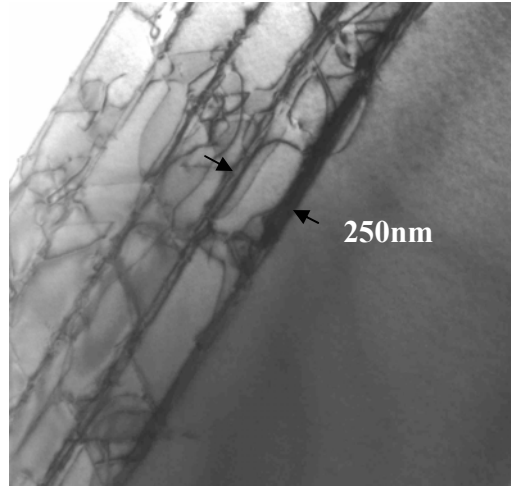


Figure 2-33: RSM of InGaAs (device layer)/InAlAs metamorphic buffers grown on GaAs substrates for both (004) and (224) scans.

Fig. 2-32 shows the RSM (004) and (224) scans for InGaAs device layers with five-step graded metamorphic buffer layers. The reciprocal lattice units (rlu) in the RSM scan normally denote  $\lambda/2d$  or  $1/d$  ( $\lambda$  is the X-Ray wavelength and  $d$  is the spacing between diffracting crystal planes,  $d = a / \sqrt{h^2 + k^2 + l^2}$ ) depending on the set options. Here a simple method of representation is chosen as  $1/P$ . The peak positions of the InP substrate and InGaAs device layer were  $(4.8327, 5259.8868) \times 10^{-4}$  rlu and  $(7.3181, 5156.2665) \times 10^{-4}$  rlu on the (004) scans,  $(3722.2961, 5253.9571) \times 10^{-4}$  rlu and  $(3681.0708, 5132.3543) \times 10^{-4}$  rlu on the (224) scans, respectively. The lattice tilt calculated by Eq. (2-5) was  $0.021^\circ$  (76 arcsec). The perpendicular misfit  $(\Delta a/a)_\perp = 1.54\%$ , and the in-plane misfit  $(\Delta a/a)_{\langle 110 \rangle} = 0.86\%$ , so the lattice mismatch was 1.65% (the [100] Poisson ratio for  $\text{In}_x\text{Ga}_{1-x}\text{As}$  is  $0.31+0.04x$ ) while the expected lattice misfit for  $\text{In}_{0.8}\text{Ga}_{0.2}\text{As}$  on InP was 1.85%. The relaxation rate of the InGaAs device layer was estimated to be 90%, and those of the five-step graded InAlAs buffer layers were estimated to be 100%, 100%, 100%, 93%, and 82%, respectively. Similarly, from the RSM (004) and (224) scans of the sample grown on a GaAs substrate (shown in Fig. 2-33), the eight-step graded metamorphic buffer layers as well as the device layer (overlapping with the last top buffer layer) were clearly identified (same sample as that in Fig. 2-29 and 2-30). The lattice mismatch between each step layer was 0.72% (compared to that of the sample grown on an InP substrate, only 0.43%), all the buffer layers were fully relaxed for a layer thickness of 250nm.

The effectiveness of the cyclic annealing step-graded buffer layers to prevent the TDs from propagating into the top layer is clearly shown in XTEM pictures in Fig. 2-33. The density of TDs in the top InGaAs device layer was estimated to be around  $5 \times 10^7/\text{cm}^2$  by comparing XTEM pictures at different locations. It was clearly observed that TDs in the step layers bent over at the interfaces and annihilated each other.



**Figure 2-34: XTEM of InGaAs device layer grown on InP substrate with five-step graded InAlAs buffer layers (the first step was missing during the mechanical sample preparing process).**

### **2.3.5 Optical characterization**

RTPL measurement was used to characterize the optical quality of the InGaAs device layers grown on the cyclic annealed step-graded metamorphic InAlAs buffer layers on GaAs and InP substrates. The RTPL setup was described previously in this chapter. The samples had an  $\text{In}_{0.82}\text{Al}_{0.18}\text{As}$  capping layer to provide additional carrier confinement in the InGaAs layers. As shown in Fig. 2-34, the sample grown on InP had a higher PL peak intensity than that of the sample grown on a GaAs substrate. Both samples have similar FWHM for the PL emission peaks of around 70meV.

From the optical absorption (transmission) measurement (as shown in Fig. 2-35), the absorption edge for the InGaAs device layer grown on GaAs substrates showed an absorption edge at  $\sim 2.5\mu\text{m}$  and the absorption coefficient at  $2.45\mu\text{m}$  was estimated to be  $\sim 3300\text{cm}^{-1}$ .

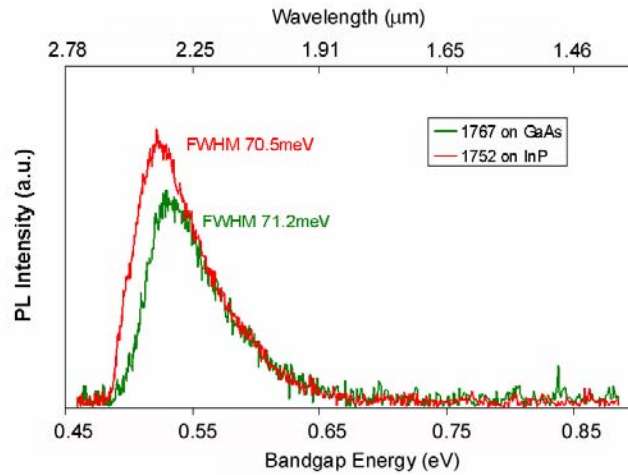


Figure 2-35: RTPL of samples grown on InP and GaAs substrates.

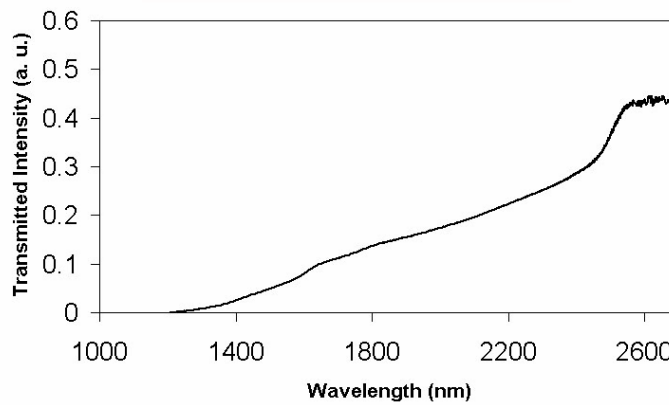


Figure 2-36: Optical absorption of InGaAs device layers grown on GaAs substrates with step-graded metamorphic buffer layers.

### 2.3.6 CONCLUSION

In summary, high-quality  $\text{In}_{0.8}\text{Ga}_{0.2}\text{As}$  thick ( $1\mu\text{m}$ ) layers were grown on InP and GaAs substrates by SSMBE with photoluminescence and optical absorption sensitive wavelength around  $2.5\mu\text{m}$ . The thick InGaAs device layers were grown on cyclic in-situ arsenic-assisted annealed step-graded metamorphic InAlAs buffer layers. Low temperature growth, followed by high-temperature thermal annealing, was essential to achieve almost fully-relaxed step layers with smooth surface morphology. As the indium content increased from lattice-matched buffer layer to the top metamorphic grown step-

graded layer, it was beneficial to decrease the growth temperature correspondingly. The formation of two different types of dislocations,  $\alpha$  dislocations gliding along [011] direction and  $\beta$  dislocations gliding along  $[0\bar{1}1]$  direction, could be balanced. Cyclic in-situ annealing step-graded buffer layers could be promising to fabricate InGaAs/InAlAs based HEMTs and thermal photovoltaic cells which need high-quality materials with bandgap energies less than 0.6eV.

## 2.4 Summary

In this chapter, MBE techniques are developed to investigate various InGaAs-based material systems. Various intrinsic layers are grown on InP and GaAs substrates:  $(\text{In}_{0.532}\text{Ga}_{0.468}\text{As})_x(\text{In}_{0.523}\text{Al}_{0.477}\text{As})_{1-x}$  and  $\text{In}_{0.532}\text{Ga}_{0.468}\text{As}_y\text{N}_x\text{Sb}_{2.56x}$  are lattice-matched to InP substrates;  $\text{In}_x\text{Ga}_{1-x}\text{As}/\text{In}_y\text{Ga}_{1-y}\text{As}$  strain-balanced superlattices (MQW) and  $\text{In}_{0.532}\text{Ga}_{0.468}\text{As}/\text{InAs}$  (1:3) fractional monolayer superlattices are pseudomorphic, highly strained on InP substrates; thick device layers of  $\text{In}_{x>0.8}\text{GaAs}$  are lattice-matched to the relaxed metamorphic InAlAs buffers on InP and GaAs substrates. In-situ process monitoring and ex-situ material quality characterization are used to help extend the emission and absorption wavelength range to beyond  $2\mu\text{m}$  for the application of photodetection in NIR region.

## References:

1. Information from various substrate vendors, AXT, WT, Sumitomo, InPact to name some of them, also in the online magazine [www.compoundsemiconductor.org](http://www.compoundsemiconductor.org), [www.three-fives.com](http://www.three-fives.com), et.al.
2. R. E. Nahory, M. A. Pollack, W. D. Johnson, R. L. Barns, "Bandgap versus composition and demonstration of Vegard's law for  $\text{In}_{1-x}\text{Ga}_x\text{As}_y\text{P}_{1-y}$  lattice matched to InP", Appl. Phys. Lett., 33 (7) 659-661, 1978
3. E. Kuphal, "Phase diagrams of InGaAsP, InGaAs and InP lattice matched to (100) InP", J. Crystal Growth, 67 (3) 441-457, 1984
4. E. Tournie, Y. H. Zhang, N. J. Pulsford, K. Ploog, "Structural and optical properties of  $\text{Al}_{0.48}\text{In}_{0.52}\text{As}$  layers grown on InP by MBE: influence of the substrate temperature and of a buffer layer", J. Appl. Phys., 70 (12) 7362-7369, 1991

5. S. T. Chou, K. Y. Cheng, "High quality  $\text{In}_{0.52}\text{Al}_{0.48}\text{As}$  grown by modulated arsenic MBE", *Appl. Phys. Lett.*, 63 (20) 2815-2817, 1993
6. J. P. Praseuth, M. C. Joncour, J. M. Gerard, P. Henoc, M. Quillec, "Growth and characterization of  $\text{AlGaInAs}$  lattice matched to  $\text{InP}$  grown by MBE", *J. Appl. Phys.*, 63 (2) 400-403, 1988
7. B. Lambert, Y. Toudic, Y. Rouillard, M. Gauneau, M. Baudet, F. Alard, I. Valiente, J. C. Simon, "high reflectivity  $1.55\mu\text{m}$   $(\text{Al})\text{GaAsSb}/\text{AlAsSb}$  Bragg reflector lattice matched on  $\text{InP}$  substrates", *Appl. Phys Lett.*, 66 (4) 442-444, 1995
8. T. Shitara, K. Eberl, "Electronic properties of  $\text{InGaP}$  grown by solid-source MBE with a  $\text{GaP}$  decomposition source", *Appl. Phys. Lett.*, 65 (3) 356-358, 1994
9. C. Lenox, H. Nie, G. Kinsey, C. Hansing, J. C. Campbell, A. L. Holmes, Jr., B. G. Streetman, "Substrate preparation and interface grading in  $\text{InGaAs}/\text{InAlAs}$  photodiodes grown on  $\text{InP}$  by MBE", *J. Vac. Sci. Technol. B*, 17 (3) 1175-1179, 1999
10. J. F. Wager, D. L. Ellsworth, S. M. Goodnick, C. W. Wilmsen, "Composition and thermal stability of thin native oxides on  $\text{InP}$ ", *J. Vac. Sci. Technol.*, 19 (3) 513-518, 1981
11. G. Hollinger, E. Bergignat, J. Joseph, Y. Robach, "On the nature of oxides on  $\text{InP}$  surfaces", *J. Vac. Sci. Technol. A*, 3 (6) 2082-2088, 1985
12. S. Ohkouchi, N. Ikoma, I. Tanaka, "Surface structure of  $\text{InP}$  and  $\text{InAs}$  thermally cleaned in an arsenic flux", *J. Vac. Sci. Technol. B*, 12 (3) 2033-2036, 1994
13. J. Fu, S. Bank, M. Wistey, H. Yuen, J. S. Harris, Jr., "Solid-source MBE growth of  $\text{GaInNASb}/\text{InGaAs}$  SQW on  $\text{InP}$  with photoluminescence peak wavelength at  $2.04\mu\text{m}$ ", *J. Vac. Sci. Technol. B*, 22 (3) 1463-1467, 2004
14. M. Kondow, K. Uomi, A. Niwa, T. Kitatani, S. Watahiki, Y. Yazawa, " $\text{GaInNAS}$ : a novel material for long-wavelength-range laser diodes with excellent high-temperature performance", *J. Jan. Appl. Phys. Part 1*, 35 (2B) 1273-1275, 1996
15. M. C. Larson, M. Kondow, T. Kitatani, K. Nakahara, K. Tamura, H. Inoue, K. Uomi, " $\text{GaInNAS-GaAs}$  long-wavelength vertical-cavity surface-emitting laser diodes", *IEEE Photon. Tech. Lett.*, 10 (2) 188-190, 1998
16. J. S. Harris, Jr., " $\text{GaInNAS}$  long wavelength lasers: progress and challenges", *Semicon. Sci. Technol.*, 17 (8) 880-891
17. W. Shan, W. Walukiewica, J. W. Ager, E. E. Haller, J. F. Geisz, D. J. Friedman, J. M. Olson, S. R. Kurtz, "Band anti-crossing in  $\text{GaInNAS}$  alloys", *Phys. Rev. Lett.*, 82 (6) 1221-1224, 1999
18. E. D. Jones, N. A. Modine, A. A. Allerman, S. R. Kurtz, A. F. Wright, S. T. Tozer, X. Wei, "Band structure of  $\text{In}_x\text{Ga}_{1-x}\text{As}_{1-y}\text{N}_y$  alloys and effects of pressure", *Phys. Rev. B*, 60 (7) 4430-4433, 1999

19. W. Shan, W. Walukiewica, J. W. Ager, E. E. Haller, J. F. Geisz, D. J. Friedman, J. M. Olson, S. R. Kurtz, "Effect of nitrogen on the band structure of GaInNAs alloys", *J. Appl. Phys.*, 86 (4) 2349-2351, 1999
20. J. S. Harris, Jr., "(GaIn)(NAsSb): the challenges for long wavelength communication devices", *Proceedings Compound Semiconductors*, vol. 184, 63-72, 2005
21. K. Volz, V. Gambin, W. Ha, M. A. Wistey, H. Yuen, S. Bank, J. S. Harris, Jr., "The role of Sb in the MBE growth of (GaIn)(NAsSb)", *J. Cryst. Growth*, 251 (1-4) 360-366, 2003
22. S. B. Zhang, A. Zunger, "Surface-reconstruction-enhanced solubility of N, P, As, and Sb in III-V semiconductors", *Appl. Phys. Lett.*, 71 (5) 677-679, 1997
23. S. B. Zhang, S. H. Wei, "Nitrogen solubility and induced defect complexes in epitaxial GaAs:N", *Phys. Rev. Lett.*, 86 (9) 1789-1792, 2001
24. W. G. Bi, C. W. Tu, "Bowling parameter of the bandgap energy of GaN<sub>x</sub>As<sub>1-x</sub>", *Appl. Phys. Lett.*, 70 (12) 1608-1610, 1997
25. M. Knodow, T. Kitatani, "Molecular beam epitaxy of GaNAs and GaInNAs", 17 (8) 746-754, 2002
26. "Long wavelength GaInNAs and GaInNAsSb lasers on GaAs" by W. Ha, Stanford University PhD dissertation, 2002
27. D. J. Friedman, J. F. Geisz, S. R. Kurtz, J. M. Olson, R. Reedy, "Nonlinear dependence of N incorporation on In content in GaInNAs", *J. Cryst. Growth*, 195 (1-4) 438-443, 1998
28. S. G. Spruytte, C. W. Coldren, J. S. Harris, W. Wampler, P. Krispin, K. Ploog, M. C. Larson, "Incorporation of nitrogen in nitride-arsenide: origin of improved luminescence efficiency", *J. Appl. Phys.*, 89 (8) 4401-4406, 2001
29. V. Lordi, V. Gambin, S. Friedrich, T. Funk, T. Takizawa, K. Uno, J. S. Harris, "Nearest-neighbor configuration in (GaIn)(NAs) probed by X-ray absorption spectroscopy", *Phys. Rev. Lett.*, 90 (14) 145505/1-4, 2003
30. "Mechanical properties of thin films" by W. D. Nix, Stanford University, Course-notes, MSE353, 2002
31. P. R. Berger, K. Chang, P. Bhattacharya, J. Singh, K. K. Bajaj, "Role of strain and growth conditions on the growth front profile of In<sub>x</sub>Ga<sub>1-x</sub>As on GaAs during the pseudomorphic growth regime", *Appl. Phys. Lett.*, 53 (8) 684-686, 1988
32. "Physics and technology of heterojunction devices", edited by D. Vernon Morgan and Robin H. Williams, INSPEC 1990
33. S. Tundo, M. Mazzer, L. Nasi, L. Lazzarini, G. Salviati, C. Rohr, P. Abbott, D. B. Bushnell, K. W. J. Barnham, G. Clarke, R. Peng, "Electron-beam-induced current and cathodoluminescence characterization of InGaAs strain-balanced multi-quantum well photovoltaic cells", *J. Appl. Phys.*, 94 (10) 6341-6345, 2003

34. S. Jourba, M. Gendry, O. Marty, M. Pitaval, G. Hollinger, "High quality highly strained InGaAs quantum wells on InP using  $(\text{InAs})_n(\text{GaAs})_{0.25}$  fractional monolayer superlattices", *Appl. Phys. Lett.*, 75 (2) 220-222, 1999
35. A. Zunger, "Spontaneous atomic ordering in semiconductor alloys: causes, carriers, ad consequences", *MRS Bulletin*, 22 (7) 20-26, 1997
36. J. Fu, X. Yu, Y. Kuo, J. S. Harris, Jr., "Near-infrared photodetection using Molecular Beam Epitaxy grown extended InGaAs", *Proceedings MRS 2005*, San Francisco, CA Mar. 28 – Apr. 1, 2005
37. J. Fu, X. Yu, Y. Kuo, J. S. Harris, Jr., "Extended InGaAs/InGaAs Quantum Structure for Near Infrared Photodetection beyond  $1.9\mu\text{m}$ ", *CLEO/QELS 2005*, Baltimore, Maryland May 22 - 27, 2005
38. B. W. Dodson, J. Y. Tsao, "Structural relaxation in metastable strained layer semiconductors", *Annu. Rev. Mater. Sci.*, 19, 419-437, 1989
39. S. C. Jain, M. Willander, H. Maes, "Stresses and strains in epilayers, stripes and quantum structures of III-V compound semiconductors", *Semicond. Sci. Technol.*, 11, 641-671, 1996
40. L. B. Freund, "A criterion for arrest of a threading dislocation in a strained epitaxial layer due to an interface misfit dislocation in its path", *J. Appl. Phys.*, 68 (5) 2073-2080, 1990
41. A. E. Romanov, W. Pompe, S. Mathis, G. E. Beltz, J. S. Speck, "Threading dislocation reduction in strained layers", *J. Appl. Phys.*, 85 (1) 182-192, 1999
42. S. K. Mathis, X. H. Wu, A. E. Romanov, J. S. Speck, "Threading dislocation reduction mechanisms in low-temperature-grown GaAs", *J. Appl. Phys.*, 86 (9) 4836-4842, 1999
43. M. Zaknune, B. Bonte, C. Gaquiere, Y. Cordier, Y. Druelle, D. Theron, Y. Crosnier, "InAlAs/InGaAs metamorphic HEMT with high current density and high breakdown voltage", *IEEE Electron. Dev. Lett.*, 19 (9) 345-347, 1998
44. W. E. Hoke, P. S. Lyman, C. S. Whelan, J. J. Mosca, A. Torabi, K. L. Chang, K. C. Hsieh, "Growth and characterization of metamorphic  $\text{In}_x(\text{AlGa})_{1-x}\text{As}/\text{In}_x\text{Ga}_{1-x}\text{As}$  high electron mobility transistor material and devices with  $x=0.3-0.4$ ", *J. Vac. Sci. Technol. B*, 18 (3) 1638-1641, 2000
45. R. U. Martinelli, T. J. Zamerowski, P. A. Longeway, " $2.6\mu\text{m}$  InGaAs photodiodes", *Appl. Phys. Lett.*, 53 (11) 989-991, 1988
46. Y. G. Chai, R. Chow, "Molecular beam epitaxial growth of lattice-mismatched  $\text{In}_{0.77}\text{Ga}_{0.23}\text{As}$  on InP", *J. Appl. Phys.*, 53 (2) 1229-1232, 1982
47. F. Romanato, E. Napolitani, A. Carnera, A. V. Drigo, L. Lazzarini, G. Salviati, C. Ferrari, A. Bosacchi, S. Franchi, "Strain relaxation in graded composition  $\text{In}_x\text{Ga}_{1-x}\text{As}/\text{GaAs}$  buffer layers", *J. Appl. Phys.*, 86 (9) 4748-4755, 1999
48. M. K. Hudait, Y. Lin, M. N. Palmisiano, C. Tivarus, J. P. Pelz, S. A. Ringel, "Comparison of mixed anion,  $\text{InAs}_y\text{P}_{1-y}$  and mixed cation,  $\text{In}_x\text{Al}_{1-x}\text{As}$  metamorphic

- buffers grown by MBE on (100) InP substrates”, *J. Appl. Phys.*, 95 (8) 3952-3960, 2004
49. J. Fu, X. Yu, Y. Kuo, J. S. Harris, Jr., “Metamorphic growth of wavelength-extended InGaAs on InP with cycling in-situ annealed step-graded InAlAs and InGaAs buffers”, EMC, Santa Barbara, California, June 24-26, 2005
  50. A. M. Andrews, J. S. Speck, A. E. Romanov, M. Bobeth, W. Pompe, “Modeling cross-hatch surface morphology in growing mismatched layers”, *J. Appl. Phys.*, 91 (9) 1933-1943, 2002
  51. M. Quillec, L. Goldstein, G. Leroux, J. Burgeat, J. Primot, “Growth conditions and characterization of InGaAs/GaAs strained layers superlattices”, *J. Appl. Phys.*, 55 (8) 2904-2909, 1984
  52. I. C. Bassignana, C. J. Miner, N. Puetz, “Photoluminescence and double-crystal X-ray study of InGaAs/InP: effect of mismatch strain on band gap”, *J. Appl. Phys.*, 65 (11) 4299-4305, 1989
  53. P. F. Fewster, N. L. Andrew, “Determining the lattice relaxation in semiconductor layer systems by X-ray diffraction”, *J. Appl. Phys.*, 74 (5) 3121-3125, 1993
  54. J. A. Olsen, E. L. Hu, S. R. Lee, I. J. Fritz, A. J. Howard, B. E. Hammons, J. Y. Tsao, “X-ray reciprocal-space mapping of strain relaxation and tilting in linearly graded InAlAs buffers”, *J. Appl. Phys.*, 79 (7) 3578-3584, 1996
  55. J. M. Chauveau, Y. Androussi, A. Lefebvre, J. Di Persio, Y. Cordier, “Indium content measurement in metamorphic high electron mobility transistor structures by combination of X-ray reciprocal space mapping and transmission electron microscopy”, *J. Appl. Phys.*, 93 (7) 4219-4225, 2003

## **CHAPTER 3 DEVICE DESIGN, FABRICATION AND CHARACTERIZATION**

In the previous chapter, material systems based on InP and GaAs were investigated with photoluminescence and absorption over a wavelength range extending as far as 2.5 $\mu\text{m}$ . As discussed in chapter 1, detectors are the most important components in a SDT IR system and the overall system performance, such as sensitivity, responsivity and frequency response depend almost entirely on the performance of the detectors. Not only the material quality, but also the device structure and optimized design determine the detector performance. Detectors fabricated using the materials systems studied so far cover the entire wavelength range of interest and would fulfill most applications in the fields of telecommunications, non-invasive specimen analysis, environmental gas detection and hyper-spectral imaging and sensing. In this chapter, the design, fabrication and characterization of photodetection devices for application to a standing-wave transform spectrometer will be discussed.

### **3.1 Detector and linearity**

Of the two types of detectors, energy detectors and photon detectors (chapter 1), we are more interested in photon detectors for applications requiring high performance photodetection. There are many photodetectors based on related operating mechanisms, such as photoconductors, p-n junction photodiodes, p-i-n photodiodes, Schottky barrier diodes, avalanche photodiodes, phototransistors, intersubband quantum well and quantum dot photodetectors. For application to the NIR standing-wave transform spectrometer, the most important aspects of performance of detectors include: the spectral response, responsivity (detectivity) and linearity. The spectral response is directly related to the material selection of the active absorption region (longest wavelength of light detected is  $\lambda(\mu\text{m})=1.24/E_g(\text{eV})$  where  $E_g$  is the bandgap energy of the material) and the last two depend on the structure design and fabrication processes. For the sake of system simplicity, p-i-n photodiodes and phototransistors will be the focus of this chapter and the differences in the two detectors come mostly from the different device structures.

### 3.1.1 p-i-n photodiode

Photodiode detectors are based upon junctions formed by different doping regions of either the same (homojunction) or different (heterojunction) materials. p-n junction photodiodes and p-i-n photodiodes are two similar device structures that are normally operated under reverse bias for high collection efficiency of photon-generated free carriers. For a p-n photodiode, the output current in the detector includes both the diode dark current and photocurrent. The ideal reverse bias diode dark current saturates and is independent of the diode bias in Eq. (3-1) [1],

$$j_d = q \left( \frac{D_p}{L_p} p_{n0} + \frac{D_n}{L_n} n_{p0} \right) \quad (3-1)$$

where all terms have the normal meaning,  $q$  the electron charge,  $D_p$ ,  $D_n$ , the diffusion coefficients for holes and electrons,  $L_p$ ,  $L_n$  the diffusion lengths of holes and electrons, and  $L = \sqrt{D \cdot \tau}$  where  $\tau$  is the carrier lifetime,  $p_{n0}$  ( $n_{p0}$ ) the hole (electron) concentration in the absence of any electric field or optical injection in the  $n$  ( $p$ ) region. The photocurrent for a p-n photodiode is dependent on the illumination intensity (negative sign refers to the bias voltage direction) in Eq. (3-2),

$$j_{ph} = -qG_0(L_p + L_n) = -q\eta \frac{P_{opt}/h\nu}{lA} (L_p + L_n) \quad (3-2)$$

where  $G_0$  is the optical generation rate,  $G_0 = \eta \frac{P_{opt}/h\nu}{lA}$ ,  $\eta$  is the quantum efficiency (fraction of incident photons generating electron-hole pairs),  $P_{opt}/h\nu$  the photon flux, and  $l$  the thickness or vertical dimension of the detector.

A p-i-n photodiode uses an intrinsic region (particularly in this dissertation, the intrinsic region is also a quantum well, and the doped cladding layers have wider bandgap) to enhance the responsivity. The total photocurrent consists of two parts: 1) drift current and 2) diffusion current. The current densities of drift component  $j_{dr}$  and diffusion component  $j_{diff}$  are [1],

$$j_{dr} = -q \frac{I_{opt}}{h\nu} \eta_i (1-R)(1 - e^{-\alpha W})$$

$$j_{diff} = -q \left( \eta_i (1-R) \frac{I_{opt}}{h\nu} \frac{\alpha L_p}{1 + \alpha L_p} e^{-\alpha W} + P_{n0} \frac{D_p}{L_p} \right) \quad (3-3)$$

where  $I_{opt}/h\nu$  is the photon flux per second,  $\eta_i$  the internal quantum efficiency in the intrinsic region,  $\alpha$  the absorption coefficient,  $W$  the intrinsic region thickness,  $R$  the surface reflection loss, and so the quantum efficiency  $\eta$  is,

$$\eta = \eta_i (1-R) \left( 1 - \frac{e^{-\alpha W}}{1 + \alpha L_p} \right) \quad (3-4)$$

Both the p-n and p-i-n photodiodes are basically linear photodetectors, the photocurrent is linearly proportional to the light intensity of the incident light power until very high intensity levels are reached.

### 3.1.2 Phototransistor

A phototransistor includes three regions, collector (C), base (B) and emitter (E). For an npn phototransistor, the base is a thin highly p-type doped region and the other two are relatively thick n-type doped. The operating condition for such a phototransistor is the same as normal bipolar transistor, i.e. the B-E junction is forward biased and the B-C junction is reverse biased [2]. Silicon npn phototransistors have been commercially available for a very long time. Considering our specific applications, a hetero-junction bipolar phototransistor (HPT) will be favored instead of a homojunction silicon phototransistor. A HPT with heterojunction only for B-E junction is called a single-HPT (SHPT) and when both B-E and B-C junctions are heterojunctions, the device is called double-HPT (DHPT).

For a general npn bipolar junction transistor (BJT) with homojunctions for both B-E and B-C junctions, the common-emitter small-signal current gain can be estimated by Eq. (3-5),

$$\beta \approx \frac{D_n N_e X_e}{D_p N_b W} \quad (3-5)$$

where  $X_e$  is the emitter thickness,  $W$  the base thickness,  $N_e$ ,  $N_b$  the impurity (dopant) concentrations in emitter and base, respectively,  $D_n$  the electron diffusion coefficient in the base (p-type doped) and  $D_p$  the hole diffusion coefficient in the emitter (n-type doped). For a heterojunction bipolar transistor (HBT), the current gain can be increased dramatically because of the bandgap discontinuity between the emitter and the base region (emitter has wider bandgap than the base),

$$\beta = \frac{I_c}{I_b} < \beta_{\max} = \frac{v_{nb} N_e X_e}{v_{pe} N_b W} \exp[\Delta E_v / k_B T] \quad (3-6)$$

where  $v_{nb}$  ( $v_{pe}$ ) are the effective velocities of electrons (holes) in the base (emitter) region,  $\Delta E_v$  is the valence band discontinuity at B-E junction (for example, InP/InGaAs junction  $\Delta E_v=0.37\text{eV}$  and correspondingly, the incremental factor for HBT gain,  $\exp[\Delta E_v/k_B T] \sim 10^6$  at 300K).

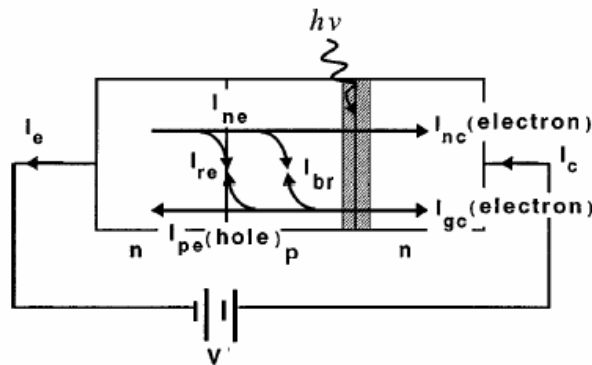


**Figure 3-1: Current components in Npn heterojunction bipolar (photo)transistor [3].**

Above rough estimation of the current gain can be extended to include parameters important to characterization of real devices in different operation modes (Fig. 3-1). In the forward active mode (compared to the reverse active mode mostly only useful for parameter extraction), current components in the device satisfy Eq. (3-7),

$$I_c = I_{nc} + I_{gc}, I_e = I_{ne} + I_{pe} + I_{re}, I_b = I_{pe} + I_{re} - I_{gc} + I_{br} \quad (3-7)$$

where all the current components have the normal meanings,  $I_{ne}$ ,  $I_{nc}$  the electron component of the emitter and collector current, respectively,  $I_{pe}$  the hole component of the emitter current,  $I_{re}$  the recombination current in the depletion region of B-E junction,  $I_{br}$  the recombination current in the neutral base region, and  $I_{gc}$  the generation current in the depletion region of B-C junction.

In the low injection regime (diffusion current dominant), the current gain  $\beta$  can be estimated to be the ratio of the electron component of emitter current ( $I_{ne} \propto \exp(V_{BE}/V_{th})$ ,  $V_{th}=k_B T/q$ ) and the recombination current in the B-E junction ( $I_{re} \propto \exp(V_{BE}/nV_{th})$ , where empirical number  $n>1$ ). With the increase in the forward emitter-base voltage  $V_{BE}$  (correspondingly an increase of collector current), the diffusion current increases faster than the recombination current, thus the current gain increases ( $\propto e^{(V_{BE}/V_{th} \cdot (1-1/n))} \propto I_c^{(1-1/n)}$ ) to the limiting value set by Eq. 3-5 and Eq. 3-6. In the regime of high injection (the number of electrons injected into the base greater than the Gummel number, defined as the total number of acceptors in the base region), the current gain decreases ( $\propto 1/I_c$ ) as the collector current increases. Taking into account the limiting factor of base transport, common-emitter gain  $\beta_T \approx 2(L_{nb}/W)^2$ , where  $L_{nb}$  is the electron diffusion length in the base and  $W$  the base width, the current gain of BJT (HBT) increases with an increase of  $I_c$  at low injection levels, saturates to the maximum value at moderate injection levels and then decreases due to high-injection effects. The Kirk effect (high-field region shift from B-E junction to B-C junction due to the carrier injection into the collector region) is another source of the decrease of common-emitter current gain.

The HPT is basically not much different than a HBT except that the photocurrent generated in the base (and B-C junction) region itself is the input signal instead of electric current from the circuit. Different from the short circuit small-signal current gain of a HBT, the optical gain is of more interest in describing the HPT device function. In a

SHPT with photon absorption in the base and B-C junction region, the photocurrent (primary) is,

$$I_{ph} = qA \frac{P_{opt}}{h\nu} \left( 1 - \frac{\exp[-\alpha(W + w_{BC})]}{\alpha L_p + 1} \right) \quad (3-8)$$

while a detailed analysis of HPT gives the expression of collector current in Eq. (3-9) [4],

$$\begin{aligned} -I_c = & (1 + \beta)qA \frac{P_{opt}}{h\nu} \left[ 1 - \frac{\exp(-\alpha w_{BC})}{\alpha L_p + 1} \right] \exp(-\alpha W) + (1 + \beta)qA \frac{\alpha^2 L_n^2}{(\alpha^2 L_n^2 - 1) \cosh(W / L_n)} \cdot \\ & \frac{P_{opt}}{h\nu} \left[ 1 - \left( \cosh\left(\frac{W}{L_n}\right) + \frac{1}{\alpha L_n} \sinh\left(\frac{W}{L_n}\right) \right) \exp(-\alpha W) \right] + (1 + \beta)I_{c0} \quad (3-9) \end{aligned}$$

where the first two terms are related to the general photocurrent and the last term is

related to the phonon-excited dark current  $I_{c0} = qA \left( \frac{D_p}{L_p} p_{n0} + \frac{D_n}{L_n} n_{p0} \tanh(W / L_n) \right)$ .

For a typical HPT with a very thin base ( $W / L_n \leq 0.25$ ), the photocurrent in Eq. (3-9) takes the form of Eq. (3-8) with high carrier collection efficiency at the B-C junction. From Eq. (3-9) we can see that the photocurrent and the phonon-excited dark current are both amplified  $(1 + \beta)$  times by the transistor action. From the earlier discussion of current gain dependence on collector current, it should be no surprise that there is a similar dependence on the illumination level, thus the output current will not be linearly proportional to the incident light intensity. The quantum efficiency in the base region,  $\eta$ , can be simplified as  $\eta = (1 - R) \left[ 1 - \frac{\exp[-\alpha(W + w_{BC})]}{\alpha L_p + 1} \right]$ , and the external optical gain  $g$  can be estimated in Eq. (3-10),

$$g = (1 + \beta) \cdot \eta = (1 + \beta)(1 - R) \left[ 1 - \frac{\exp[-\alpha(W + w_{BC})]}{\alpha L_p + 1} \right] \quad (3-10)$$

The optical gain of a HPT is highly dependent on the base width, doping levels (shown in Fig. 3-2 [5]), material qualities (especially recombination centers due to defects in the B-E junction) as well as the illumination level (corresponding to different level of collector current). Eq. (3-9) ignores the recombination current in the heterojunctions, so the optical gain of a HPT considering the non-ideal heterojunction due to recombination, tunneling and avalanching, the internal optical gain can be expressed in Eq. (3-11) [3] (refer to Fig. 3-1),

$$g_0 = \frac{I_c}{I_{gc}} = \frac{(I_{ne} + I_{pe} + I_{re})(1 + \beta)}{I_{ne} + I_{pe} + I_{re}(1 + \beta)} \quad (3-11)$$

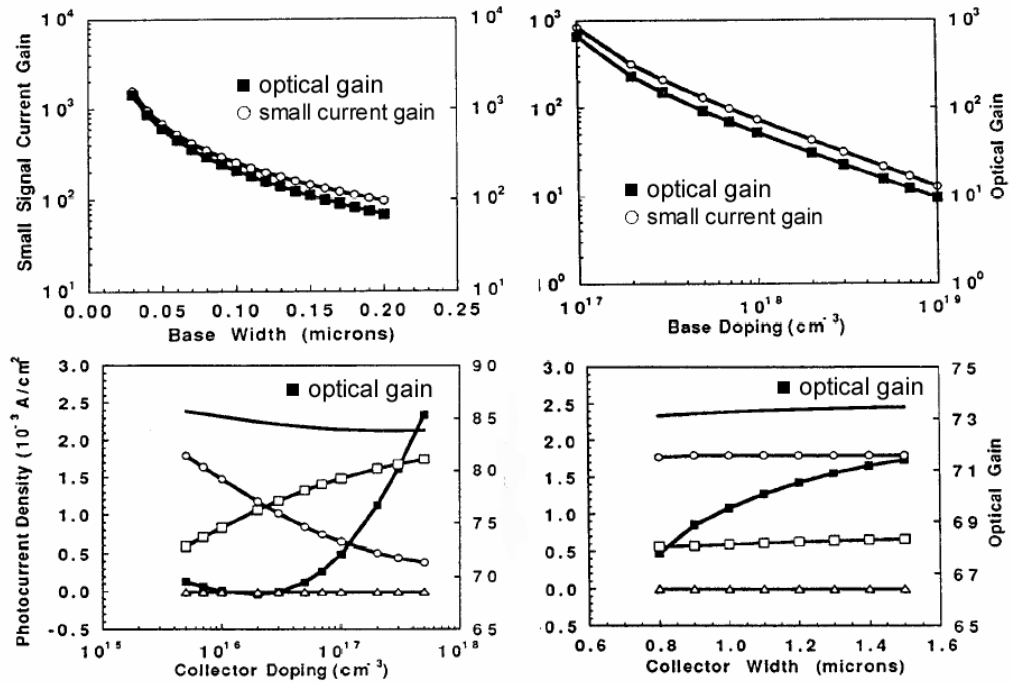


Figure 3-2: Scaling law of Npn HPT on the optical gain and small signal current gain, as well as the photocurrent density in the device (dependence on the collector, bottom two figures, total photocurrent density (no symbol), component in the quasi-neutral base ( $\bar{y}$ ), B-C space charge region ( $\bar{u}$ ) and collector region ( $\bar{u}$ )) [5].

If the illumination level is low ( $V_{BE}$  small,  $I_{ne}+I_{pe}<I_{re}$ ), the optical gain keeps a constant small value independent of the collector current; if the illumination level is moderate ( $I_{ne}+I_{pe}>I_{re}$  but  $I_{ne}+I_{pe}<\beta I_{re}$ ), then the optical gain is dependent on the collector current; if the illumination level is high ( $I_{ne}+I_{pe}>\beta I_{re}$ ), the internal optical gain is only dependent on the current gain of HBT.

From above analysis, a HPT has a different design criteria and different operating regions from a HBT. A HBT is always biased so that the device provides excellent linear amplification in a relatively broad constant gain region ( $\sim 100$ ) between recombination limit and high-injection limit regions. For a HPT, the optical gain region corresponds to a light level down to zero, so the small-signal current gain  $\beta$  can be even less than 1 in the recombination-limiting region for low-level illumination. Because the extremely high possible gain ( $10^6$ ) due to the bandgap discontinuity in valence bands is possible and desirable for the design of HPT, the high injection region can be reached with very low photocurrent. So the linear operating region is significantly reduced for a HPT compared with that of a HBT. The operating region of a HPT transits from the recombination-limiting region to the high-injection limiting region within only a relatively small range of illumination levels.

In summary, the p-i-n photodiode detector is a linear detector, with output current linearly proportional to the incident light intensity and dark current extremely low with no-bias-voltage operation mode. The npn phototransistor is a non-linear photodetector and the optical gain is not constant for a wide range of illumination levels. We will make use of this unique property of HPT in the next chapter.

### **3.2 Device design and fabrication**

For photodetection applications, Si, GaAs and InP based material systems are possible choices covering a wide wavelength range from visible light to the NIR region. Because of the high absorption coefficient and mature technology on material growth and device fabrication, detectors fabricated on GaAs and InP substrates will have much higher quantum efficiency and better performance than Si detector. In this chapter,

lattice-matched material systems will be the main focus including AlGaAs/GaAs and InP/InGaAs/InAlAs structures. As discussed in chapter 1, the photodetection devices in a standing wave Fourier-transform spectrometer (folded Michelson spectrometer) need be partially transparent with a very thin active region, so quantum-well like structures will be utilized for both the p-i-n photodiode and npn DHPT. The system performance related design on the device structures will be described in chapter 4.

### 3.2.1 AlGaAs/GaAs p-i-n photodiodes

The lattice constant of AlAs is  $5.6611\text{\AA}$ , which is very close ( $\sim 0.14\%$ ) to that of GaAs  $5.6533\text{\AA}$ . So the material system of AlGaAs/GaAs is generally regarded as a lattice-matched materials system on GaAs substrates. Several general parameters of the  $\text{Al}_x\text{Ga}_{1-x}\text{As}$ /GaAs system are important for the p-i-n photodiode detector design, including bandgap energy of  $\text{Al}_x\text{Ga}_{1-x}\text{As}$   $(1.424+1.247x)\text{eV}$  for  $x < 0.45$  or  $(1.9+0.125x+0.143x^2)\text{eV}$  for  $0.45 < x < 1.0$ ; bandgap discontinuity of valence band  $\Delta E_v = 0.4\Delta E_g$ ; absorption coefficient and refractive index of intrinsic GaAs, which are shown in Fig. 3-3.

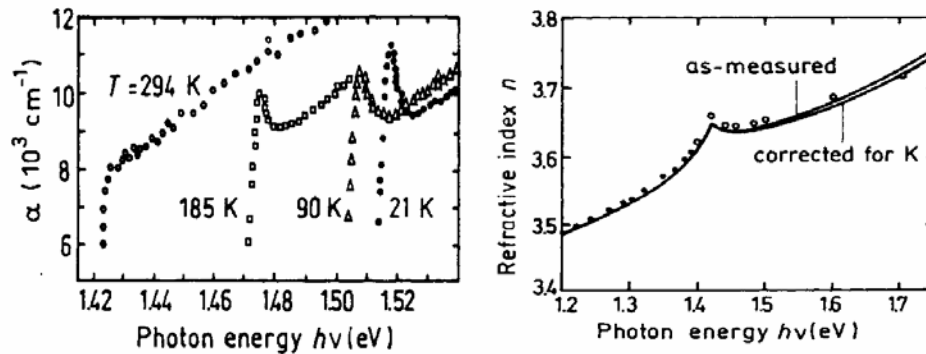
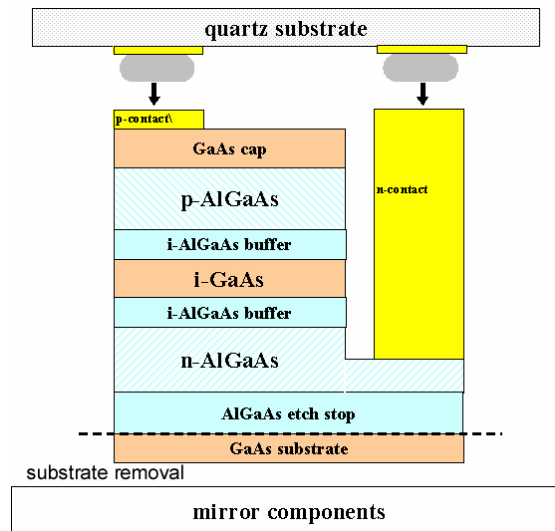


Figure 3-3: Absorption coefficient ( $\alpha$ ) and refractive index ( $n$ ) of intrinsic GaAs [6].

The samples were grown in the Gen-II MBE system-I and the general growth process was described in chapter 2. After surface deoxidization and thermal cleaning, a thin GaAs buffer layer was grown, followed by an  $\text{Al}_{0.85}\text{Ga}_{0.15}\text{As}$  etch-stop layer (high wet-etching selectivity over GaAs) for subsequent substrate removal, a n-type doped (500nm, Si-doping level  $5 \times 10^{17} \text{ cm}^{-3}$ ) and intrinsic (50nm)  $\text{Al}_{0.3}\text{Ga}_{0.7}\text{As}$  layer followed by

the absorption active region, intrinsic GaAs (55nm, the layer thickness design criteria will be discussed in chapter 4), intrinsic (50nm) and p-type doped (250nm, Be-doping level  $5 \times 10^{17} \text{ cm}^{-3}$ )  $\text{Al}_{0.3}\text{Ga}_{0.7}\text{As}$ , and a very thin capping layer of highly doped GaAs for protection of the AlGaAs layer and Ohmic contact enhancement. The full structure is shown in Fig. 3-4.



**Figure 3-4: AlGaAs/GaAs p-i-n photodiode layer structure, mesa definition, substrate removal and flip-chip bonding for the integration purpose [7].**

The mesa structure of the photodiode (1mm×1mm) can be fabricated by routine lithography and etching process. The processing details are described in Appendix A. The plasma etching of GaAs and AlGaAs layers generates steep side-walls with ion damage. Wet-etching ( $\text{H}_2\text{SO}_4:\text{H}_2\text{O}_2:\text{H}_2\text{O}$  1:8:40) is a simpler process and gives smooth slope side-walls. The Ohmic contacts for both the p-type doped GaAs and n-type doped AlGaAs regions have the same shape of coplanar ring contacts, p-contact of Ti(25nm)/Pt(25nm)/Au(100nm), n-contact of Au/Ge with Ge weight ratio of 12%. Because of the band alignment of GaAs and contact metals, post-evaporation alloy annealing (415°C for 30s) is always needed to further reduce the contact resistivity for good Ohmic contacts.

### 3.2.2 InP/InGaAs/InAlAs DHPT

The MBE growth of lattice-matched (LM) material systems, including  $\text{In}_{0.532}\text{Ga}_{0.468}\text{As}$ ,  $\text{In}_{0.523}\text{Al}_{0.477}\text{As}$  and  $(\text{InGaAs})_x(\text{InAlAs})_{1-x}$ , has been described extensively in chapters 1 and 2. The bandgap energies of LM-InGaAs, InAlAs and InP are 0.75eV, 1.46eV and 1.35eV, respectively. Bandgap discontinuities of InGaAs/InP ( $\Delta E_g=0.6\text{eV}$ ) junction are  $\Delta E_v=0.6\Delta E_g=0.36\text{eV}$  and  $\Delta E_c=0.24\text{eV}$ , while that of InGaAs/InAlAs ( $\Delta E_g=0.71\text{eV}$ ) junction are  $\Delta E_v=0.21\text{eV}$  and  $\Delta E_c=0.5\text{eV}$ . From Eq. (3-6) we can see that the selection of InP/InGaAs as the E-B junction for a HBT (HPT) is favorable due to the large valence band discontinuity. In this section, LM-InGaAs is mostly chosen as the active absorption region and the optical properties are shown in Fig. 3-5.

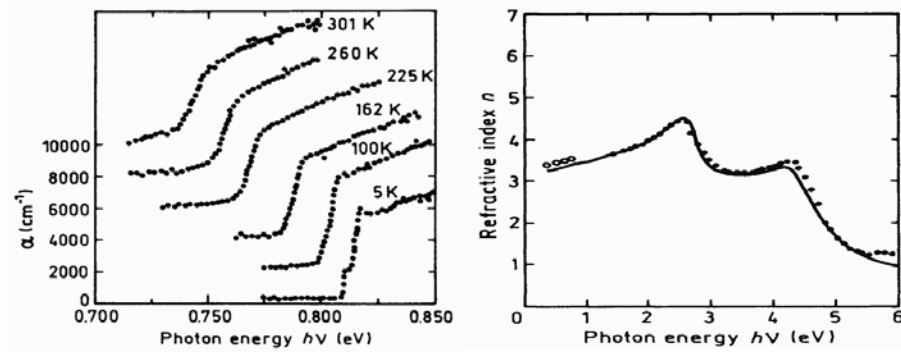
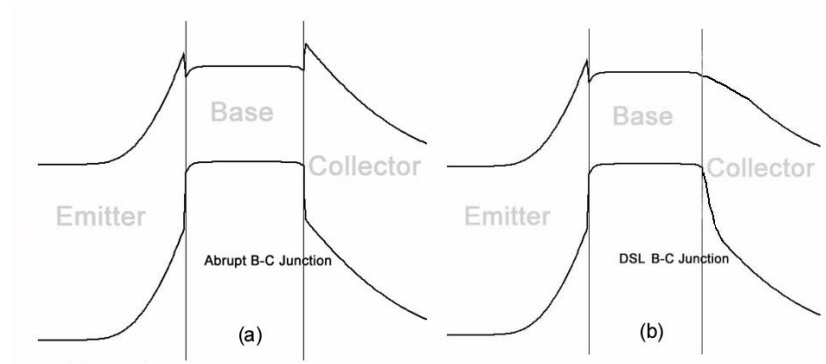


Figure 3-5: Absorption coefficient and refractive index of intrinsic LM-InGaAs [6].

Since the bandgap of base (LM-InGaAs) is 0.75eV, an InP(Emitter)/InGaAs(Base and Collector) based HBT (HPT) will have low turn-on voltage and small breakdown voltage due to the high impact ionization rates at low fields. Thus a DHPT with the structure of InP(E)/ InGaAs(B)/InAlAs(C) is a better device design for low turn-on voltage and higher collector breakdown. However, since the carrier collection efficiency is severely degraded by the energy barrier at the abrupt junction, a graded junction design is necessary to improve device performance. From chapter 2.1, the graded B-C junction can be realized with a digital graded superlattice (DSL)  $(\text{In}_{0.532}\text{Ga}_{0.468}\text{As})_x(\text{In}_{0.523}\text{Al}_{0.477}\text{As})_{1-x}$ , where  $x$  decreases from 1.0 (base side) to 0 (collector side) (as shown in Fig. 3-6).



**Figure 3-6: DHPT with (a) abrupt B-C junction, and (b) graded B-C junction, with energy barrier at B-C junction removed by DSL.**

The theory of HBTs and HPTs was clear for a long time before the materials technology achieved sufficient maturity so that a real device could be fabricated. This was pushed by the needs of long wavelength communications applications [8, 9]. From Eq. (3-9) and (3-11), the material quality (defect control and the reduction of junction interface recombination centers) determined the optical performance of HPTs to an extremely important level. An InP/InGaAs phototransistor was first fabricated in the early 1980's [8, 9], but the performance has been improved significantly over the past two decades due to the outstanding accomplishments in crystal growth technology (such as MBE and MOVPE), processing technology (Inductively Coupled Plasma and RIE dry etching and sub-micron lithography) and extensive improvement in device design [10-12]. Two different device structures, an emitter-up structure and a collector-up structure, which correspond to different illumination directions, were both investigated in this chapter. It has been noticed that material systems with binary layers grown on ternary alloys normally have better material quality than those with ternary layers grown on binary compounds. For application of NIR detection in the standing-wave Fourier-transform spectrometer (next chapter), an emitter-up device structure was utilized to minimize the difference of output current due to back- and front-illumination by the incident and reflected light beams forming the standing-wave interferogram.

All the samples were grown on InP substrates in GEN II MBE system-I with the growth processes described in chapter 2. A GaP sublimation (decomposition) source was

used to grow the InP buffer and emitter regions. Much attention has to be paid to precisely control the LM layer composition. The growth rate of the InGaAs layer was 0.58um/hr and the rate of the InAlAs layer was 0.59um/hr, where the slight difference of growth rate coming from the lattice match condition of the two materials to InP. The layer structure of the collector-up HPT is shown in Fig. 3-7 with DSL graded junctions for both B-E and B-C junctions. The conduction and valence band diagram for the DSL was shown in Fig. 2-3. It consists of 19 periods ( $\times 10\text{nm}$ ) of  $\text{In}_{0.532}\text{Ga}_{0.468}\text{As}/\text{In}_{0.523}\text{Al}_{0.477}\text{As}$  with each period consisting of a layer of InGaAs ranging from 0.5nm to 9.5nm and a corresponding layer of InAlAs ranging from 9.5nm to 0.5nm.

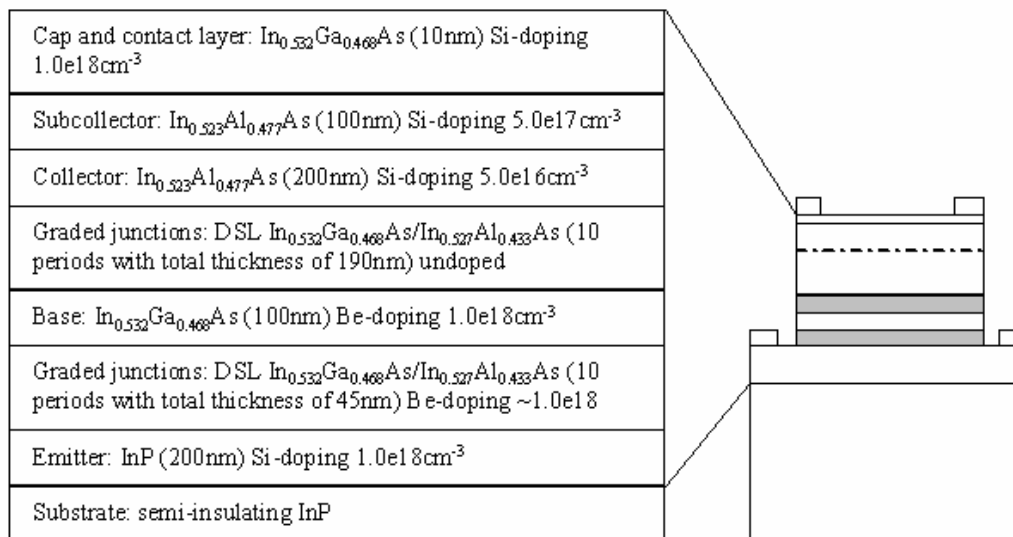


**Figure 3-7: Epi-layers of collector-up Npn InP/InGaAs/InAlAs DHPT, mesa structure and Ohmic contact.**

Compared to RIE and ICP-RIE dry etching, wet etching of mesas produce smoother sidewalls with a less steep slope. Although it is well known that steep sidewalls are critical for sub-micrometer transistors, the surface recombination on the sidewall is not dominant for large mesa-devices. For the sake of simplicity, an all-wet etching process was favored for the phototransistors fabricated in this chapter.  $\text{H}_2\text{SO}_4:\text{H}_2\text{O}_2:\text{H}_2\text{O}$  (1:1:40) was used to etch through the collector and base since the etchant almost perfectly selective-etches InGaAs/InAlAs over InP, and the emitter can be easily exposed by a second single step wet etch (as shown in Fig. 3-7). At room temperature, the etch rate of

InGaAs/InAlAs by such an etchant is close to 200nm/min depending on the relative thickness of InGaAs and InAlAs layers. In order to guarantee etching completely all though the collector and base regions, twenty percent over-etching was performed for the mesa definition. After the mesa etching, the entire sample was passivated by dipping into a buffered oxide etchant (BOE, HF:H<sub>2</sub>O 1:6) for a very short time, followed by rinsing in deionized water for one minute. A thin layer of SiN<sub>x</sub> was deposited by plasma enhanced chemical vapor deposition. Device performance analysis showed that the surface-passivated phototransistors have lower dark current (low surface recombination velocity of InGaAs is 5000cm/s, compared to that of GaAs 10<sup>6</sup>cm/s) and do not degrade as much as unpassivated devices do in the air. Part of the degradation comes from the oxidation process of InGaAs and InAlAs surfaces in air. For large devices, the sidewall slopes make no difference if the exposed surface has been passivated.

For two-terminal DHPT with a floating base, the processing is rather simple. After the collector/base mesa etch, Au/Ge (weight ratio around 88:12) n-type Ohmic contact for emitter and collector can be done in one step. Annealing is not always necessary for n-type contact on InGaAs and InP due to the band structure of metal-semiconductor interface (energy barrier of n-InGaAs/metal is only 0.25eV, and that of p-InGaAs/metal is 0.5eV). Post-evaporation alloy annealing at 400-450°C for 30 seconds will always help to further reduce the contact resistivity. For three-terminal DHPT with a defined base potential, the etch-stop on the base is rather difficult since the base width is always thinner than 100nm and a two-step etching process is needed. Au/Ti/Pt was normally used as p-type Ohmic contact on InGaAs. If the p-type doping was not high enough, annealing is needed to achieve good conductivity while it is well known and characterized by tunneling electron microscopy that metal can penetrate into the underlying layer by as much as tens of nanometers during the annealing process [13]. But for the case of a base contact in a three-terminal phototransistor, the base doping was always high enough to avoid annealing and thus eliminate the metal penetration problem. Improved device performance of a three-terminal HPT compared to a two-terminal HPT has been demonstrated.

The fabricated DHPT is packaged by a standard wire-bonding method in a 24-pin DIP package with customized window opening (hole with diameter 5mm) on the backside for transmission applications.

### 3.3 Device characterization

Both the p-i-n AlGaAs/GaAs photodiode detector and npn InP/InGaAs/InAlAs DHPT fabricated previously are two-terminal devices. The photodiode is operated without any voltage bias across the anode and cathode. The DHPT is operated in a forward active mode with E-B forward biased and B-C reverse biased. With a floating base, the operation of a DHPT is no much different than a normally reverse-biased photodiode. For the purpose of device characterization, a HP4165 semiconductor parameter analyzer, an 810nm laser source for the GaAs-based photodiode and a 1550nm laser source for the InGaAs-based DHPT were used in the electric and optical measurements.

The AlGaAs/GaAs photodiode is designed for the wavelength range from red (AlGaAs cladding layers still transparent) to 870nm (GaAs absorption edge). The fabricated device (1mm×1mm) had a low dark current of 3nA with a 2V reverse bias voltage and the single pass responsivity at 810nm was 34mA/W. The absorption coefficient of intrinsic GaAs at a photon energy of 1.53eV (wavelength 810nm) is about  $1.2 \times 10^4 \text{cm}^{-1}$ . With an intrinsic region thickness of 55nm (single pass optical absorption about 6.4%), refractive index of AlGaAs(GaAs) close to 3.65 (reflection loss of 49%), the calculated responsivity is,

$$\left(1 - e^{-\alpha d}\right) \frac{2n}{n^2 + 1} = 32 \text{mA/W} \quad (3-12)$$

while the internal quantum efficiency is 85% and the internal responsivity ( $e\lambda\eta/hc$ ) is 1.1A/W.

The HPT dark current consists of the leakage current of the base-emitter and base-collector junctions with open loop current gain of the transistor. For a high gain

transistor, the device suffers large dark current (Eq. 3-9). The dark current performance of the phototransistors depends on the fabrication process, material quality and the device structure. It was noticed that different phototransistors on the same wafer through the same fabrication process had different dark current densities. One possible explanation is that defects formed during the material growth are randomly distributed across the wafer surface and different sizes of devices incorporate random number of defects. A phototransistor with an InP-emitter-up structure was fabricated by selective wet-etching InP over the InGaAs(base). In an emitter-floating condition, the phototransistor acted as a normal p-i-n photodiode and the dark current across the B-C junction  $5.28 \times 10^{-7} \text{ A/cm}^2$  with device area  $1 \text{ mm} \times 1 \text{ mm}$ . For the normal forward active mode of the DHPT with the base floating, the dark current density of the phototransistor was  $3.68 \times 10^{-4} \text{ A/cm}^2$  and the relatively constant current gain under different E-C bias was about 700.

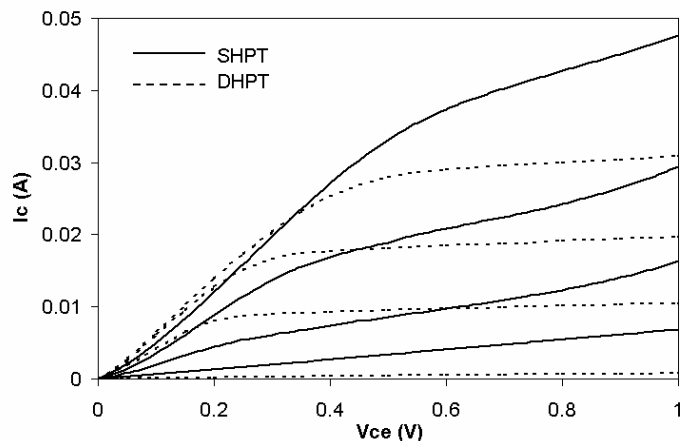


**Figure 3-8: I-V characteristics of SHPT and DHPT.**

SHPT InP/InGaAs and DHPT InP/InGaAs/InAlAs were fabricated and compared. The detection efficiency was characterized by measuring the HPT collector current under illumination by a broadband light source with different power levels as shown in Fig. 3-8. In order to compare the two sets of data from the SHPT and DHPT, the collector current of DHPT was exaggerated to reflect the thickness difference of the InGaAs absorption region. DHPT has much lower dark current density than SHPT because the B-C heterojunction has much lower leakage current [14].

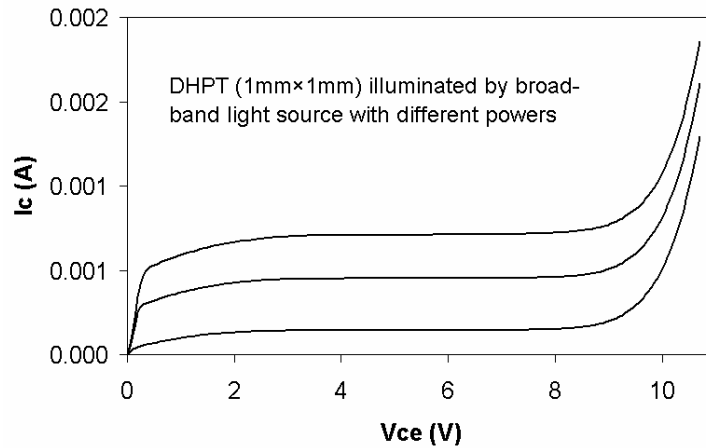


**Figure 3-9: I-V characteristics of DHPT with large C-E voltage bias.**

The responsivity performance of the phototransistors was characterized by illuminating the device with a laser beam at the wavelength of 1550nm and power of 100 $\mu$ W (Gaussian beam waist width around 2.8mm). Taking into account the surface reflection loss and the finite absorption region length, we estimated that the internal current gain of the HPT was about 3000 at a collector-emitter bias of 1V, and the internal quantum efficiency is close to 100%. The overall responsivity of DHPT with 1mm $\times$ 1mm mesa structure is around 19A/W. By applying high voltage across the collector and emitter, the phototransistors died with non-reversible avalanche breakdown. The breakdown voltage was observed to vary wildly among different device sizes. InP/InGaAs SHPTs suffer from low breakdown voltage because of the low breakdown voltage of InGaAs. InP/InGaAs/InAlAs(InP) DHPTs have higher breakdown voltage because InP and InAlAs have smaller ionization rates than InGaAs. There is no observable difference in the breakdown voltage characteristics between graded and abrupt junction HPTs (as shown in Fig. 3-9).

Fig. 3-10 illustrates the behavior of a defective DGHPT. The photon current gain was at a maximum with collector-emitter bias of 2.7V. It was believed that particular defects were incorporated in the heterojunctions and a reversible carrier path was established at higher bias. It was believed that InGaAs/InAlAs interface has high probability to incorporate several types of defects, which may play different roles in the

current-voltage characteristics and need further study in the device design and fabrication processes [15].

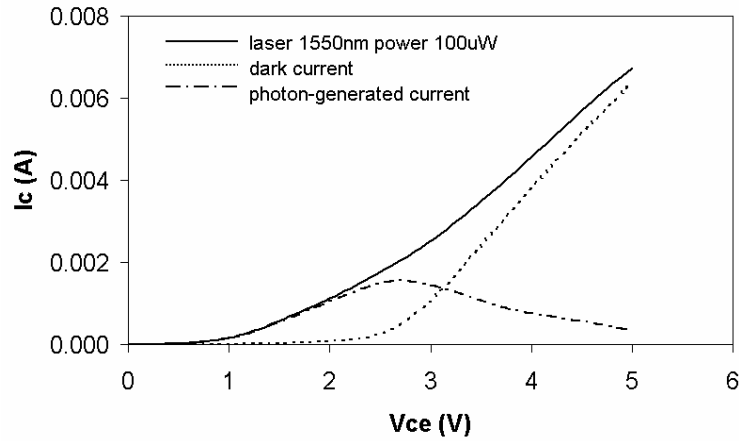


**Figure 3-10: I-V characteristics of a defective DHPT.**

The spectral responsivity of a DHPT (emitter-up structure) was characterized using monochromatically filtered white light source. The measurement results are shown in Fig. 3-11. The photocurrent difference between front and back illumination is partly due to substrate free-carrier absorption, but mostly comes from the light intensity difference at the E-B junction interface under the two illumination conditions. The theoretical analysis in section 3.1 only considered illumination from the emitter side, so that the light intensity at E-B junction was the highest in the quasi-neutral base region. For illumination from the collector side, the light intensity is highest at the C-B junction, so even though the integral light absorption in the base region is the same, independent of the illumination direction, the output currents for the two light illumination cases are different. In the next chapter, we will use this fact to compensate for the single pass loss in the base region to form a standing-wave light field.

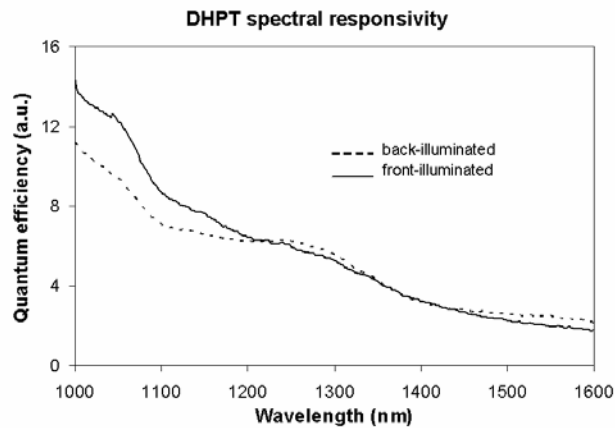


**Figure 3-11: Spectral responsivity characterization of a DHPT with emitter-up structure.**

From the conclusions in section 3.1, when the HPT is operated over a broad intensity range, it is a nonlinear photodetector with an output current that is not linearly proportional to the incident light intensity. This property is clearly shown in Fig. 3-12. The collector saturation effect, corresponding to the decrease of the optical gain, was due to the high-level injection effects described in section 3.1.

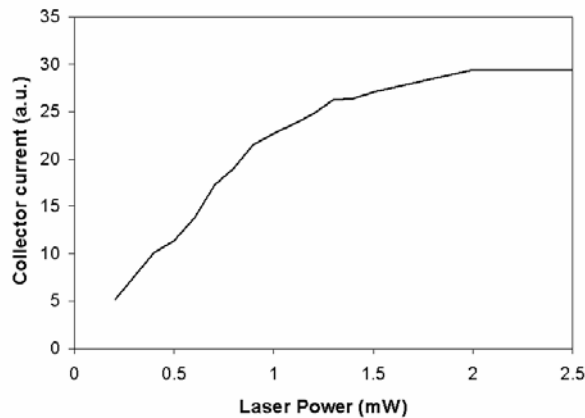


**Figure 3-12: Collector current characteristics with different incident laser powers.**

Since a DHPT with a very thin base region is particularly interesting for our applications, let us review the base width effect again from another view different from Eq. 3-10 and Fig. 3-2. Eq. 3-5 is rewritten here as,

$$G = \frac{N_e w_e D_{nb}}{N_b w_b D_{pe}} \quad (3-5)$$

For a very thin active region width of  $w_b$ , the photon absorption ratio is,  $r = 1 - e^{-\alpha \cdot w_b} \approx \alpha \cdot w_b$ , and the collector current for a specific illumination light power in the constant gain region can be simplified as Eq. (3-13),

$$j \propto P \cdot \eta \cdot G \cdot r \approx \frac{P \alpha N_e w_e D_{nb}}{N_b D_{pe}} \quad (3-13)$$

It is interesting to note that within this approximation, at a specific illumination level and moderate C-E voltage bias, the collector current density is independent (or very weakly dependent) on the thickness of base region. This is a highly desirable characteristic for the applications requiring very low absorption loss. A DHPT with a quantum-well like structure in the NIR region with a very thin base region can be integrated into a compact system operating over a broad wavelength range from 800nm to 2500nm.

### 3.4 SUMMARY

In this chapter, a linear photodetector (AlGaAs/GaAs/AlGaAs p-i-n photodiode) and a nonlinear photodetector (InP/InGaAs/InAlAs npn DHPT) were theoretically and experimentally investigated. Based on the analysis and characterization of device performance, they are suitable for various applications in the fields of optical communications and sensing technology. Specifically, both of them will be utilized and compared in the standing-wave Fourier-transform spectrometer system in the next chapter.

### References:

1. S. L. Chuang, "Physics of optoelectronic devices", John Wiley & Sons, Inc. 1995
2. M. Shur, "Physics of semiconductor devices", Prentice-Hall, Inc. 1990

3. C. C. Lin, W. Martin, J. S. Harris, Jr., "Optical gain and collector current characteristics of resonant-cavity phototransistors", *Appl. Phys. Lett.*, 76 (9) 1188-1190, 2000
4. N. Chand, P. A. Houston, P. N. Robson, "Gain of a heterojunction bipolar phototransistor", *IEEE Trans. Electron. Devices*, 32 (3) 622-627, 1985
5. S. M. Frimel, K. P. Roenker, "A thermionic-field-diffusion model for Npn bipolar heterojunction phototransistor", *J. Appl. Phys.*, 82 (3) 1427-1437, 1997
6. A very good website with various semiconductor material property parameters collection, <http://www.ioffe.rssi.ru/SVA/NSM/Semicond/>
7. S. Bhalotra, "Adaptive optical micro-spectrometers and spectral-selective sensing", PhD dissertation, Stanford University 2004
8. J. C. Campbell, A. G. Dentai, C. A. Burrus, J. F. Ferguson, "InP/InGaAs heterojunction phototransistor", *IEEE J. Quantum. Electron.*, 17 (2) 264-269, 1981
9. J. C. Campbell, K. Ogawa, "Heterojunction phototransistor for long-wavelength optical receivers", *J. Appl. Phys.*, 53 (2) 1203-1208, 1982
10. S. Chandrasekhar, M. K. Hoppe, A. G. Dentai, C. H. Joyner, G. J. Qua, "Demonstration of enhanced performance of an InP/InGaAs heterojunction phototransistor with a base terminal", *IEEE Electron. Device Lett.*, 12 (10) 550-552, 1991
11. Y. Miyamoto, J. Yoshinaga, H. Toda, T. Arai, H. Hongo, T. Hattori, A. Kokubo, K. Furuya, "Sub-micron GaInAs/InP hot electron transistors by EBL process and size dependence of current gain", *Solid-State Electron.*, 42 (7-8) 1467-70, 1998
12. P. Mazumder, S. Kulkarni, M. Bhattacharya, J. P. Sun, G. I. Haddad, "Digital circuit applications of resonant tunneling devices", *Proc. IEEE*, 86 (4) 664-86, 1998
13. H. Gorobkin, S. Tehrani, T. Rimmel, P. L. Fejes, K. J. Johnson, "Ohmic contact penetration and encroachment in GaAs/AlGaAs and GaAs FETs", *IEEE Trans. Electron Devices*, 36 (2) 281-288, 1989
14. J. Fu, J. S. Harris, Jr., "InP-based DHPT with graded E-B and B-C junctions", *Proc. SPIE*, 5726, 19-26, 2005
15. P. Bhattacharya, "Properties of lattice-matched and strained InGaAs", *INSPEC*, 1993

## CHAPTER 4 STANDING-WAVE FOURIER-TRANSFORM INTERFEROMETER

As described in chapter 1, FTIR is one of the most important multiplex spectrometer systems for detecting photons with different wavelengths simultaneously [1]. Much effort has been put in realizing compact FTIR [2], and the solution of standing-wave Fourier transform spectrometer (interferometer) (SWFTIR) by integrating silicon MEMS mirror and thin-film photodetectors was recently realized with good system performance [3-5]. This chapter will propose and realize a new technique utilizing harmonic Fourier spectra created by the non-linear properties of a HPT to improve the system resolution.

### 4.1 Fourier transform and harmonic spectra components

Fourier transform theory was proposed by Jean B. Joseph Fourier in 1822 and has been applied to many fields, such as signal processing. It has become a very powerful technique for spectrum analysis. For a periodic signal,  $f(t)$ , with a period of  $T$  in the time domain and angle frequency,  $\omega_0 = \frac{2\pi}{T}$ , it can be described by a Fourier series in Eq. (4-1),

$$f(t) = \frac{1}{2}a_0 + \sum_{k=1}^{\infty} (a_k \cos k\omega_0 t + b_k \sin k\omega_0 t) \quad (4-1)$$

$$a_k = \frac{2}{T} \int_{-T/2}^{T/2} f(t) \cos k\omega_0 t dt, b_k = \frac{2}{T} \int_{-T/2}^{T/2} f(t) \sin k\omega_0 t dt$$

The general form of the Fourier transform between  $f(t)$  and  $F(\omega)$  in the time and frequency domains, respectively, can be described in Eq. (4-2),

$$F(\omega) = \frac{1}{2\pi} \int_{-\infty}^{\infty} f(t) e^{-j\omega t} dt \quad (4-2)$$

For an ideal sinusoidal signal with frequency  $\omega_0$ , the Fourier spectrum will be a  $\delta$ -function (infinite magnitude and infinitesimal width) at  $\omega_0$  and  $-\omega_0$ . In reality the signal

cannot extend infinitely in the time domain and sampling an ideal sinusoidal signal by a time window results in a change of the Fourier spectrum. The Fourier transform will be the convolution of the ideal sinusoidal spectrum and a *sinc*-function (Fourier transform of a square sampling window). When the signals are distorted from an ideal sinusoid, higher order (harmonic) spectral components will appear. Fig. 4-1 shows that periodic square waves and symmetrical triangle waves only have odd-number harmonic components while asymmetrical triangle waves have all orders of harmonic components. The Fourier spectrum of sampling a distorted sinusoidal signal will include *sinc*-function at high-order harmonic components with the same linewidth determined by the width of the sampling window.

Let us consider two scenarios sampling a light wave by a partially transparent linear detector: (1) for a traveling wave  $E \sim E_0 e^{-j(\omega t - kz)}$ , the detector signal is constant,  $I \sim I_0 |e^{-j(\omega t - kz)}|^2 = I_0$ ; (2) for superposition of incident and reflected light waves with same frequency,  $E \sim E_0 (e^{-j(\omega t - kz)} + e^{-j(\omega t + kz)})$ , an immovable sinusoidal interference intensity pattern of the light fields (“interferogram”) can be sampled by the detector,  $I \sim I_0 |e^{-j(\omega t - kz)} + e^{-j(\omega t + kz)}|^2 = \frac{1}{2} I_0 (1 + \cos 2kz)$ . Two such immovable sinusoidal (or distorted versions for nonlinear detector) interference patterns with different frequencies ( $\omega_0$  and  $\omega_0 + \Delta\omega$ ) and fixed phase (“coherent”) will form an immovable interference pattern. The resolution of the system aiming to distinguish them depends on the extension range of the interference pattern defined by the sampling window width,  $\Delta L$ . For sinusoidal waves, the resolution needed to distinguish the two waves is  $0.6/\Delta L$  (compared with the full width half maximum FWHM width of *sinc* function as  $1.2/\Delta L$ ), which means that the spectrum will be clear enough to identify each frequency only if the frequency difference  $\Delta\omega > 0.6/\Delta L$  (as shown in Fig. 4-2). As mentioned above, the Fourier spectrum of distorted sinusoidal waves has higher order harmonic components with the same FWHM width of  $1.2/\Delta L$ . Since the frequency difference of the  $n$ th order harmonic component is  $n\Delta\omega$ , the resolution of the system need only satisfy  $n\Delta\omega > 0.6/\Delta L$ , with  $n$  times resolution improvement, although decreasing the signal level as shown in Fig. 4-3.

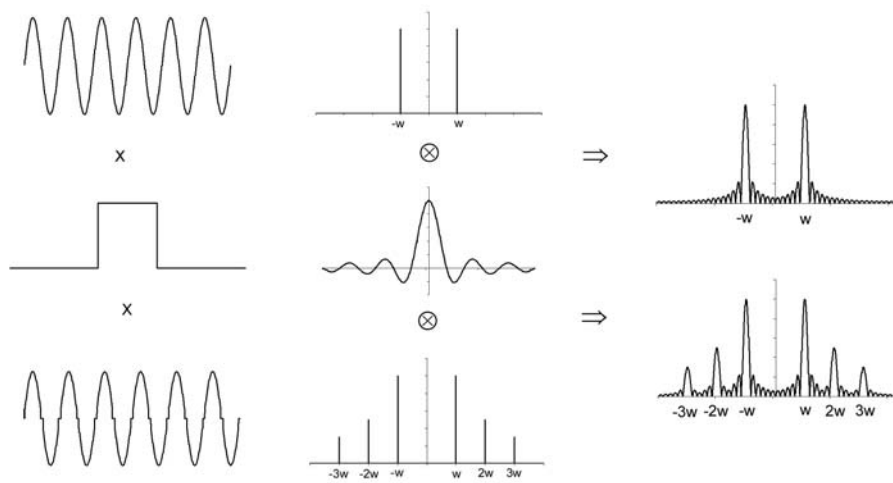
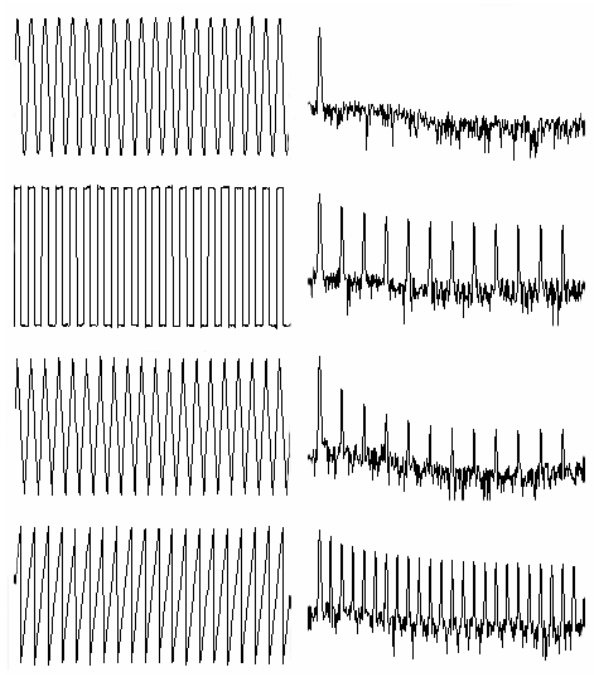


**Figure 4-1: Fourier transform of periodic signals (top), sampling sinusoidal and distorted signals with a square window (bottom).**

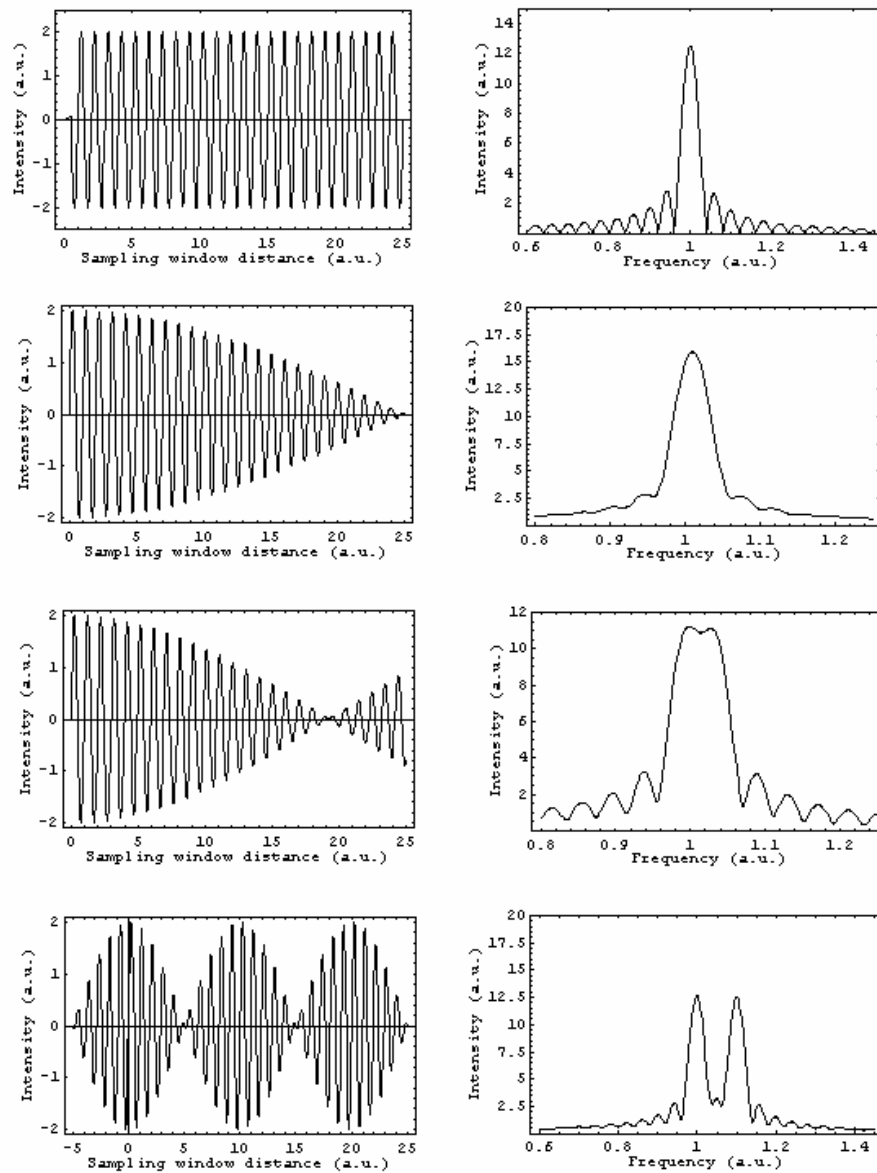


**Figure 4-2:** In order to distinguish two waves with different frequencies by sampling with a fixed window width: (from top to bottom) single sinusoidal wave with normalized frequency 1, two sinusoidal waves with frequencies 1 and 1.02, two sinusoidal waves with frequencies 1 and 1.025, two sinusoidal waves with frequencies 1 and 1.1. The sampling window has a fixed width of  $\Delta L = 25$ ,  $0.6/\Delta L = 0.024$ .

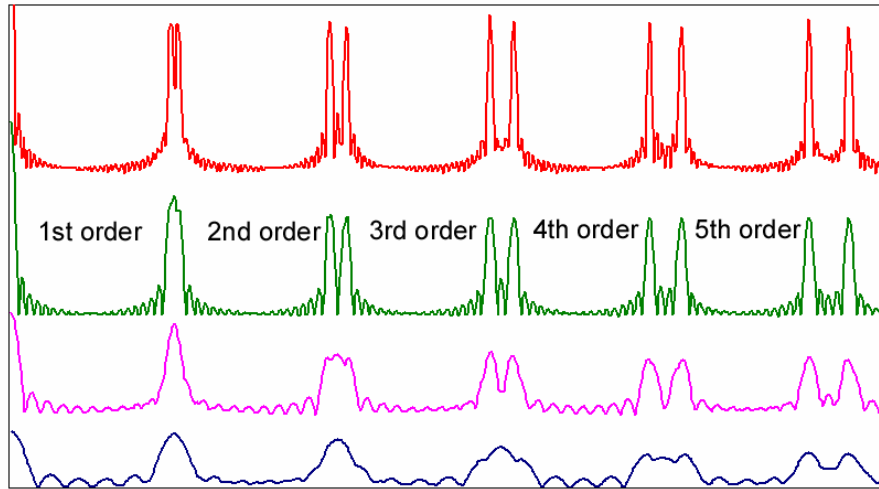


**Figure 4-3: Harmonic components in Fourier spectrum up to 5<sup>th</sup> order.**

There is another degree of freedom for the analysis of waves at multiple frequencies, relative phase difference. The interference pattern in a specific sampling window is dependent on the phase differences. A Mathematica model Eq. (4-3) shows the Fourier transform using normalized frequency, a relative frequency difference ratio,  $x$ , and a phase difference,  $\varphi$

$$F(\omega) = \frac{1}{2\pi} \int_0^{\Delta L} e^{-j\omega t} [\sin 2\pi \cdot t + \sin(2\pi \cdot x \cdot t + \varphi)] dt \quad (4-3)$$

As shown in Fig. 4-4, adjusting the phase difference between two waves will move the interference pattern in the sampling window. With the incorporation of an envelope node (at the center of the sampling window of the figure bottom), the Fourier transform is able to distinguish the two frequency components. The peak separation in the spectrum is related to both phase and frequency differences. If the envelope node of the interference patterns moves exactly to the central sampling window with a specific phase term, the peak separation is  $1/\Delta L + \Delta k$ , with  $\Delta L$  the sampling window width and  $\Delta k$  the frequency difference.

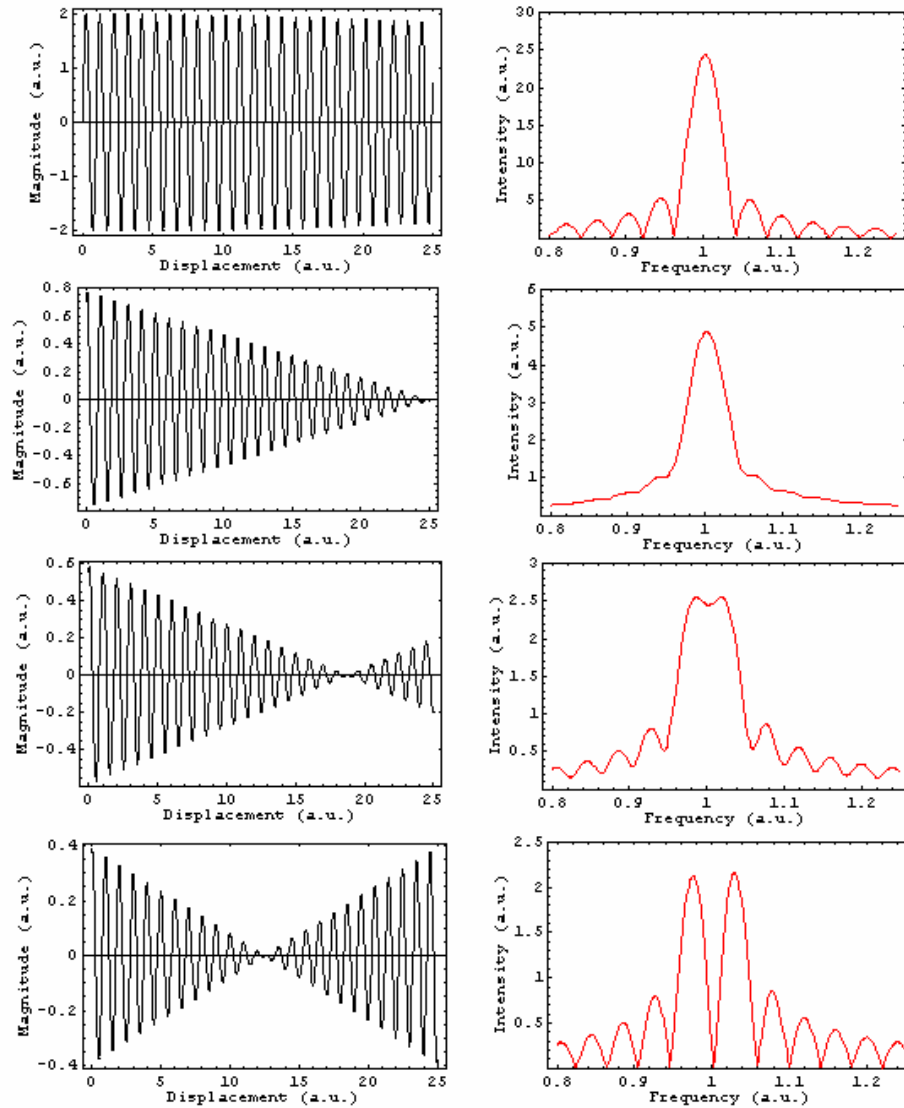
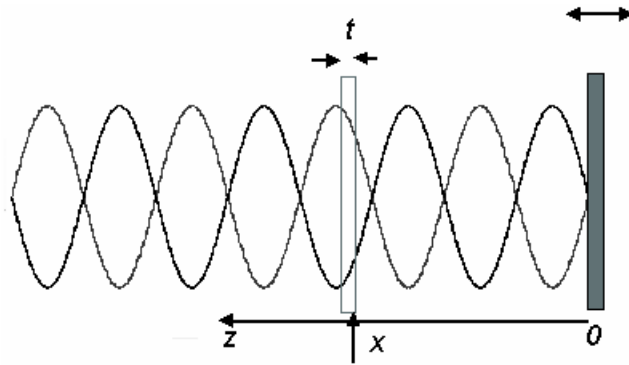


Figure 4-4: Waveforms and Fourier spectra of two ideal sinusoidal waves with different frequencies normalized to 1 and 1.005 with sampling window width of  $\Delta L=25$ , (from top to bottom) a phase difference  $\varphi=0, 3\pi/4, 13\pi/16$ , and  $7\pi/8$ . The frequency difference of the two waves is 0.005,  $\ll 0.6/\Delta L=0.024$ . The improvement of the resolution of the system is at the cost of signal magnitude, and the peak difference in the bottom spectrum equals to  $1/\Delta L+\Delta k$  with all the peak FWHM width of  $1/\Delta L$ .

## 4.2 Standing wave FTIR design

A standing wave may be formed by the forward light and backward light within a distance less than the coherent length of the incident light sources. Since the distance between the detector and the scan mirror cannot be reduced beyond limits set by the processing technology and the operating conditions, the standing-wave FTIR should be targeted to be a spectrometer for distinguishing highly coherent light sources.



**Figure 4-5: Scheme of a standing-wave transform spectrometer, the intensity of the standing-wave light field being sampled by a thin partially transparent detector.**

### 4.2.1 Optical model

The wave function of the standing wave formed by the incident waves and reflected waves can be described in Eq. (4-1),

$$E = E_0 e^{j\omega t}, \quad k = \frac{2\pi}{\lambda}, \quad \omega = 2\pi\nu, \quad \nu = \frac{c}{\lambda} \quad (4-1)$$

where  $k$ ,  $\omega$ ,  $\lambda$ ,  $\nu$  have normal meanings, wavenumber, angular frequency, wavelength and frequency, respectively, and the magnitude is position dependent in Eq. (4-2) (with the origin at the mirror surface, as shown in Fig. 4-5, the reflection at a highly conductive mirror surface introduces an extra phase shift of  $\pi$ ) [3],

$$E_0(z) = E_{f0} e^{-jkz} + E_{b0} e^{jkz} \quad (4-2)$$

where  $E_{f0}$  and  $E_{b0}$  are forward and backward components of the light waves, both being complex. The intensity of the standing wave can be described by Eq. (4-3),

$$I(z) = |E_0^2| = |E_{f0}^2| + |E_{b0}^2| + E_{f0}^* E_{b0} e^{j2kz} + E_{f0} E_{b0}^* e^{-j2kz} \quad (4-3)$$

where the last two terms in Eq. (4-3) represent the interference between the forward and backward light waves. The absorption of photons in the detector active region can be described by Eq. (4-4),

$$\frac{dP_{opt}}{dx} = -\alpha P_{opt}$$

$$g_{opt} = -\frac{1}{A} \frac{dP_{opt}}{dx} \frac{1}{h\nu} \quad (4-4)$$

where  $P_{opt}$  is the power of incident light,  $\alpha$  the absorption coefficient of detector active region materials,  $g_{opt}$  the generation rate of carriers upon illumination,  $A$  the area of the detector active region,  $h$  Plank constant and  $\nu$  frequency of the incident photons. The photocurrent from the detector in the standing wave light field can be determined by Eq. (4-5),

$$i_{det}(x) = C_0 \cdot \int_x^{x+t} (1 + e^{-\alpha z} + 2e^{-\alpha z/2} \cos kz) e^{-\alpha(z-x)} dz$$

$$= C_0 \cdot \left\{ (1 + e^{-\alpha x}) \int_x^{x+t} e^{-\alpha(z-x)} dz + 2e^{-\alpha x/2} \int_x^{x+t} \frac{e^{jkz} + e^{-jkz}}{2} \cdot e^{-\alpha(z-x)} dz \right\}$$

$$= C_0 \cdot \left\{ \frac{1}{\alpha} (1 - e^{-2\alpha t}) + 2e^{-\alpha x/2} \cdot \sqrt{\frac{1 + e^{-2\alpha t} - 2e^{-\alpha t} \cos kt}{\alpha^2 + k^2}} \cdot \sin(kx + \varphi) \right\} \quad (4-5)$$

where  $C_0$  is a constant incorporating the incident light power and other system related parameters,  $t$  the thickness of detector active region,  $x$  the detector position shown in Fig.

4-5, other parameters having the normal previous meanings and the extra phase term for

simplicity  $\varphi$  is: 
$$\cos \varphi = \frac{ke^{-\alpha t} \cos kt + \alpha e^{-\alpha t} \sin kt - k}{\sqrt{\alpha^2 + k^2} \cdot \sqrt{1 + e^{-2\alpha t} - 2e^{-\alpha t} \cos kt}}$$

#### 4.2.2 Detector absorption region thickness

The last term in Eq. (4-5) is the interference of forward and backward light wave components. The system sensitivity (*SEN*) and contrast (*CON*) can be defined in Eq. (4-6) considering the different light field intensity components,

$$I_{tot} = I_{con} + I_{speckle}$$

$$SEN = I_{con} + |I_{speckle}|$$

$$CON = \frac{2 \cdot |I_{speckle}|}{I_{inc}} \tag{4-6}$$

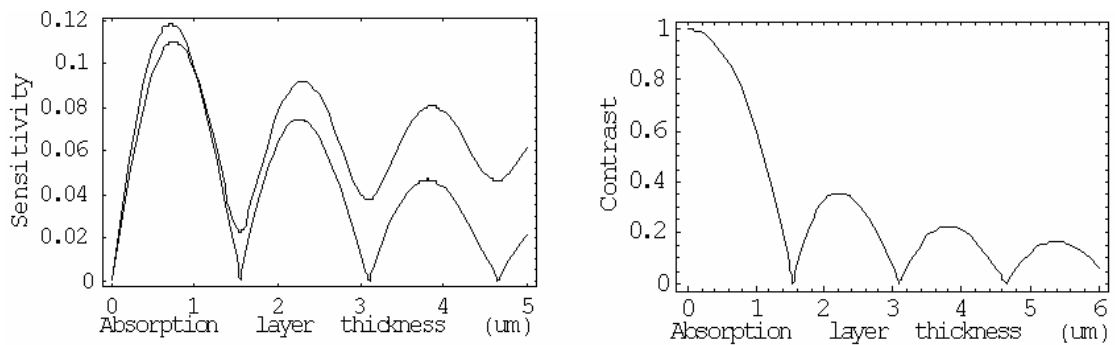


**Figure 4-6: The dependence of sensitivity and contrast on the absorption layer thickness for a linear photodetector, shown in the left diagram is the precise model and rough model without considering the power loss in the absorption region.**

### 4.2.3 Tolerance analysis

The interference pattern contrast is dependent on the system parameters (as shown in Fig. 4-7), including both the absorption region thickness and tilt deviating from a perfectly perpendicular plane in the standing waves.

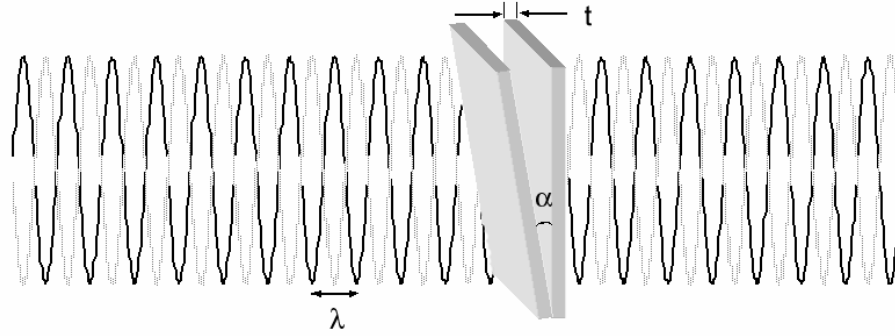


**Figure 4-7: Influence of detector tilting on the signal contrast.**

$$\begin{aligned}
 i_{\text{det}}(x) &\propto \int_0^D \int_x^{x + \frac{t}{\cos \theta}} (1 + \cos k(z + y \sin \theta)) dz dy \\
 &= \int_0^D \left[ z + \frac{1}{k} \sin k(z + y \sin \theta) \right]_x^{x + \frac{t}{\cos \theta}} dy \\
 &= \frac{tD}{\cos \theta} + \frac{\lambda^2}{\pi^2 \sin \theta} \sin(kD \sin \theta / 2) \sin\left(\frac{kt \cos \theta}{2}\right) \sin k\left(x + D \frac{\sin \theta}{2} + \frac{t}{2 \cos \theta}\right) \quad (4-7)
 \end{aligned}$$

The dependence of contrast on the detector tilt angle is shown in Fig. 4-8, where the best contrast can be achieved only within a range of tilting angle of no more than 6 arcsec. For discrete components system, such optical path alignment is not a trivial job! However, for a compact standing wave transform spectrometer with integrated thin-film photodetector fabricated by silicon micro-electric-mechanical-system (MEMS) technology [4, 5], the system alignment is guaranteed by the selective etching of precisely defined crystallographic planes in the fabrication processes.

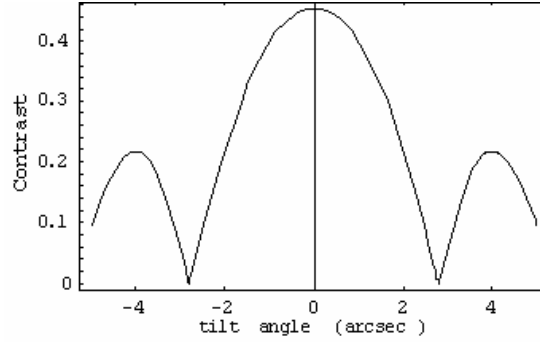


Figure 4-8: Dependence of the interference pattern contrast on the detector tilt angle.

#### 4.2.4 Fabry-Perot effect

The previous discussion ignored all surface reflections except from the scanning mirror surface. If we include light reflection at the outer surface of the detector (the surface incident light beams first reach), the detector will then be effectively located in a Fabry-Perot cavity defined by the scan mirror and detector outer surface as shown in Fig. 4-9.

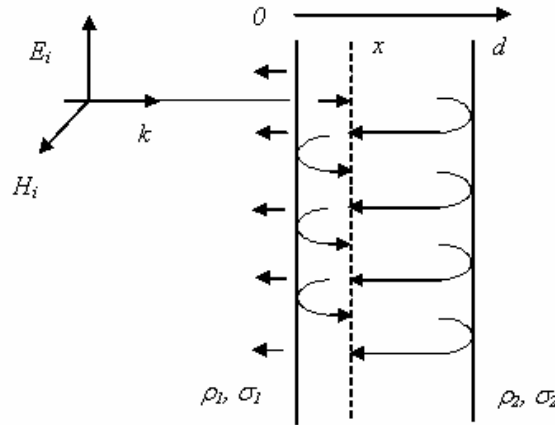


Figure 4-9: Fabry-Perot cavity formation, dash line corresponds to the detector absorption region,  $\rho$ ,  $\sigma$  the amplitude reflection and transmission of each mirror,  $\rho^2=R$  and  $\sigma^2=T$ .

The amplitude at the detector absorption plane ( $x$ ) can be expressed in Eq. (4-8),

$$E(x) = \sigma_1 E_i e^{-jkx} + \sigma_1 \rho_2 E_i e^{-jkd} e^{-jk(d-x)} + \sigma_1 \rho_1 \rho_2 E_i e^{-jk2d} e^{-jkx} + \sigma_1 \rho_1 \rho_2^2 E_i e^{-jk3d} e^{-jk(d-x)}$$

$$+ \dots + \sigma_1 (\rho_1 \rho_2)^n E_i e^{-jk2nd} e^{-jkx} + \sigma_1 \rho_2 (\rho_1 \rho_2)^n E_i e^{-jk(2n+1)d} e^{-jk(d-x)} \quad (4-8)$$

which can be easily summed in Eq. (4-9),

$$E(x) = \frac{\sigma_1 E_i e^{jkx}}{1 - \rho_1 \rho_2 e^{-j2kd}} \left[ e^{-j2kx} + \rho_2 e^{-j2kd} \right] \quad (4-9)$$

It is thus easy to measure the light intensity at the detector absorption plane,

$$I(x) = I_i \cdot \frac{\sigma_1^2}{(1 - \rho_1 \rho_2)^2 + 4\rho_1 \rho_2 \sin^2 2kd} \left[ 1 + \rho_2^2 + 2\rho_2 \cos 2k(x - d) \right] \quad (4-10)$$

If the detector surface is coated with a perfect anti-reflection (AR) coating,  $\sigma_1 = 1$ ,  $\rho_1 = 0$ , there is no Fabry-Perot cavity formed and Eq. (4-10) will be simplified to Eq. (4-5). For the parameters in our system, reflection on the InP (or InGaAs, InAlAs) is about 50%,  $\sigma_1 = 0.71$ ,  $\rho_1 = 0.71$ ,  $\sigma_2 = 0$ ,  $\rho_2 = 1$ ,  $x = 400\mu\text{m}$ ,  $\lambda = 1550\text{nm}$ , the light intensity at the detector absorption region versus the mirror displacement is shown in Fig. 4-10. It is not surprising to find the resonances in the light intensity as the mirror scans across specific positions. These resonances also effectively contribute to the generation of high-order Fourier-components in the detector response, even with a linear detector.

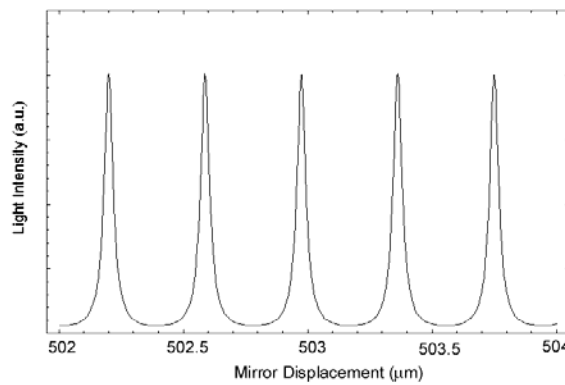


**Figure 4-10: Light intensity at the detector absorption region versus the mirror position.**

### 4.3 SWFTIR setup

The SWFTIR setup has only two major components, one partially transparent photo-detector and one scan mirror (silicon MEMS mirror or a PZT-controlled mirror). The incident light comes from a fiber port output of a 3dB in-line fiber combiner (Oplink Model # SWFC 5250P002214), which combines coherent light sources from a tunable laser (1500-1580nm) and three different laser diodes (“1” MQW-DFB Excelight 1546nm  $I_{th}=10\text{mA}$ , “2” PL15B002FC11-S-0 Pdl 1549nm, and “3” PL13B002FC11-S-0 Pdl 1312nm) for the demonstration of spectral resolution.

The partially transparent thin-film photodetector is a double hetero-junction InP/InGaAs/InAlAs bipolar phototransistor (DHPT) with an emitter-up mesa structure. The DHPT detector is operated in its nonlinear region to distort the sinusoidal light field intensity of the standing wave in order to utilize the Fourier transform harmonic components analysis introduced in the previous section in this chapter. The bias voltage across the emitter and collector was kept at 2.5V and the base was floating. The emitter surface and mesa walls were passivated by PECVD (plasma-enhanced chemical vapor deposition) deposited SiN, which prevents oxidation and degradation of indium based semiconductor materials exposed to air. If the thickness of the SiN passivation layer was precisely controlled to be one quarter of the central wavelength of the incident coherent light sources, the SiN layer could act as an AR coating. The DHPT was wire-bonded on a custom-made butterfly 24-pin electronic package with open transmission window on the backside. Fig. 4-11 shows the photo-current output of the DHPT after conversion to a voltage signal by measuring the voltage across a resistor between the emitter and ground. In the spectrometer setup, the DHPT was illuminated from the back (collector side) by the collimated incident light beams. The emitter is closer to the mirror side, and correspondingly the back-reflected light from the scan mirror illuminated the DHPT from the front (emitter side) and hence higher effective optical gain. Thus the loss of light intensity by the absorption in the base region is compensated by the higher HPT gain for light reflected from the mirror surface. In addition, reflections at the interfaces between different materials were reduced to the minimum degree.

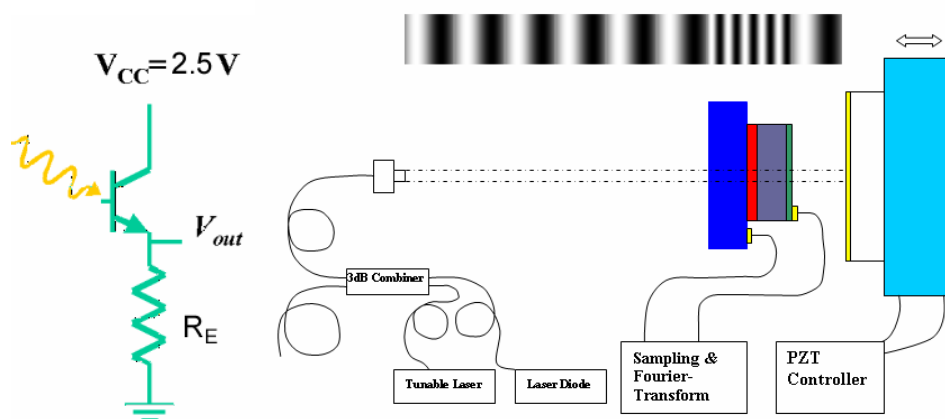


**Figure 4-11: The scheme of standing-wave Fourier-transform spectrometer, shown light field intensity does not consider the refractive difference of InP, InGaAs and InAlAs, and the DHPT circuit shows the floating base and sampling of  $R_E$ .**

The gold-coated highly reflective mirror was mounted on a lead zirconium titanate (PZT) piezoelectric controlled stage. Both the packaged DHPT and PZT-controlled scan mirror were mounted on high-precision optical mirror mounts (*New Focus 9807*) with a tilting resolution of  $107 \mu\text{rad}$  (22arcsec) per  $5^\circ$  screw rotation. The PZT stage (*Piezosystem jena PZ38SG*) has a feedback loop controlled scan range of  $32\mu\text{m}$  (z direction) with a control voltage of 10V (internal operating voltage 100V), and a free scan range up to  $42.8\mu\text{m}$  with an operating voltage of 150V. The relationship between the displacement and voltage control was calibrated by the vendor as well as the hysteresis protocol and linearity (Appendix B).

The modulation control voltage to the PZT stage was produced by a function signal generator and a symmetrical triangle wave was used. The Fourier-transform of the interference patterns was performed in-situ using a PC-controlled oscilloscope. The influence of the nonlinearity of the DHPT on the interference pattern is shown in Fig. 4-12, illustrating the distortion of a sinusoidal waveform. Based on the analysis of the F-P cavity set by the scan mirror and detector surfaces in Eq. (4-10) and Fig. 4-10, we can see that the nonlinear property is actually a combination of the F-P mode and nonlinear DHPT detector.

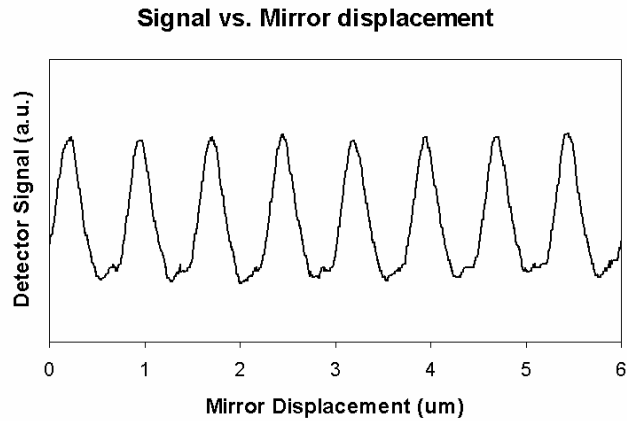


**Figure 4-12: Interference pattern from the DHPT with the scan mirror displacement, the coherent light source is a tunable laser with wavelength of 1500nm and output power of 1mW.**

#### 4.4 Optical measurements

A SWFTIR based on a linear thin-film photodiode detector (silicon and AlGaAs/GaAs) and silicon-MEMS-mirror was characterized in references [4-7]. The system resolution was dependent on the free scan length of the MEMS mirror and was estimated from the FWHM width of the spectrum peaks. The MEMS mirror scan length was  $\Delta L=52.6\mu\text{m}$ , and the peak FWHM peak was 4.3nm for an incident laser source  $\lambda=633\text{nm}$  and 7.5nm for a laser source  $\lambda=866\text{nm}$ , both of which were close to the theoretical value of  $0.6/\Delta L =96\text{ cm}^{-1}$ . In the following section, we will use the HPT detector and harmonic spectrum technique to improve the spectrometer resolution beyond this  $0.6/\Delta L$  limit.

##### 4.4.1 Single frequency light source

Fig. 4-11 shows the waveform of the interference pattern from the DHPT sampling the standing wave formed by a single frequency laser (1500nm, 1mW, linewidth less than 2GHz). Due to the Fabry-Perot effects and the nonlinearity of the operating mode of the DHPT, the Fourier spectrum of the interference pattern shows high order harmonic components with wavenumbers of  $6667\text{cm}^{-1}$  (1<sup>st</sup> order),  $13334\text{cm}^{-1}$  (2<sup>nd</sup> order),  $20000\text{cm}^{-1}$  (3<sup>rd</sup> order), and  $26668\text{cm}^{-1}$  (4<sup>th</sup> order).

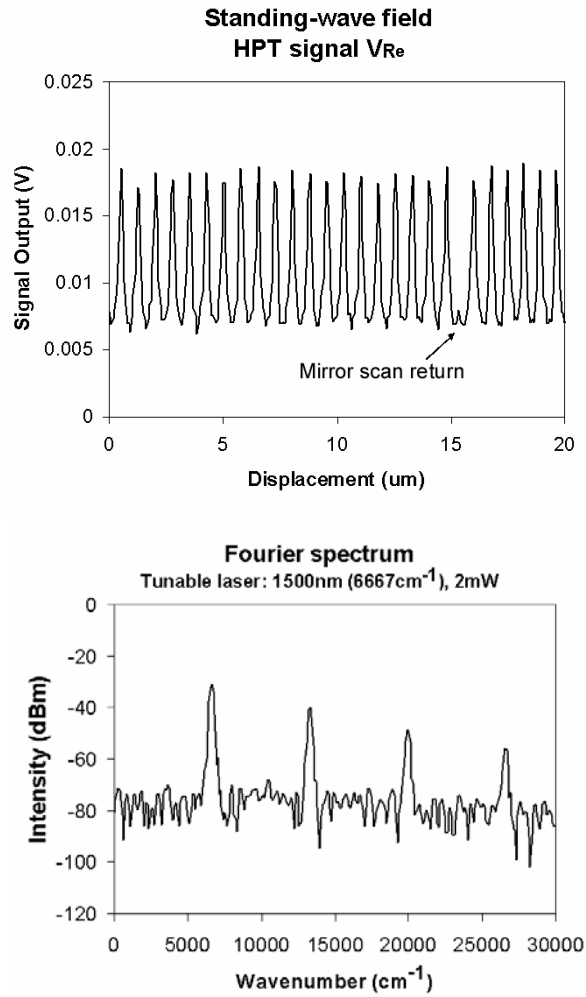


**Figure 4-13: Waveform and Fourier spectra of a single wavelength laser source. The bottom figure shows the four harmonic components with wavenumbers: 6667cm<sup>-1</sup> (1<sup>st</sup> order), 13334cm<sup>-1</sup>(2<sup>nd</sup> order), 20000cm<sup>-1</sup>(3<sup>rd</sup> order), and 26668cm<sup>-1</sup>(4<sup>th</sup> order).**

Calibration of the SWFTIR system can be done independently by two methods: one is to use the pre-calibration data of the PZT-stage, the other is to use a reference light source with a precisely known frequency. Most of the systematic error comes from scanning the PZT-controlled mirror because of small nonlinearity and hysteresis effects. The second method is important for identification of multiple wavelength light sources and will be discussed in the next section. From the calibration data from the vendor, the sensitivity of the PZT (PZ38SG) is  $\eta_{PZT} = 0.3097\text{V}/\mu\text{m}$ , the modulation signal of the PZT control is  $\nu_{mod}$  (on the order of 1V/s), the wavelength of the light sources can be calculated from the interference patterns and Fourier spectrum by Eq. (4-8),

$$\lambda = \frac{2}{p \cdot f_n} = \frac{2 \cdot v_{PZT}}{f_n} = \frac{2 \cdot v_{mod}}{f_n \cdot \eta_{PZT}} \quad (4-8)$$

where  $f_n$  is the Fourier spectrum peak position collected from the PC-controlled oscilloscope. The calculation results from the raw Fourier spectrum data shows the wavelength of the light source as  $\lambda = \frac{2 \cdot 10V / 500ms}{86.91Hz \cdot 0.3097V / \mu m} = 1486nm$ , comparing to the known wavelength 1500nm, the difference being ~1%, which is within the PZT scan error range.

#### 4.4.2 Multiple wavelength light sources

Compared to the absolute frequency of the light sources, the frequency difference of multiple wavelength light sources is of more interest for coherent photodetection. Fig. 4-12 shows the waveforms and Fourier spectra of the interference pattern from the DHPT in the SWFTIR system distinguishing light sources of two frequencies, one from the tunable laser at 1500nm, another from laser diode 3 (1312nm, noted as “1300nm” in the figure for simplicity). The peaks in the spectra are identified as two groups, one from the tunable laser and the other from the laser diode 3. The frequency of the tunable laser was taken as a calibration reference to calculate the frequency of the peaks in the other group. The error between the calculation result ( $1/7600cm^{-1}=1316nm$ ) is very close to the OSA measured wavelength of 1312nm.

Based on the harmonic Fourier spectrum analysis in section 4-1, the resolution of the SWFTIR for a mirror scan length of  $\Delta L=32\mu m$  would be:  $0.6/\Delta L=187.5cm^{-1}$  at the 1<sup>st</sup> order fundamental,  $0.6/(2\Delta L)=93.8cm^{-1}$  at the 2<sup>nd</sup> order harmonic,  $0.6/(3\Delta L)=62.5cm^{-1}$  at the 3<sup>rd</sup> order harmonic,  $0.6/(4\Delta L)=46.9cm^{-1}$  at the 4<sup>th</sup> order harmonic, and  $0.6/(5\Delta L)=37.5cm^{-1}$  at the 5<sup>th</sup> order harmonic. In order to verify the resolution analysis, the SWFTIR system was used to distinguish the combined light sources of laser diode 2 (MQW-DFB 1546nm,  $6468cm^{-1}$ ) and the tunable laser (1500-1580nm,  $6329-6667cm^{-1}$ ). As shown in Fig. 4-13, Fourier spectra for the multiple coherent light sources demonstrate the resolution at different harmonic orders.

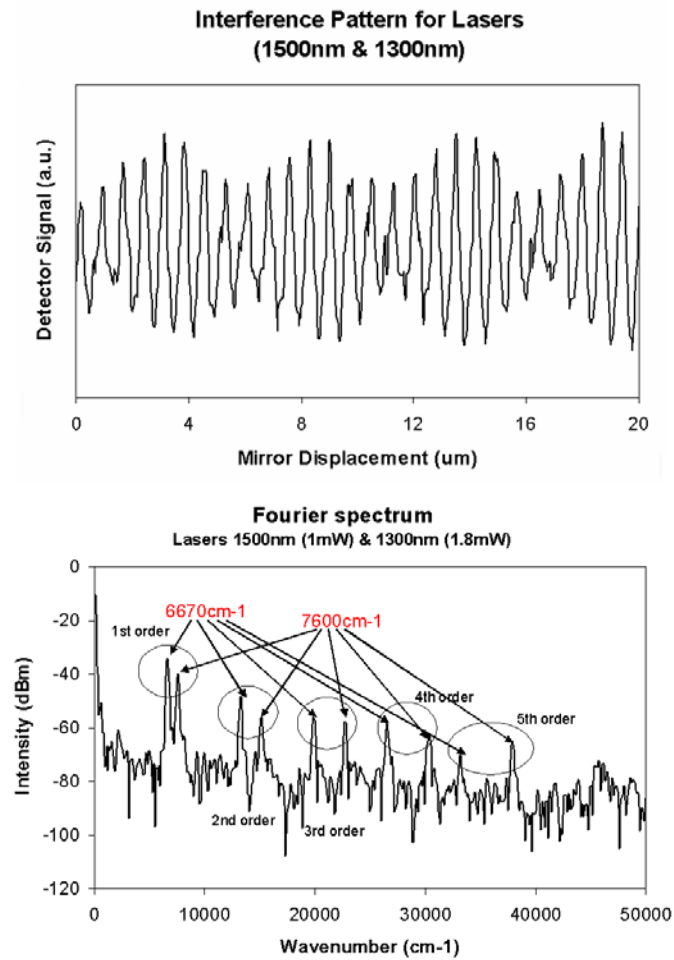


**Figure 4-14: Waveform and Fourier spectrum of the interference pattern for light sources with two frequencies ( $6670\text{cm}^{-1}$  taken as reference,  $7600\text{cm}^{-1}$  calculated from the calibration data).**

The frequency of laser 2 ( $1546\text{nm}$ ,  $6468\text{cm}^{-1}$ ) was taken as reference to calibrate the measurement results, the three frequencies calculated in Fig. 4-13 were  $6610\text{ cm}^{-1}$ ,  $6562\text{ cm}^{-1}$ , and  $6535\text{ cm}^{-1}$ , respectively. Compared with the set points of the tunable laser ( $1500\text{nm}$ ,  $1520\text{nm}$  and  $1535\text{nm}$ , correspondingly  $6667\text{ cm}^{-1}$ ,  $6579\text{ cm}^{-1}$ , and  $6515\text{ cm}^{-1}$ ), the error range is less than 0.5%.

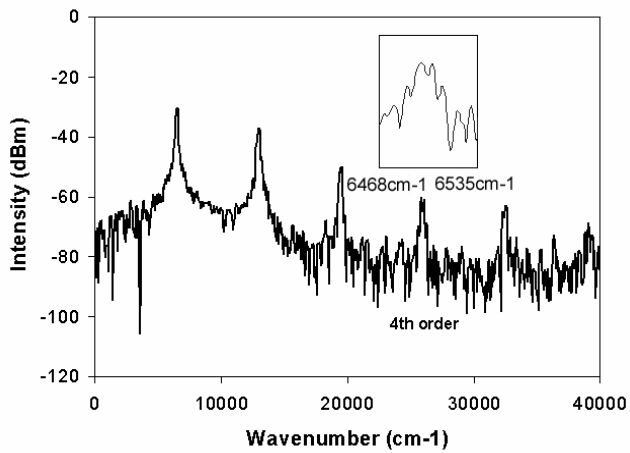
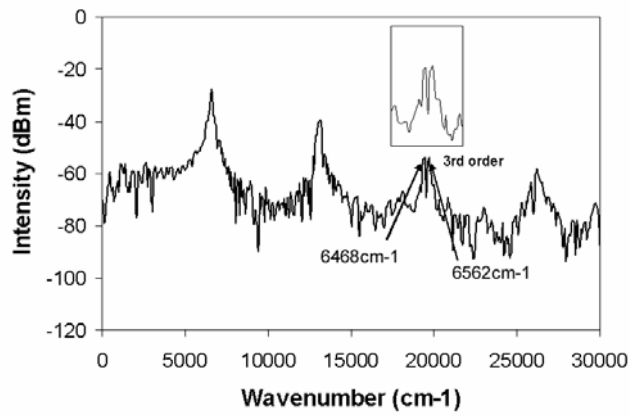
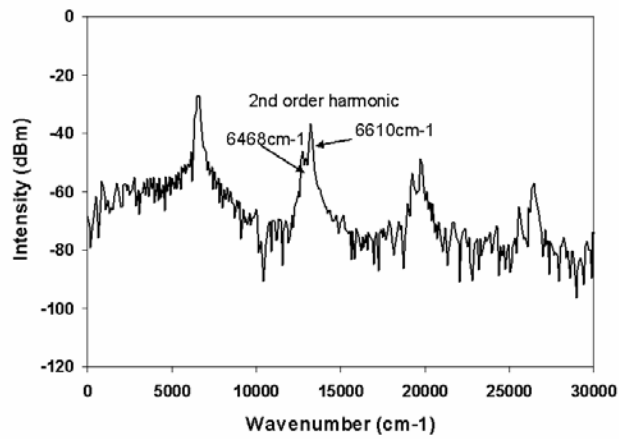


Figure 4-15: Fourier spectra for multiple wavelength coherent light sources: as the frequency difference was reduced from 50nm to 30nm and 15nm, the harmonic order at which one can distinguish the two frequencies changes from the 2<sup>nd</sup> order to 3<sup>rd</sup> and 4<sup>th</sup> order.

## 4.5 Summary

This chapter investigates theoretically and experimentally a compact standing-wave Fourier-transform spectrometer using the non-linear properties of a HPT detector and a new technique of harmonic spectrum component analysis to improve the system resolution. The demonstrated system shows a resolution  $37.5\text{cm}^{-1}$  for the 5<sup>th</sup> order harmonic spectrum component with a mirror scan range of  $32\mu\text{m}$  and should be achievable over a wide spectral range of 950-1700nm determined by the InGaAs-based DHPT detector. At the central wavelength of 1550nm, such a SWFTIR system utilizing the harmonic spectrum analysis technique has a system resolution of  $\mathcal{R} = \lambda/\Delta\lambda = 172$  and  $\Delta\lambda = 9\text{nm}$ . At the central wavelength of 633nm similar SWFTIR system with nonlinear Si-based thin-film detector utilizing same harmonic spectrum analysis has a system resolution of  $\mathcal{R} = \lambda/\Delta\lambda = 422$  and  $\Delta\lambda = 1.5\text{nm}$ . For future system resolution improvements, the available PZT (or MEMS mirror) scan range could be as long as 1.5mm, the harmonic spectral components could be selected out to 10<sup>th</sup> order, and thin-absorption-layer nonlinear photo-detectors (HPT) can be interchangeable within a broad range covering the whole near infrared region. Such SWFTIR array system could cover the entire NIR region with a resolution of  $1\text{cm}^{-1}$ .

The limitation of harmonic Fourier-spectrum analysis is the correlation of system spectral resolution and free spectral range (FSR). Aliasing effects in the harmonic spectral components limit the free spectral range of the system. For a signal with central wavenumber of  $k (=1/\lambda)$  and spectral range of  $\Delta k$ , at the  $n^{\text{th}}$  ( $n > 1$ ) harmonic order the free spectral range can be determined by  $(n-1) \cdot (k + \Delta k/2) = n \cdot (k - \Delta k/2)$ ,  $\Delta k = k/(n-1/2)$ ; when  $n=1$ ,  $\Delta k = 2k/3$ . On the other hand, the spectrum power at the  $n^{\text{th}}$  harmonic order is dependent on the spectra envelope shape determined by the sampling transfer function. For example, the central wavelength is 1500nm for the demonstrated system in this chapter, and the FSR at the 5<sup>th</sup> harmonic order is  $1481\text{cm}^{-1}$  ( $\sim 340\text{nm}$ ).

Let us make an interesting comparison between the traditional bulky FTIR systems and SWFTIR systems utilizing harmonic spectral analysis technique (H-SWFTIR) proposed in this chapter as a conclusion (shown in Table 4-1) [8].

**Table 4-1: Comparison between traditional FTIR and H-SWFTIR.**

	FTIR	H-SWFTIR
Dimension	0.1-1m	5cm (discrete components) 0.1-1mm (MEMS)
Resolution	Varies 0.01-10cm <sup>-1</sup>	1, 10-100cm <sup>-1</sup>
Price	\$10,000 for resolution 1cm <sup>-1</sup>	Cheap
Array capability	no	yes

**References:**

1. P. R. Griffiths, "Fourier transform infrared spectrometry", Science, New series, 222 (4621) 297-302, 1983
2. C. P. Bacon, Y. Mattley, R. DeFrece, "Miniature spectroscopic instrumentation: applications to biology and chemistry", Review of Scientific Instruments, 75 (1) 1-16, 2004, and a large amount of references therein.
3. D. A. B. Miller, "Laser tuners and wavelength-sensitive detector based on absorbers in standing-waves", IEEE J. Quantum. Electron. 30 (3) 732-749, 1994
4. H. L. Kung, "Miniaturized optical wavelength sensors", PhD dissertation, Stanford University, 2003
5. S. R. Bhalotra, "Adaptive optical micro-spectrometers and spectra-selective sensing" PhD dissertation, Stanford University, 2004
6. S. R. Bhalotra, H. L. Kung, J. X. Fu, N. C. Helman, O. Levi, D. A. B. Miller, J. S. Harris, Jr., IEEE Lasers and Electro-Optics Society 2002 Annual Meeting, Glasgow, Scotland (November 10-14, 2002). Paper ML5.
7. D. Knipp, H. Stiebig, S. R. Bhalotra, E. Bunte, H. L. Kung, D. A. B. Miller, "Silicon-based micro-Fourier spectrometer", IEEE Trans. Electron. Devices, 52 (3) 419-426, 2005
8. Commercial FTIR systems see: [http://www.jascoinc.com/products/s\\_ftir\\_raman.html](http://www.jascoinc.com/products/s_ftir_raman.html), resolution of a FTIR for gas analysis applications see: <http://www.irgas.com/Application%20Notes/IAN-05-05%20FTIR20Resolution.pdf>,

## CHAPTER 5 SUMMARY

SWFTIR systems utilizing harmonic spectral analysis technique have been demonstrated with improved resolution in near-infrared region for applications of coherent photodetection.

This dissertation has focused on three areas: InGaAs-based semiconductor materials systems investigated by SSMBE with active regions out to beyond  $2\mu\text{m}$ ; design, fabrication, and characterization of photodetectors in NIR region; implementation of a SWFTIR.

(1) High quality semiconductor material is essential to high-performance IR systems. MBE materials growth technique with optimized operating conditions is capable of achieving high quality semiconductor materials, including strain and defect free thin films lattice-matched to the substrate, highly strained pseudomorphic quantum structures, and relaxed low defect density device layers on metamorphic buffers.

(2) Thin-film photo-detectors are designed, fabricated and characterized. The difference in design criteria for HBT and HPT (especially for the applications in this dissertation) is identified. A group of detectors, including p-i-n photodiode detector, MSM photodetector and npn phototransistor, has been utilized in applications such as spectral shaping and spectrum identification.

(3) Based on the nonlinearity properties of Fabry-Perot cavity and phototransistor, Fourier-spectrum analysis technique using harmonic order spectral components is applied to the implementation of compact standing-wave transform interferometer (spectrometer). The system resolution is improved at high harmonic order spectral components with a reduced FSR. The demonstrated SWFTIR system has a resolution of  $37.5\text{cm}^{-1}$  with a FSR of  $340\text{nm}$ .

Future work related to this dissertation may include:

(1) We need to extend the applications of above InGaAs-based materials systems in the wavelength region of  $2\text{-}2.5\mu\text{m}$  for both NIR light sources and detection

devices. With further optimized MBE growth conditions, it may be possible to fabricate lasers (LED) using the low defect-density device layers on metamorphic buffers;

(2) We may be able to integrate the MEMS scan mirror (from bulk micromachining), or a tunable filter (surface micromachining), and the thin film detector (including linear and non-linear photo-detectors) to make a micro-interferometer with improved system resolution;

(3) We need investigate the influence of anti-reflective (AR) and high-reflective (HR) coating of the detector surfaces (both front and back sides) on system performances. For an AR-coating detector, no cavity is formed between the scan mirror and the light sources; for a HR-coating detector, a Fabry-Perot cavity is formed between the scan mirror surface and detector surface. We may further improve the system resolution without degrading the FSR aspect by introducing extra nonlinear property of the system;

(4) We may expand the applications of such coherent NIR system into hyper-spectral sensing, objects identification sensor and other fields which require array construction.

## **APPENDIX A: Fabrication process for a HPT (same as mesa photodiodes)**

### (1) Lithography:

Yield enhancement systems (YES) oven: standard program 30mins;

Laurel: using Shipley3612 photoresist, 3000rpm, 30s, resist-film layer  $\sim 1.6\mu\text{m}$  reached;

Karluss: after pre-bake  $90^\circ\text{C}$  for 30s, soft contact, exposure (C11,  $15\text{mW}/\text{cm}^2$ ) for 1.4s, post-bake  $115^\circ\text{C}$  for 1min;

Developer (LDD26W) for 2mins till exposed area clean, DI water rinse for 1min;

Hardening bake: at  $90^\circ\text{C}$  for 10mins.

### (2) Etching:

Dry etching (plasma quest) AlGaAs/GaAs, etch rate  $\sim 250\text{nm}/\text{min}$ :

Process pressure  $\sim 5\text{mTorr}$ ,  $\text{BCl}_3$   $\sim 50\text{sccm}$ ,  $\text{Cl}_2$   $\sim 7.4\text{sccm}$ , Ar  $\sim 75\text{sccm}$ , chuck T  $\sim 20^\circ\text{C}$ , backside He  $\sim 10\text{sccm}$ , ECR power  $\sim 400\text{W}$ , RF power  $\sim 50\text{W}$ .

Wet etching (varies due to temperature and humidity fluctuation):

$\text{H}_2\text{SO}_4:\text{H}_2\text{O}_2:\text{H}_2\text{O}$  (1:1:40) selective etching InAlAs/InGaAs over InP:  $\sim 250\text{nm}/\text{min}$ ;

$\text{H}_2\text{SO}_4:\text{H}_2\text{O}_2:\text{H}_2\text{O}$  (1:1:20) selective etching InAlAs/InGaAs over InP:  $\sim 450\text{nm}/\text{min}$ ;

$\text{H}_2\text{SO}_4:\text{H}_2\text{O}_2:\text{H}_2\text{O}$  (1:8:40) etching AlGaAs/GaAs:  $\sim 1.0\mu\text{m}/\text{min}$ ;

$\text{H}_3\text{PO}_4:\text{HCl}$  (9:1) etching InP:  $\sim 220\text{nm}/\text{min}$ ;

$\text{HCl}:\text{H}_2\text{SO}_4:\text{CH}_3\text{COOH}$  (1:1:2) etching InP:  $\sim 300\text{nm}/\text{min}$ .

### (3) PE-CVD (STS) and dry etching of standard $\text{SiN}_x$ :

Deposition rate  $\sim 77\text{A}/\text{s}$ : silane (2%)  $\sim 1143\text{sccm}$ , ammonia  $\sim 20\text{sccm}$ , RF power  $\sim 11\text{W}$ , high:low time ratio  $\sim 5:2$ , chamber pressure  $\sim 550\text{mTorr}$ , chuck temperature  $\sim 350^\circ\text{C}$ , load  $\sim 35.0\%$ , tune  $\sim 60.0\%$ .

Dry etching (Drytek 4)  $\sim 550\text{A}/\text{s}$ :  $\text{CHF}_3$   $\sim 100\text{sccm}$ ,  $\text{O}_2$   $\sim 4\text{sccm}$ , RF power  $\sim 100\text{W}$ , pressure  $\sim 100\text{mTorr}$ , over-etch  $\sim 20\%$ .

Other related processes, such as Ohmic contact, metal lift-off, surface passivation, and others, can be found in chapter 3.

## APPENDIX B: PZT properties

### piezosystem jeria

07.12.2004

element (ser.nr.): PZ 38 SG (75086)  
 system (ser.nr.): 12 V 40 SG (19769)

tester: M. Franke  
 axis: z

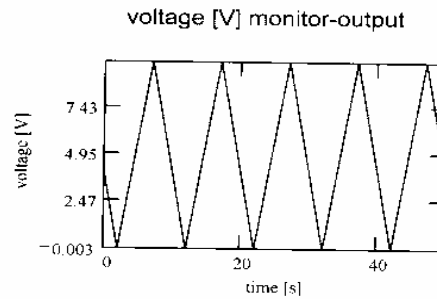
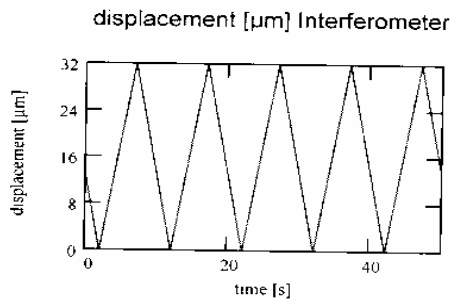
closed loop - motion:  
 monitor output:

0.0  $\mu\text{m}$       32.0  $\mu\text{m}$   
 -0.003 V      9.907 V

sensitivity = 0.3097 V/ $\mu\text{m}$   
 measurement temperature: 22,2 °C  
 upload: 50 g

measured with: ZYGO 2/20 interferometer

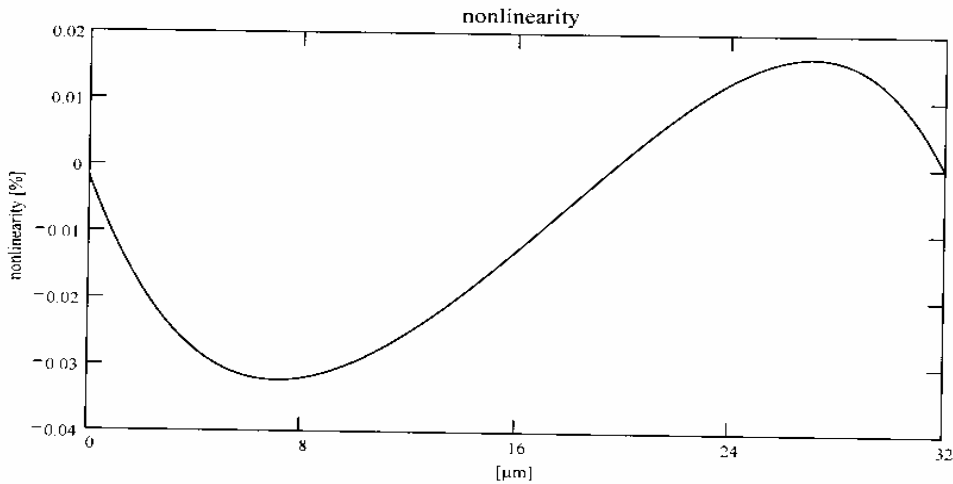
**Linearität; Genauigkeit, Wiederholbarkeit**  
**accuracy, linearity, repeatability**  
 five measurements, triangle full scale



### Linearität - linearity

max. nonlinearity : absolut = 16 nm

relativ = 0.049%



### Wiederholbarkeit - repeatability

R\_absolut = 13 nm

R\_relativ = 0.041%

data file : a475086z.prn

order no. 030957

sign: *M. Franke*

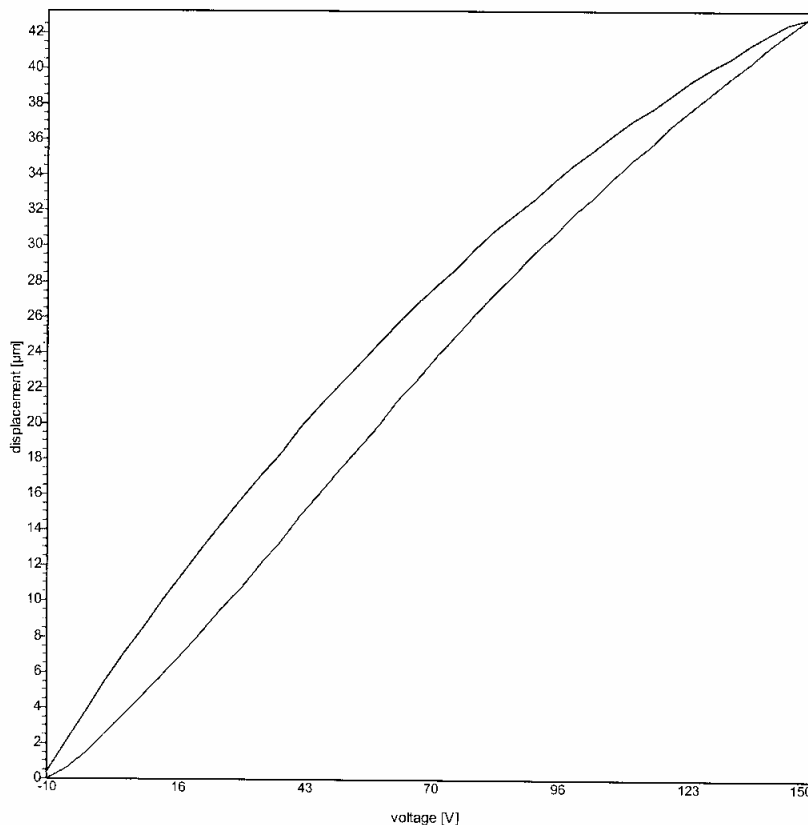


Hysteresis Protocol

element name: PZ38SG  
serial number: 75086  
order number: 30957

tester: Norbert Voigt  
date: 06.12.04

total stroke: 42,8  $\mu\text{m}$   
voltage range: -10...150 V  
max. hysteresis: 11.7%  
DMS: 34,5...43,9 mV



test O.K.:

sign: